Atomistic Simulation of Non-Equilibrium Phenomena in Hypersonic Flows

A THESIS
SUBMITTED TO THE FACULTY OF THE GRADUATE SCHOOL
OF THE UNIVERSITY OF MINNESOTA
BY

Paul Erik Norman

IN PARTIAL FULFILLMENT OF THE REQUIREMENTS
FOR THE DEGREE OF
Doctor of Philosophy

July, 2013

Acknowledgements

There are many people that have earned my gratitude for their contribution to my time in graduate school. The research into gas-surface interactions presented here has been a truly collaborative effort. I would like to thank Dr. Ioana Cozmuta, who initial work and support helped start this line of research. The assistance of Professor Adri van Duin and his student Sriram Srinivasan with the ReaxFF potential was invaluable in troubleshooting problems with the potential and developing a new version of the potential specific to our needs. I would like to thank Professor Donald Truhlar and his group members Anant Kulkarni, Hannah Leverentz, Sijie Luo, Ruben Meana-Pañeda, and Yuliya Paukku for their efforts carrying out electronic structure calculations and valuable feedback. I would also like to thank my fellow group members Chonglin Zhang and Paolo Valentini for their continuing assistance with Molecular Dynamics and Direct Simulation Monte Carlo simulations and helpful discussions. Finally, I would like to thank my advisor, Professor Tom Schwartzentruber, for his support, encouragement, and feedback over my five years at the University of Minnesota.

Abstract

The goal of this work is to model the heterogeneous recombination of atomic oxygen on silica surfaces, which is of interest for accurately predicting the heating on vehicles traveling at hypersonic speeds. This is accomplished by creating a finite rate catalytic model, which describes recombination with a set of elementary gas-surface reactions. Fundamental to a description of surface catalytic reactions are the *in situ* chemical structures on the surface where recombination can occur. Using molecular dynamics simulations with the $\text{ReaxFF}^{\text{GSI}}_{\text{SiO}}$ potential, we find that the chemical sites active in direct gas-phase reactions on silica surfaces consist of a small number of specific structures (or defects). The existence of these defects on real silica surfaces is supported by experimental results and the structure and energetics of these defects have been verified with quantum chemical calculations. The reactions in the finite rate catalytic model are based on the interaction of molecular and atomic oxygen with these defects. Trajectory calculations are used to find the parameters in the forward rate equations, while a combination of detailed balance and transition state theory are used to find the parameters in the reverse rate equations. The rate model predicts that the oxygen recombination coefficient is relatively constant at T (300-1000 K), in agreement with experimental results. At $T > 1000$ K the rate model predicts a drop off in the oxygen recombination coefficient, in disagreement with experimental results, which predict that the oxygen recombination coefficient increases with temperature. A discussion of the possible reasons for this disagreement, including non-adiabatic collision dynamics, variable surface site concentrations, and additional recombination mechanisms is presented. This thesis also describes atomistic simulations with Classical Trajectory Calculation Direction Simulation Monte Carlo (CTC-DSMC), a particle based method for modeling non-equilibrium rarefied gas flows that employs trajectory calculations to determine the outcome of molecular collisions. We compare CTC-DSMC to direct molecular dynamics calculations for one-dimensional shocks, where exact agreement between the two methods is demonstrated. We also discuss a number of topics important in CTC-DSMC simulations, including GPU enabled acceleration, a preliminary algorithm for modeling three-body collisions, and characterizing high temperature rovibrational effects.

Contents

List of Tables

List of Figures

Chapter 1

Introduction

1.1 Motivation

Accurate modeling of the non-equilibrium thermal and chemical processes occurring in the flow around hypersonic vehicles presents a major challenge for the design and reliability of these vehicles. One major challenge is the accurate prediction of aerothermal surface heating, which dictates the size and material properties of the vehicle's thermal protection system (TPS). At hypersonic speeds, a strong shock forms in front of the leading edges of a vehicle, causing a sharp increase in the gas phase density, pressure, and temperature. Depending on the speed of the vehicle, the gas phase molecules downstream of the shock can partially or fully dissociate. The layer between the surface of the vehicle and the shock (called the shock layer) is often in a state of thermal and chemical non-equilibrium. For example, at low densities characteristic of hypersonic flight, the time scale of gas phase recombination reactions can be longer than the characteristic flow time scale, which leads to concentrations of dissociated species much higher than the equilibrium value in moderate temperature regions near the surface of the vehicle. These dissociated species can diffuse through the boundary layer and chemically react (either through surface meditated recombination or surface ablation) with the surface of the vehicle, significantly contributing to the overall surface heating. Numerical simulations, such as Computational Fluid Dynamics (CFD) and Direct Simulation Monte Carlo (DSMC) have enabled increasingly accurate description of hypersonic flows over a range of regimes. However, the accuracy of these techniques depends upon the fidelity of

the continuum or particle based thermochemical models for the shock layer. The goal of this thesis is to develop tools and methodologies for modeling non-equilibrium thermal and chemical phenomenon in hypersonic flows through atomistic scale numerical simulations. Atomistic simulations are a valuable tool because they allow the simulation of regimes where experimental measurements are unavailable, and allow for a understanding of the fundamental processes, such as chemical reactions and molecular energy exchange, that govern non-equilibrium phenomena.

In this thesis, atomistic simulations are used to model the gas surface chemical reactions in oxygen silica systems and trajectory calculations are used to replace the probabalistic gas-phase collision models within the Direct Simulation MonteCarlo method. A description of these topics and their relevance to hypersonic flight is discussed below.

1.2 Oxygen Silica Surface Catalysis Under Hypersonic Conditions

During reentry, the surface of the vehicle can act as a catalyst for the exothermic recombination of dissociated species originating from the shock layer, increasing the heat flux to the vehicle's surface. Studies have shown that heterogeneous catalysis can contribute up to 30% of the total heat load for Earth reentry[8], and that the stagnation point heat flux for Mars entry could vary by a factor of three between the assumptions of highly and weakly catalytic wall.[9] To reliably design thermal protection systems for hypersonic vehicles it is important to quantify the aerothermal heating that these vehicles need to withstand. In this work we focus on oxygen recombination on silica surfaces. In hypersonic flight through Earth's atmosphere, dissociated oxygen will be present in the shock layer. At very high speeds, nitrogen dissociation and gas phase ionization will occur. Silica is chosen because it is a significant component in both reusable (LI900, LI2200, FRSI) and ablative (SIRCA) thermal protection systems.[10] Additionally, studies have found that several non-SiO_2 based thermal protection systems, such as SiC (at $T < 1800$ K) and Ultra High Temperature Ceramics (ZrB_2-SiC and ZrB_2-SiC-HfB_2 at $T < 1300$ K) form thin SiO_2 layers when exposed to air plasma, and act similarly to pure silica from a catalytic perspective.[5, 11] Despite a large body of experimental work on oxygen-silica surface catalysis[12, 6, 13, 7, 5, 14], there is still

uncertainty in precise temperature, pressure, and gas composition dependence of the catalycity of this substance.[15]

The goal of this work is to investigate oxygen-silica surface catalysis through atomistic scale simulations with the aim of improving gas-surface chemistry models in computational fluid dynamic (CFD) simulations of hypersonic vehicles. This research is covered by Chapters 2-4 of this thesis. Chapter 2 presents a literature review of experimental results and previous computational modeling in this area. In Chapter 3 we describe the ReaxFF force field, a potential parametrized to reproduce quantum chemical calculations, which is used to carry out classical molecular dynamics (MD) simulations. We use molecular dynamics simulations with this potential to model the structure of silica surfaces exposed to atomic oxygen. Through these simulations a number of potentially catalytic surface sites are identified. Chapter 4 describes the creation of a gas-surface chemical rate model based on the interaction of atomic and molecular oxygen with these surface sites. The rate model is created using a combination of trajectory calculations, estimates from simple transition state theory, detailed balance, and single point energies from quantum chemical calculations. This rate model can be incorporated into CFD simulations as a boundary condition, and the predictions of the rate model are compared to experimental results. Conclusions and future directions of this research are discussed in Chapter 6.

1.3 Classical Trajectory Calculation Direct Simulation Monte Carlo

The Direct Simulation Monte Carlo (DSMC) technique is a particle based numerical method capable of modeling non-equilibrium rarefied gas flows.[16] One key aspect of the DSMC technique is the collision model, which determines the collision rate and the outcomes of molecular collisions. The collision model ultimately determines the transport properties (such as viscosity, thermal conductivity, and diffusion coefficients) and rate of chemical reactions in the simulated gas. For complex flows involving rotational, vibrational, and chemical non-equilibrium at high temperatures (characteristic of hypersonic shock layers), recent research has investigated the use of accurate *ab initio* based potential energy surfaces (PES) to inform DSMC collision models.[17, 18, 19, 20] It has

been shown that trajectory calculations using sufficiently accurate PES have the ability to reproduce molecular beam experimental results for both collision cross-sections and product energy distributions.[21]

In Chapter 5 of this thesis we investigate classical trajectory calculation (CTC) DSMC simulations, where individual collisions are carried out "on-the-fly" during a DSMC simulation with classical trajectory calculations. This method, which was originally described by Koura[22], directly links atomistic scale calculations of collisions to macroscopic dilute gas flows. However, the high computational cost of calculating trajectories during a simulation has been one significant barrier to the widespread application of this method.[23] In Chapter 5 we address a number of topics important to expanding the utility of this method. We provide a comparison of CTC-DSMC to full molecular dynamics simulations of 1-D shocks in argon and nitrogen to demonstrate that these two numerical methods are equivalent for these flows when using an identical interatomic potential and trajectory integration schemes. Additionally, we describe a GPU parallelization scheme to accelerate CTC-DSMC simulations, and show that with existing parallel computing power this method is feasible for 3D and axisymmetric flows. A preliminary algorithm for determining the three body collision rate in CTC-DSMC simulations is presented and validated for the simple case of collisions with no interatomic potential. Finally, we introduce some of the phenomena that arise when modeling rotating, vibrating molecules including the effect of rovibrational coupling on the energy in the rotational/vibrational modes at high temperatures and shock drift in 1D shock simulations due to inconsistencies in classical and quantum descriptions of molecular vibration. Conclusions and future directions of research are discussed in Chapter 6.

Chapter 2

Literature Review of Oxygen Silica Gas Surface Catalysis

This chapter presents a literature review for the experimental and computational work modeling the heterogeneous recombination of oxygen on silica surfaces.

2.1 Experimental Review

There is a large body of experimental work measuring the catalycity of atomic oxygen on silica[24, 6, 25, 26, 7, 27, 5, 14, 28, 29] (also, see the summary paper of Bedra et al.[15]). Despite this extensive body of research, there remains uncertainty in the catalytic properties of silica with respect to atomic oxygen due to the spread in experimental results. Experiments typically report the recombination coefficient γ_o, which is defined as:

$$\gamma_o = \frac{F_{o,rec}}{F_o} \tag{2.1}$$

where $F_{o,rec}$ is the flux of oxygen atoms recombining at the surface and F_o is the total flux of oxygen atoms to the surface. In some works[27] the term 'surface loss coefficient' is used instead of 'recombination coefficient'. A surface loss coefficient is necessary in cases where oxygen is depleted at the surface by reactions other than recombination (for example, when the surface is being actively oxidized by the gas phase atomic oxygen[11]). In this work we only consider cases where all oxygen lost at the surface recombines

to form O_2. There is a large spread in the experimentally reported recombination coefficients; values for γ_o on quartz vary from 2×10^{-4}[6] to 9×10^{-3}[5] at 1000 K. One experiment reports a recombination coefficient as high as $\gamma = 0.4$ for oxygen on Reaction Cured Glass at 1000 K.[25] Therefore, care must be taken when interpreting the physical meaning of experimentally measured recombination coefficients and applying them to systems dissimilar to the original experimental setups.

There are many reasons to expect the oxygen recombination coefficient on silica to vary between experiments. One reason is the morphology of the silica sample used. Balat and coworkers report oxygen recombination coefficients that differ by a factor of $\sim$5 for quartz and a thin silica film formed on plasma oxidized SiC.[5] Different morphologies of silica may present different surfaces, which in turn may have different catalycity with respect to the recombination of atomic oxygen. Another important factor is the microscopic surface roughness. In the work by Kim and Boudart[6], the authors demonstrated that the recombination coefficient of oxygen on quartz increases linearly with a surface roughness factor, which is proportional to total surface area. Additionally, in the experiment by Alfano and coworkers[30], the authors found that the recombination coefficient of oxygen on oxidized SiC varied by a factor of two for two identically machined TPS samples. This result was attributed to the visibly different surface roughness of the samples. Therefore an experimentally measured oxygen recombination coefficient is not necessarily transferable to another sample, even within the same experiment, unless the surface area/roughness is explicitly taken into account. Of all the experiments summarized here, only the work of Kim and Boudart[6] takes this effect into account.

Another important factor affecting the oxygen recombination coefficient is the gas phase composition. In gases with multiple dissociated species (for example N_2 or CO_2), the oxygen recombination coefficient is different than in gases composed of purely oxygen because atomic oxygen can combine with other reactive species. For example, in the work of Pejaković et al.[31] the authors demonstrate that NO is formed by the surface catalyzed combination of nitrogen and oxygen on quartz. In this work we focus on cases where oxygen is the only species recombining on the surface. However, even when considering a gas composed purely oxygen, the gas phase composition can still effect the recombination coefficient. In many ground based experiments, dissociated oxygen

is created by plasma discharge, which also creates large number of electrons and ionized species. It is possible that these charged species influence the state of the surface and alter the measured recombination coefficient. For example, in the work of Carty et al.[32] the authors conclude that the oxygen recombination coefficient of oxygen is two orders of magnitude higher when the surface is submitted to ion bombardment than when the surface is only exposed to a neutral flux of species. Additionally, there is experimental evidence that silica surfaces exposed oxygen plasma exhibit charging effects, which might further alter the energetics of gas surface interactions.[33] In this work we will only consider charge neutral surface and gas phase systems, which are expected to occur during hypersonic flight (although at very high speeds gas phase ionization will occur). Finally, because of the low catalycity of silica, any impurities introduced to the surface can alter the recombination coefficient. For example it is possible that copper emitted by the electrodes[34] in Arc Jet experiments[26] might contaminate the surface with copper, altering the surface catalycity.

It is also possible that the experimental methodology used to measure recombination coefficients in different works affects the reported values. In some experiments[26, 28], surface heating is used to measure the oxygen recombination coefficient. Measurements using the surface heating typically rely on the assumption that the non-convective heating on the surface arises from fully accommodated surface reactions. However, it is possible that recombination reactions do not produce molecules fully accommodated to the surface temperature (for example surface recombination may produce vibrationally or electronically excited molecules), which would tend to reduce the surface heating and affect the measured recombination coefficient. The effect of thermal accommodation is often characterized by a thermal accommodation coefficient:

$$\beta = \frac{\Delta H_{act}}{\Delta H_{eq}} \tag{2.2}$$

where $\Delta \mathrm{H}_{eq}$ is the difference between the enthalpy of the reactants and products at equilibrium, and $\Delta \mathrm{H}_{act}$ the change in enthalpy due to a recombination reaction. While there are experimental estimates of the thermal accommodation coefficient[25, 35], these are even more uncertain than experimentally measured recombination coefficients. It is of note that the thermal accommodation coefficient can be affected by more than simply recombination reactions. For example, in the work of Balat and et al.[35], the authors

account for the surface heating due to the quenching of electronically excited N_2 and O_2 upon collision with the surface. Another common method for measuring the oxygen recombination coefficient is to measure the spatial[5, 31, 29] or temporal variation[32] in the concentration of atomic oxygen. Such approaches rely on continuum level modeling of systems in chemical non-equilibrium, accurate simulation of which is challenging. Uncertainties in surface catalysis experiments are difficult to estimate, and in some cases are estimated to be as high as several hundred percent.[7]

2.1.1 Interpretation of Experimental Results

Despite the uncertainty in experimental results, there are some consistent trends seen across a number of experiments. For example, at temperatures between 300 K and 1000 K, γ_O on quartz remains relatively constant with temperature.[6, 7] At T > 1000 K, measured recombination coefficients show a weak exponential trend with temperature.[6, 5, 25] Assuming recombination coefficients follow an Arrhenius trend, an activation energy for oxygen recombination on quartz at high temperatures has been interpreted as 0.19 $\pm$ 0.01 eV by Balat-Pichelin et al.[5] and 0.18 $\pm$ 0.04 eV by Kim and Boudart.[6] It is thought[6, 5] that oxygen recombination on silica surfaces at high temperatures is due to an Eley-Rideal (ER) type reaction.[36] Thus, the interpreted activation energy has been associated with the ER recombination reaction. In a number of works, the low temperature trend in recombination coefficients is attributed to a Langmuir-Hinshelwood (LH) recombination type mechanism, where mobile physisorbed atomic oxygen diffuse on the surface and recombine with chemisorbed atomic oxygen.[14, 6, 37] The trend in γ_O with pressure is less certain, however, in experiments where pressure in varied there is evidence that γ_O on Pyrex and oxidized Zr-B_2-SiC decreases with pressure.[38, 27] We will analyze how the results of atomistic scale simulations confirm or disagree with these interpretations in Chapter 4.

2.2 Review of Computational Modeling

Previous studies in this area have been carried out for the interaction of atomic and molecular oxygen with the (001) cleaved β-cristobalite[39, 40, 41, 42, 43, 44] surface and for the interaction of atomic oxygen with the cleaved (001) β-quartz surface.[45, 46]

In one series of studies,[41, 43, 44] the authors used quantum chemical calculations (PW91 density functional calculations) to generate potential energy surfaces for the interactions of O and O_2 with the surface. The potential energy surfaces were fit with a corrugation-reducing procedure, allowing the authors to carry out quasiclassical trajectory calculations for a number of reactions. In another series of studies[39, 40, 46] the authors used an empirical interatomic potential (based on PBE0 density functional calculations in one work[40]) to describe the interaction of oxygen with the surface. The potential energy surfaces developed in these works are only applicable to describing gas-surface interactions on the cleaved silica surface which they were parametrized with, and are not expected to be transferable to other silica polymorphs (for example amorphous SiO_2). In both series of studies the authors used cleaved silica surfaces. However, cleaved silica surfaces are covered by highly reactive dangling bonds and tend to reconstruct to lower energy states, minimizing the number of under-coordinated atoms on the surface. This has been shown by various calculations employing density functional theory[47] (DFT) with various exchange-correlation (xc) functionals. For example, direct dynamics calculations employing the PBE and LDA xc functionals showed that the (011) α-quartz surface reconstructs into a disordered state at room temperature.[48] There are also calculations[49] with the PW91 xc functional on structures generated with an empirical potential indicating the reconstruction of the (0001) α-quartz surface to (1×1) and (2×1) patterns, and direct dynamics calculations with the LDA xc functional also the favorability of a (1×1) reconstruction.[50] Experimental results are also varied, with experiments showing reconstruction of the (0001) α-quartz surface to (1×1) and ($\sqrt{84} \times \sqrt{84}$) patterns[51] and a (2×2) pattern.[52] Recent experiments[53] on dry two-dimensional amorphous silica glasses may also be relevant. As described in Chapter 3, molecular dynamics simulations of the (0001) α-quartz surface (similar to the surface used in [45]) show that this surface reconstructs to a lower energy state, significantly altering the structure of the surface. Generally, we expect that dry, cleaved silica surfaces are not stable and tend to reconstruct to lower energy states. The existence of cleaved silica surfaces that are stable without surface hydroxyls or surface waters calls for additional study. Furthermore, exposure to highly reactive atomic oxygen will likely further influence the structure of silica surfaces. Essential to an understanding of the

gas-surface chemical reactions is accurate characterization of the *in situ* chemically active sites occurring on the surface. In this work, Chapter 3 is devoted to characterizing which surface sites occur on realistic silica surfaces exposed to atomic oxygen.

In the work by Cozmuta[10], which served as an impetus for this research, the author considered both quartz and amorphous silica surfaces exposed to nitrogen and oxygen mixtures. In this case the author used the $\text{ReaxFF}_{\text{SiO}}$ potential, which is described in Chapter 3. Molecular dynamics simulations consisted of a silica slab in a periodic box with a fixed number of gas molecules. While results of early simulations using this approach were valuable, this approach proved somewhat problematic because the gas molecules in the box quickly adsorbed or recombined on the surface, making it difficult to define the gas phase temperature and pressure. To better simulate the exposure of a silica surface to a gas at a fixed chemical composition, we implement a flux boundary condition, which is detailed in Chapter 3.

In summary, there are two crucial aspects in computational modeling of oxygen recombination on silica surfaces: an accurate description of the structure of silica surfaces exposed to atomic oxygen, and an accurate interatomic potential to describe gas-surface interactions. Previous computational works focused on modeling the interaction of atomic and molecular oxygen with cleaved silica surfaces. However, the structure of silica surfaces exposed to atomic oxygen is not well known, and there are experimental and computational results indicating that cleaved silica surface tend to reconstruct, altering their surface chemistry. While the potential energy surfaces developed in some previous works are based on quantum chemical calculations and are accurate for describing oxygen interaction with these cleaved surfaces[40, 41, 42, 43, 44], they are not transferable to other, more realistic, silica surfaces. In this work our goal is to use the $\text{ReaxFF}^{\text{GSI}}_{\text{SiO}}$ potential, which can describe a variety of silica polymorphs and was specifically parametrized to describe gas-surface chemical reactions[3], to model which structures occur on silica surfaces exposed to atomic oxygen by conducting large scale simulations of the gas-surface interface region. The structures occurring on these surfaces are used to further study individual chemical reactions and to create a rate model for oxygen recombination on silica.

Chapter 3

The Structure of Silica Surfaces Exposed to Atomic Oxygen

Accurate characterization of the structure of silica surfaces is important in a wide variety of applications. For example, chemically active sites on silica surfaces are thought to contribute to the toxicity of freshly ground silica, a known carcinogen and the cause of acute silicosis.[54] The rates of surface reactions are important in the growth of thin silica films formed by chemical vapor deposition, which are used in semiconductor circuits to isolate conducting regions.[55] Additionally, the structure of silica surfaces is important for aerospace applications, where surface reactions on silica-based thermal protection systems can increase the surface heating on re-entry vehicles. The focus of this chapter is on the structure of silica surfaces when exposed to atomic oxygen at high temperatures (1000–1750 K) characteristic of a thermal protection system during atmospheric re-entry.

There has been a great deal of experimental work on the surface chemistry of silica surfaces exposed to water (for example, see the extensive summary paper of Zhuravlev[56]). Under standard terrestrial conditions, silica surfaces are primarily covered with bridging oxygen atoms (Si-O-Si), surface hydroxyls (Si-OH), and physisorbed water molecules.[56] In this work we focus on the structure of dry silica surfaces exposed to atomic oxygen. It is typically assumed that water/hydroxyl groups on the surface are

removed by the high temperature, low pressure, and reactive dissociated gas flux experienced by the surface during re-entry[10], and in many experimental works silica surfaces are dehydroxylated in similar high temperature, low pressure environments.[56] There is relatively little data in the literature about the structure of dry silica surfaces that have been exposed to atomic oxygen. One measurement comes from the atomic beam experiments of Carleton and Marinelli, who found that Reaction Cured Glass exposed to atomic oxygen had a high ratio of oxygen to silicon ($\sim$3.5:1) near the surface.[25] In this chapter we use molecular dynamics (MD) simulations to describe the surface structures occurring on dry silica surfaces under vacuum and exposed to atomic oxygen with the ReaxFF$^{\text{GSI}}_{\text{SiO}}$ potential.

Although the ReaxFF$^{\text{GSI}}_{\text{SiO}}$ potential was parametrized using many phases of SiO_2 including coesite, cristobalite, tridymite, and stishovite, we only consider the interaction of oxygen with two stable surfaces: (1) quartz, which has been experimentally well characterized in many catalysis experiments,[15] and (2) amorphous silica, which presents a surface like those of thermal protection systems during re-entry. For molecular dynamics simulations, we use the LAMMPS MD program[57] with the ReaxFF$^{\text{GSI}}_{\text{SiO}}$ potential. The ReaxFF$^{\text{GSI}}_{\text{SiO}}$ potential was specifically parametrized with density functional calculations of the interaction of molecular and atomic oxygen with silica surfaces, and it is freely available in the supporting information of the work by Kulkarni et al.[3]

This chapter is organized as follows. Section 3.1 describes the ReaxFF$^{\text{GSI}}_{\text{SiO}}$ potential and its parametrization. In section 3.2 we validate the ReaxFF$^{\text{GSI}}_{\text{SiO}}$ potential for the bulk structure of α/β-quartz and amorphous silica (a-SiO_2). In section 3.3 we describe the preparation of quartz and a-SiO_2 surfaces. Section 3.4 details the flux boundary condition, which is used to expose surfaces to atomic oxygen at a given temperature and pressure. In section 3.5 we analyze the structures occurring on silica surfaces under different conditions and discuss their importance in the heterogeneous recombination of atomic oxygen, and in section 3.6 we present our conclusions.

3.1 Description of the ReaxFF$^{\text{GSI}}_{\text{SiO}}$ Potential

Molecular dynamics simulations based on empirical potentials have been used widely in the study of gas surface interactions of atomic and molecular oxygen with silica

surfaces.[41, 42, 43, 44, 39, 45, 46] A number of previously developed empirical force fields describing SiO systems[58, 59, 60, 61] have been successful in describing the structures and energies of various polymorphs of silicon and silicon oxides. Specifically, the BKS potential[60] has been used for simulating bulk silica and silica surfaces.[62] Although these force fields provide valuable insights into the dynamics of silica polymorphs and their chemistry, they are applicable only close to the structures of the morphologies against which they were parametrized. This imposes a severe restriction on the transferability of these potentials and their ability to simulate chemical reactions. In this work we use the ReaxFF interatomic potential to carry out molecular dynamics calculations. ReaxFF is a general bond-order dependent potential that uses a relationship between bond distance and bond order and a relationship between bond order and bond energy to describe bond formation and bond dissociation realistically.[63] Bond orders are combined with functions of valence coordinates such as bond angles and torsion angles so that the energy contributions from bonding terms vanish on bond dissociation. The ReaxFF potential uses a central field formalism wherein non-bonded interactions, namely Coulomb and van der Waals interactions, are calculated between every atom pair. Excessive short range interactions are avoided by using a shielding term in the energy expression for the non-bonded interactions. Atomic charges are calculated using the geometry-dependent charge calculation scheme (EEM scheme) of Mortier et al.[64] Instead of an Ewald summation to calculate long-range Coulomb interactions, ReaxFF uses a seventh-order taper function with an outer cutoff radius of 10 Å. The system energy in ReaxFF is calculated as the sum of a number of energy terms according to:

$$E_{\text{system}} = E_{\text{bond}} + E_{\text{over}} + E_{\text{under}} + E_{\text{ip}} + E_{\text{val}} + E_{\text{pen}} + E_{\text{tors}} + E_{\text{conj}} + E_{\text{vdWalls}} + E_{\text{Couloumb}} \tag{3.1}$$

A detailed description of each of these terms and their energy expressions can be found in the original work.[65] The ReaxFF potential has been shown to accurately model a diverse array of chemically reacting systems, including gas surface interfaces. For example, ReaxFF MD simulations of the trapping probability of low-incident-energy (<0.4 eV) oxygen molecules on the Pt(111) surface are in good quantitative agreement with experimental results.[66] To describe the structures, properties, and chemistry specific to silicon and silicon oxide materials, $\text{ReaxFF}_{\text{SiO}}$ was developed by van Duin

et al.[65] $\text{ReaxFF}_{\text{SiO}}$ simulations of the oxidation of Si(100) reconstructed surfaces[67, 68] and Si nanowires[69] have been shown to closely match the experimental radial distribution functions and bond angle distributions. Although the $\text{ReaxFF}_{\text{SiO}}$ potential has been developed and used extensively, it was not specifically parametrized for gas-surface interactions. Therefore a new version of the $\text{ReaxFF}_{\text{SiO}}$ potential, called the $\text{ReaxFF}^{\text{GSI}}_{\text{SiO}}$ potential, was developed to describe gas-surface interactions in oxygen silica systems.[3] This potential takes a central role in this research, and a description is given below.

One key aspect of the ReaxFF potential is that it is parametrized using quantum chemical calculations. This potentially allows for a force field that reproduces accurate but computationally expensive quantum chemistry calculations at a fraction of their cost. The implementation of ReaxFF potential in parallel MD codes such as LAMMPS[57] allows for molecular dynamics simulation of larger systems (millions of atoms), where as DFT is limited to calculations of smaller systems (< 100 atoms). In the work by Kulkarni et al.[3] the authors modeled the interaction of atomic and molecular oxygen with a set of structures on silica surfaces that had been observed in MD simulations with other empirical interatomic potentials and whose existence on silica surfaces was experimentally confirmed. These structures were represented by small clusters (made up of 1-5 silica tetrahedral units) of atoms, which were shown to be sufficient to represent the larger surface. Highly accurate but computationally expensive Coupled Cluster (CCSD(T)) calculations[70, 71] were used on select systems to validate that computationally less expensive Density Functional Theory (DFT) calculations with the M06 model chemistry[72, 73] could be used for extensive calculations.

A large number of DFT calculations for the interaction of atomic and molecular oxygen with clusters representative of surface structures were carried out.[3] One important conclusion of this work based on the results of electronic structure calculations was the importance of electronic energy states. For example Fig. 3.1 shows the potential energy surface for an oxygen atom interacting with a silica cluster. Density functional theory results for the system in the doublet (D) state show that there is an energy barrier for the approach of the atom to the cluster, followed by a potential energy minimum of $\sim$2 eV. However DFT results for the system in the quartet (Q) state show that there is no energy barrier or significant adsorption minimum. The $\text{ReaxFF}^{\text{GSI}}_{\text{SiO}}$ potential was

parametrized with the results of DFT calculations using the potential energy of the locally lowest energy spin state. This assumes that the system switches between electronic energy states when potential energy surfaces cross, and always follows the lower energy potential energy surface. However, in reality the system could remain in one electronic energy state throughout the course of a gas-surface interaction, which could alter the outcome of the interaction. Nevertheless, a potential parametrized to the local lowest electronic energy state is a valuable first step in a realistic description of oxygen silica gas-surface interactions.

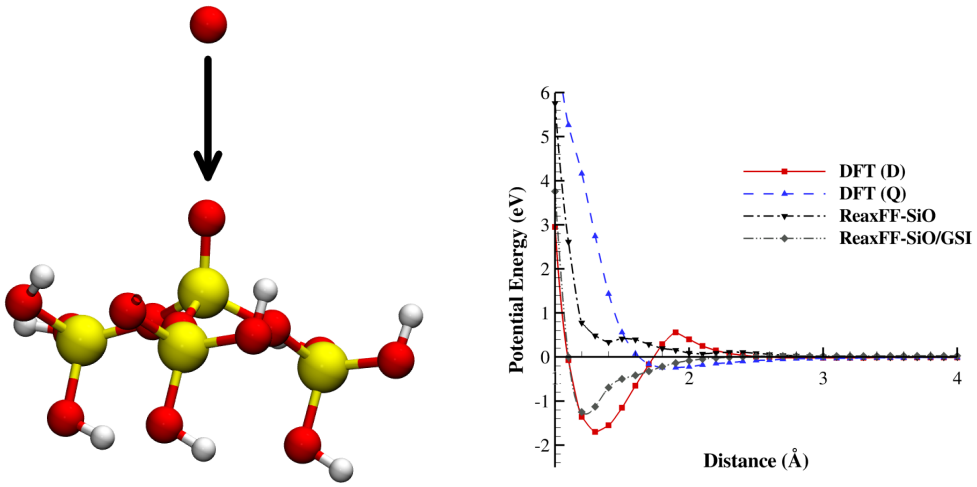

(a) Silica Cluster. Silicon atoms are yellow, oxygen atoms are red, hydrogen atoms are white

(b) Potential Energy Surface. Distance is defined by the distance between the center of the O_2 molecule and top most silicon atom.

Figure 3.1: Potential energy surface of O_2 interacting with a silica cluster from Kulkarni et al.[3]

In the work by Kulkarni et al.[3], it was shown that the $\text{ReaxFF}^{\text{GSI}}_{\text{SiO}}$ potential was in better agreement with DFT results than the $\text{ReaxFF}_{\text{SiO}}$ potential. However, it is of note that the $\text{ReaxFF}^{\text{GSI}}_{\text{SiO}}$ potential was not in exact agreement with the DFT results for all cases (for example, see Fig. 3.1), so any specific predictions of this potential, such as accurate binding energies or geometries, should still be validated against DFT. The $\text{ReaxFF}^{\text{GSI}}_{\text{SiO}}$ potential file is available in the supporting information of the work by

Kulkarni et al.[3] The potential file is formatted so that it can be read by LAMMPS, a freely available open source program.[57]

3.2 Validation of ReaxFF$^{GSI}_{SiO}$ Potential

3.2.1 Bulk α-quartz and β-quartz

Here, we validate that the ReaxFF$^{GSI}_{SiO}$ potential reproduces the crystal structure of α/β-quartz. These two slightly different morphologies are distinguished by a rigid 16.3° rotation of the SiO_4 tetrahedra in the bulk about the (100) axis[74], and the transition from α-quartz to β-quartz occurs at 846 K for pure crystalline quartz at atmospheric pressures.[75] To validate that the ReaxFF$^{GSI}_{SiO}$ potential accurately reproduces these crystal structures, we performed an energy minimization that included anisotropic relaxation of the crystal cell on a single unit cell of the experimental bulk structure with periodic boundary conditions and a pressure of 1 atm. The experimentally predicted crystal structures for α-quartz and β-quartz were taken from the works by Levien et al.[76] and Kihara[77] via the American Mineralogist Crystal Structure Database.[78] A comparison between experiment and the ReaxFF$^{GSI}_{SiO}$ potential for various geometric values in the unit crystal cell are shown in Tables 3.1 and 3.2 for α-quartz and β-quartz respectively. In all cases the bond length predicted by ReaxFF$^{GSI}_{SiO}$ is within 0.02 Å of the experimental value and the bond angle is within 0.1° of the experimental value.

3.2.2 Bulk a-SiO_2

Here we validate that the ReaxFF$^{GSI}_{SiO}$ potential can accurately reproduce the structure of amorphous silica. Whereas the structure of quartz, being periodic, required optimization of only a single unit cell, for a-SiO_2 a larger sample was necessary, which was generated by molecular dynamics simulations following the annealing procedure described by Huff et al.[79] A periodic crystalline sample containing 11,616 atoms of β-cristobalite (chosen because it has a similar density to a-SiO_2) was given an initial temperature of 8000 K and propagated for 20 ps under NVT dynamics to randomize its crystal structure. The system was then cooled at 50 K/ps under NVT dynamics until it reached 300 K. We found that slower cooling rates (25 K/ps, 12.5 K/ps) did not significantly influence the

	$\text{ReaxFF}_{\text{SiO}}^{\text{GSI}}$	Experiment[76]
a (Å)	4.857	4.916(1)
c (Å)	5.334	5.4054(4)
V (Å^3)	108.98	113.13(1)
Si-O (Å)	1.585	1.614(1)
Si-O (Å)	1.593	1.605(1)
$\angle$ Si-O-Si (degrees)	143.85	143.73(7)
$\angle$ O-Si-O (degrees)	110.44	110.52(6)
$\angle$ O-Si-O (degrees)	108.85	108.81(2)
$\angle$ O-Si-O (degrees)	109.03	108.93(9)
$\angle$ O-Si-O (degrees)	109.22	109.24(8)

Values in parenthesis are experimental uncertainty estimates in the last digit.

Table 3.1: Comparison of experimental and computational results for the crystal structure of α-quartz. The parameters a and c are the dimensions of the unit cell.

	$\text{ReaxFF}_{\text{SiO}}^{\text{GSI}}$	Experiment[77]
a (Å)	4.956	4.997
c (Å)	5.411	5.455
V (Å^3)	115.11	117.93
Si-O (Å)	1.575	1.587
$\angle$ Si-O-Si (degrees)	153.47	153.43
$\angle$ O-Si-O (degrees)	110.12	110.12
$\angle$ O-Si-O (degrees)	110.94	110.98
$\angle$ O-Si-O (degrees)	107.38	107.34

Table 3.2: Comparison of experimental and computational results for the crystal structure of β-quartz. The parameters a and c are the dimensions of the unit cell.

resulting final bulk a-SiO_2 structure. The system was propagated for an additional 40 ps under NPT dynamics at 300 K, 1 atm, with the last 20 ps used to collect statistics

about the structure. For all MD simulations in the NVT and NPT ensembles we used the Nosé-Hoover thermostat/barostat with a time damping value of 100 fs.[80] The sample was large enough to ensure sufficient statistics about the structure were collected.[79] Simulations were performed with the ReaxFF$^{GSI}_{SiO}$ potential and the BKS potential using the modifications outlined in the work by Jee et al.[81] The BKS potential is included here because it has been shown to reproduce the bulk structure of amorphous silica.[82]

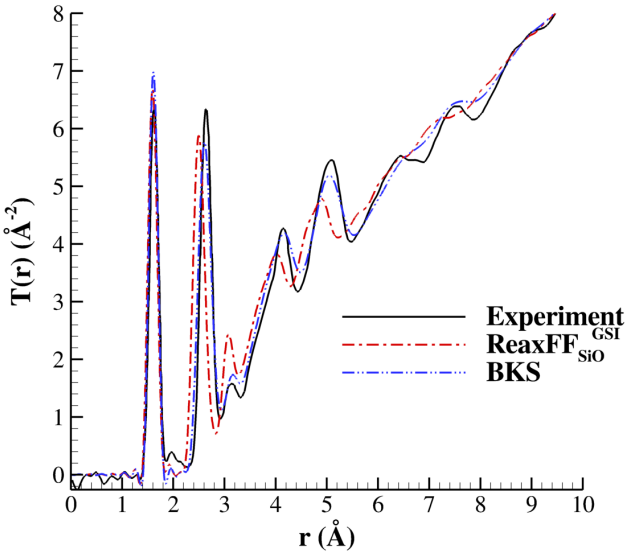

Figure 3.2: Comparison of total correlation function $T(r)$ to experiment[4]

The total correlation function ($T(r)$) can be used to directly compare the computationally generated structure to neutron scattering experiments. This function is generated from the partial radial distribution functions from MD simulations as described by Nakano et al.[83] A comparison between the total correlation function predicted by MD simulations and experiment is shown in Fig. 3.2. The ReaxFF$^{GSI}_{SiO}$ and BKS potentials are in good agreement with experimental results for the location and magnitude of the first peak, which represents the average Si-O bond length. The ReaxFF$^{GSI}_{SiO}$ potential underpredicts the location of the secondary peak, which corresponds to the average distance between O-O nearest neighbors, by 0.15 Å (the ReaxFF$_{SiO}$ potential, which

was parametrized only for bulk silica polymorphs[65], underpredicts the location of this peak by approximately the same amount[84]). Overall, the BKS potential is in slightly better agreement with the experimentally measured total correlation function than the $\text{ReaxFF}^{\text{GSI}}_{\text{SiO}}$ potential; however, the BKS potential lacks the ability to describe chemical reactions such as gas-phase oxygen-oxygen bonding because of its two-body nature. Table 3.3 shows a comparison of MD results to other available experimental measurements, where it is seen that the $\text{ReaxFF}^{\text{GSI}}_{\text{SiO}}$ potential is generally in good agreement with the experimentally measured bulk structure.

	Experiment		$\text{ReaxFF}^{\text{GSI}}_{\text{SiO}}$	BKS.
Si-O first RDF[a] max(Å)	1.608(4)[85]	1.62[86]	1.59	1.61
O-O first RDF[a] max(Å)	2.626(6)[85]	2.65[86]	2.48	2.64
Si-Si first RDF[a] max(Å)	3.077[87]		3.03	3.15
∠ Si-O-Si Avg. (degrees)	152.[88]		146.0	149.5
∠ Si-O-Si RMS[b] (degrees)	7.5[89]		14.02	13.75
∠ O-Si-O Avg. (degrees)	109.7(6)[85]		107.91	109.10
∠ O-Si-O RMS[b] (degrees)	4.5 [85]		15.4	7.40
Density(gm/cm^3)	2.20[86]		2.22	2.21
%2 coord. O			97.8	99.4
%4 coord. Si			99.0	99.4

[a]Radial Distribution Function

[b]Root Mean Square

Table 3.3: Comparison of structural features of bulk a-SiO_2 to experiment.

3.3 Silica Surface Preparation

3.3.1 Quartz Surfaces

A quartz surface can be created by cleaving the bulk along the desired plane, for example, the cleaved (0001) α-quartz surface is shown in Fig. 3.3(a). However, such cleaved surfaces are covered in highly reactive dangling bonds, and they tend to rapidly reconstruct. There are calculations[49] with the PW91 density functional on structures

generated with an empirical potential indicating reconstruction to (1×1) and (2×1) patterns, and direct dynamics calculations with the LDA density functional indicating the favorability of a (1×1) reconstruction.[50] To generate initial geometries for the reconstructed surface, we used the procedure described by Chen et al.[49] A slab composed of 4×4×6 unit cells of α-quartz (720 atoms) with two (0001) cleaved, oxygen terminated surfaces was created by deleting atoms above and below specified z-values from a sample of the periodic crystal structure. The domain containing slabs was periodic in all directions with a vertical spacing between slabs of 100 Å. To generate reconstructed surfaces, the system was heated from 0 K to 1400 K under NVT dynamics with the BKS potential at a rate of 50 K/ps. At intervals of 100 K, a copy of the slab was quenched to 0 K and a final energy minimization allowing for anisotropic box relaxation with a pressure of 1 atm was performed with the ReaxFF$^{\text{GSI}}_{\text{SiO}}$ potential. The ReaxFF$^{\text{GSI}}_{\text{SiO}}$ potential predicts that the (0001) α-quartz surfaces created with this procedure exhibit either (1×1) or (2×1) reconstructions, as shown in Fig. 3.3(b,c) and Fig. 3.3(d) respectively. These patterns are consistent with the experimental evidence, which shows that the reconstruction of the (0001) α-quartz surface exhibits (1×1)[51, 52] and (2×2)[52] patterns. It is thought that alternating patches of the (2×1) reconstruction account for the experimentally observed (2×2) pattern.[49]

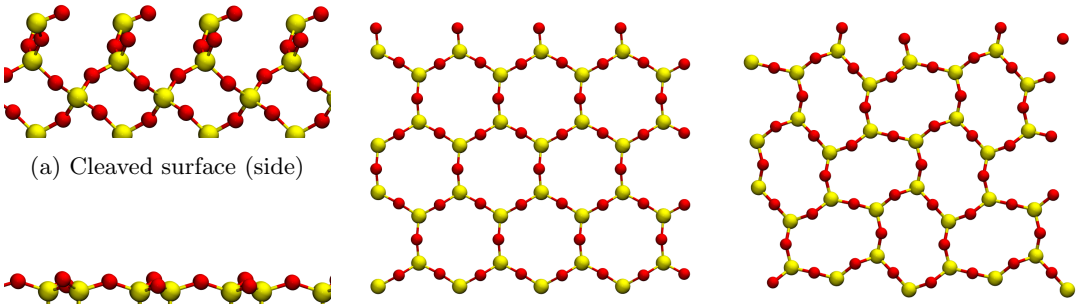

(a) Cleaved surface (side)

(b) (1×1) surface (side)

(c) Top layer of (1×1) reconstruction (top)

(d) Top layer of (2×1) reconstruction (top)

Figure 3.3: (0001) α-quartz surfaces

A comparison between the surface energy as predicted by the ReaxFF$^{\text{GSI}}_{\text{SiO}}$ potential

and other works using DFT is shown in Table 3.4. The surface energy is defined as:

$$E_{\text{surf}} = \frac{E_{\text{slab}} - E_{\text{bulk}}}{A_{\text{surface}}} \tag{3.2}$$

where E_{slab} is the energy of the slab under vacuum, E_{bulk} is the energy of the atoms if they were in the bulk quartz structure, and A_{surface} is the surface area of the slab including both the top and bottom faces. As shown in Table 3.4, the surface energy predicted by the ReaxFF$^{\text{GSI}}_{\text{SiO}}$ potential is in good agreement with the surface energies predicted by DFT. We will use the (0001) α-quartz surface with the (1×1) reconstruction in further MD simulations on quartz surfaces. At temperatures used in subsequent simulations (T > 1000 K) surfaces initialized from either the (1×1) or (2×1) reconstructions are indistinguishable, so we will simply refer to this surface as the reconstructed (0001) α-quartz surface. For the purposes of gas surface interaction simulations we used larger slabs containing 2400 atoms which were 17 atomic layers thick (12 Å) and 10×10 unit cells (49×42 Å) in area. We found that using thicker slabs did not influence any of the measured surface properties. We will use the (0001) α-quartz surface as a model for a quartz surface that has not yet been exposed to atomic oxygen, although it is noted that real quartz surfaces could present a number of crystal faces.

Surface	Surface energy (eV/Å^2)				
	Chen et al.[49]			Riganese et al.[50]	ReaxFF$^{\text{GSI}}_{\text{SiO}}$
Cleaved	0.167			0.17	0.12
(1×1)	0.031	0.0308		0.05	0.045
(2×1)	0.0273	0.0298	0.343		0.033

Table 3.4: Surface energy of (0001) α-quartz

3.3.2 Amorphous Silica Surfaces

A slab of amorphous silica can be created by deleting atoms above a convenient plane from the previously generated periodic bulk a-SiO_2 structure, in a similar manner to the quartz surfaces described above. However, this creates a slab with unrealistic cleaved surfaces that are terminated by highly reactive broken bonds which reconstruct to lower

energy states over long time scales. To generate more realistic surfaces, we performed MD annealing simulations. The final state of an annealed silica slab or periodic bulk structure is dependent on the annealing procedure.[84, 79] Unlike bulk a-SiO_2, there is relatively little information in the literature about the concentrations of specific features on real a-SiO_2 surfaces, so it is difficult to evaluate the effectiveness of a given annealing procedure.

To create surfaces, we followed the procedure detailed in Fogarty et al.[84] A slab of a-SiO_2 was heated at 25 K/ps from 300 K to 4000 K under NVT dynamics and then cooled back to 300 K at the same rate. The system was propagated for an additional 40 ps under NPT dynamics at 300 K, 1 atm, with the final 20 ps used to collect statistics. Slabs were 50×50×20 Å (4300 atoms), and periodic in all directions, with a vertical spacing of 100 Å between slabs. We found that using thicker slabs did not affect any of the measured surface properties. In MD annealing simulations we found that slower cooling rates or additional annealing cycles produced surfaces with slightly lower surface energies and slightly fewer defects (a complete description of the identification of surface defects is presented in section 3.5). However, we found that the same types of defects occur on surfaces annealed for longer times. Therefore, although the surfaces used here contain more defects that they would if annealed at slower rates, they still contain the salient structural features of realistic a-SiO_2 surfaces. We will use the annealed a-SiO_2 surface created here as a model for amorphous silica surfaces that have not yet been exposed to atomic oxygen.

3.4 Flux Boundary Condition Simulations

To simulate the gas-surface interface of a silica surface exposed to atomic oxygen in MD simulations, we implement a flux boundary condition, where gas-phase atoms enter and leave through a plane over the surface during the course of the simulation. This approach assumes that the surface is interacting with a uniform, static volume of ideal gas. The number of atoms colliding with the surface per unit area per unit time is given by the flux of an ideal gas through a plane:

$$F = \frac{n\overline{C}_o}{4} \tag{3.3}$$

where n is the number density, and $\overline{C}_o$ is the average molecular speed. A conceptual diagram of the flux boundary condition is shown in Fig. 3.4. Atom additions are distributed randomly over the course of the simulation by sampling from a Poisson distribution based on the expected flux through the plane above the surface at each time step. Atoms are initialized randomly on a plane 10 Å above the surface, which is the interatomic force cutoff used in our calculations, and any species more than 15 Å from the surface is deleted from the simulation. The initial velocity of gas-phase atoms is sampled from the Maxwell-Boltzmann distribution as described by Garcia and Wagner.[90] The position of the slab is fixed by freezing a central layer of atoms within the slab, while atoms within 2 Å of the frozen layer are thermalized with a Langevin thermostat to maintain the surface temperature. Atoms that are not frozen or thermostatted are allowed to move freely.

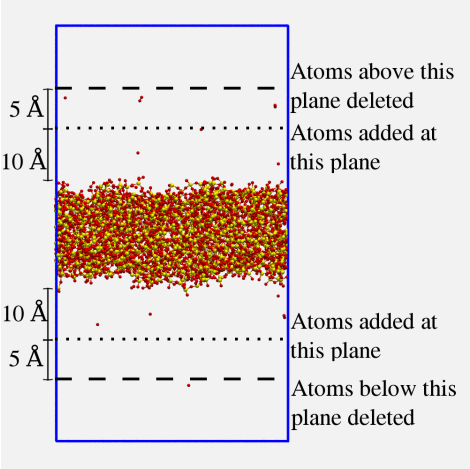

(a) Diagram of the flux boundary condition

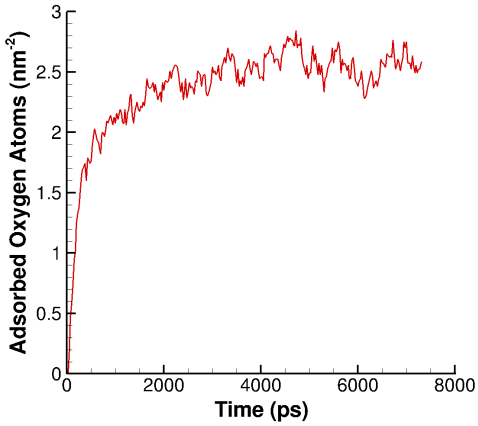

(b) Concentration of adsorbed oxygen vs. time for a-SiO_2 surface at 10 atm, 1000 K

Figure 3.4: Flux boundary condition simulations

When exposed to atomic oxygen the silica surfaces studied here adsorb atomic oxygen, increasing the ratio of oxygen to silicon atoms on the surface above 2:1, in qualitative agreement with molecular beam experimental results.[25] The amount of time

taken for a surface to reach a steady-state population depends on the pressure and temperature of the gas to which the surface is exposed. For example, the concentration of oxygen atoms adsorbed on an amorphous silica surface at $P = 10$ atm, $T = 1000$ K is shown in Fig. 3.4(b). Due to the long time scales (in MD terms) associated with this population, this method is limited to high pressures ($P > 1$ atm). For all subsequent calculations involving surfaces exposed to atomic oxygen, surfaces are first exposed to atomic oxygen until the number of adsorbed oxygen atoms reaches a steady state. Here, we define steady state as no significant change in the concentration of adsorbed atomic oxygen for 1 ns. It should be noted that due to the short time scales available in MD simulations, it is possible that the population of oxygen on surfaces exposed to a flux of atomic oxygen for longer periods might further increase. However, select cases that ran for longer times (up to 10 ns) remained at the steady-state concentration reached at earlier times.

3.5 Results and Discussion

It is thought[6, 5] that oxygen recombination on silica surfaces at high temperatures is due to a weakly activated ($E_a \cong 0.2$ eV) Eley-Rideal (ER) type reaction.[36] The potential catalycity of oxygen atoms adsorbed on silica surfaces with respect to direct gas-phase recombination can be evaluated through their binding energy. Figure 3.5 shows the distribution of binding energies of oxygen atoms on the reconstructed (0001) α-quartz and a-SiO_2 surfaces after exposure to atomic oxygen. Both plots use a bin width of 0.1 eV and are normalized. The binding energy of an oxygen atom is evaluated as the difference in the total system energy with the oxygen atom in its bound geometry and the oxygen at an infinite distance from the surface. All binding energies are calculated after the surface geometry is first relaxed via an energy minimization. As shown in Fig. 3.5, the majority of oxygen atoms on the silica slabs are in strongly bound ($\sim$10 eV) bridging configurations (Si-O-Si), which can exist either in the bulk or on the surface. These atoms are not likely to directly recombine with impinging gas-phase atoms because such a reaction would be endothermic with an activation energy of at least 5 eV (that is, 10 eV to break the bond to the surface minus 5 eV from forming O_2). Sites participating in weakly activated Eley-Rideal recombination must have a binding

energy cloose to the O_2 bond energy. As shown in Fig. 3.5, a number of specific sites (or defects) meet this criteria. These defects are identified as three types of non-bridging oxygen (NBO I-III) configurations and a peroxyl defect, shown in Fig. 3.6. This figure also shows the undercoordinated silicon defect (Si-UC), which is the precursor to the NBO I defect. Figure 3.7 shows these defects highlighted on thin slices (∼20 Å in the direction normal to the page) of both quartz and a-SiO_2 slabs after exposure to atomic oxygen. It is noted that because only a thin slice of the surface is displayed, bonds at the front and back of the displayed slice appear broken.

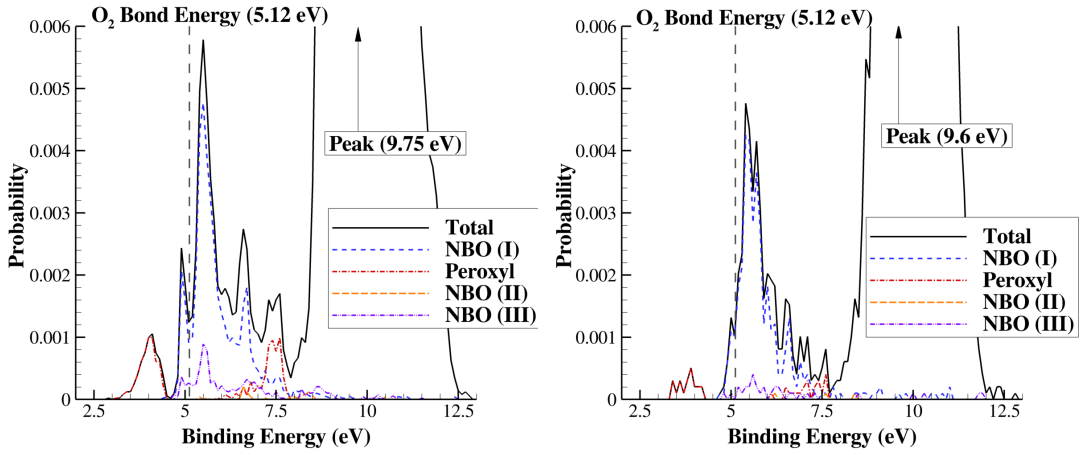

(a) a-SiO_2 surface

(b) Reconstructed (0001) α-quartz surface

Figure 3.5: Distribution of binding energies of oxygen on quartz and a-SiO_2 surfaces exposed to atomic oxygen.

Defects are uniquely identified by their connectivity to other atoms. For example, the NBO I defect is identified as a silicon atom that is bound to three bridging oxygen atoms and one singly coordinated oxygen atom. We use the conservative values of $D_{\mathrm{Si-O}} < 2$ Å and $D_{\mathrm{O-O}} < 1.4$ Å to define Si-O and O-O bonds respectively. As shown in Fig. 3.5, the NBO I defect and peroxyl defect are the most common defects on both surfaces. The non-bridging oxygen atom in the NBO I defect is on average bound with ∼5.5 eV of energy, which is consistent with the energy of this defect isolated on the reconstructed surface or on a small cluster of atoms.[3] However, due to the high

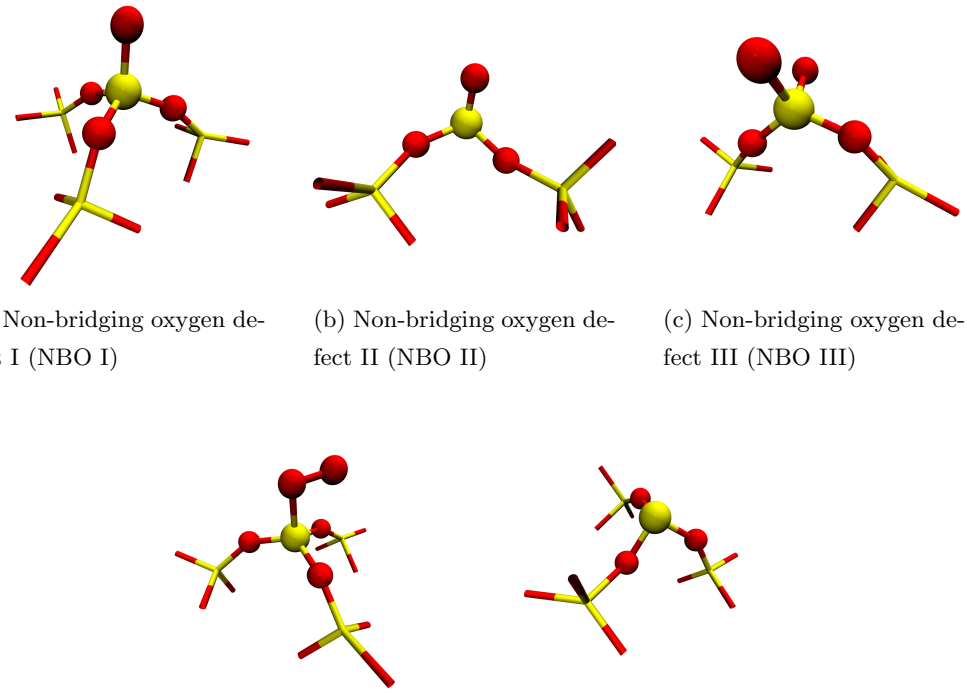

(a) Non-bridging oxygen defect I (NBO I)

(b) Non-bridging oxygen defect II (NBO II)

(c) Non-bridging oxygen defect III (NBO III)

(d) Peroxyl defect

(e) Undercoordinated silicon defect (Si-UC)

Figure 3.6: Surface Defects. Oxygen atoms are shown in red and silicon atoms are shown in yellow. Spheres are used to represent atoms directly connected to the sites, while a wire frame model is used to highlight the connectivity of the sites to the surface.

concentration of defects on the slabs, many non-bridging oxygen defects interact with other defects on the surface, increasing the overall binding energy of oxygen atoms in these configurations. This is visible as the large number of non-bridging oxygen atoms with binding energies between 6-8 eV shown in Fig. 3.5. When analyzing the concentration of defects on the slabs, we only consider those non-bridging oxygen atoms with binding energies of less than 6 eV. This is applied to all three types of non-bridging oxygen defects. As shown in Fig. 3.5, oxygen atoms in the peroxyl defect have a binding energy of either ∼4 eV (for the terminal oxygen atom in the peroxyl configuration), or ∼7.5 eV (for the middle oxygen in the peroxyl configuration). This defect identification

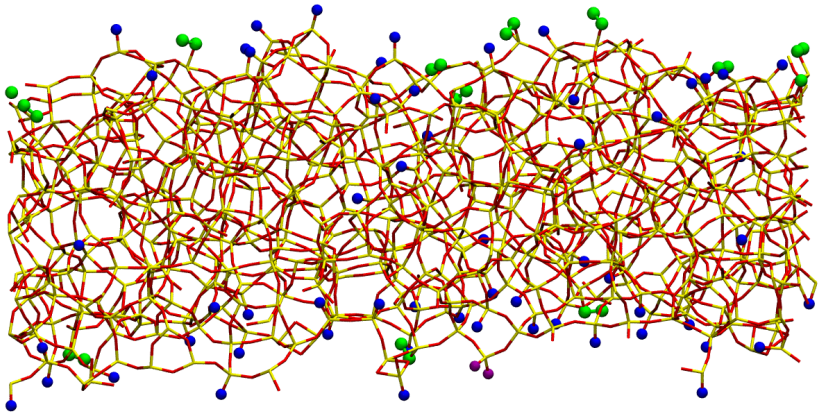

(a) a-SiO_2 slab

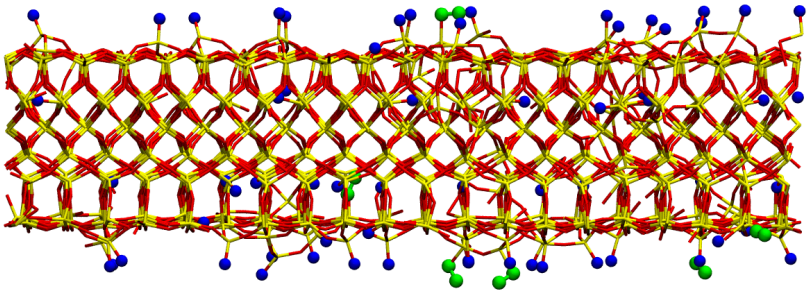

(b) Reconstructed (0001) α-quartz slab

Figure 3.7: Defects highlighted on silica surfaces after exposure to atomic oxygen. The surface is displayed in wire frame, while defects are highlighted with spheres colored by defect type. Defects are colored as NBO I (blue), NBO III (purple), peroxyl (green).

scheme gives a qualitative description of the relative number of different defects on the surface. However, it is noted that not all of the identified defects can truly be considered active sites, because some are not directly accessible to impinging gas-phase oxygen atoms (for example, Fig. 3.7 shows that a number of NBO I defects occur within the slab).

The concentration of defects on the a-SiO_2 and reconstructed (0001) α-quartz surfaces exposed to atomic oxygen at different temperatures and pressures is shown in Fig. 3.8. In all cases the a-SiO_2 surface has more defects than the quartz surface. This is in part due to the fact that the a-SiO_2 surface began with some concentration of defects before exposure to atomic oxygen (NBO I: 0.65 nm^{-2}, Si-UC: 0.62 nm^{-2}). The concentrations of defects on the a-SiO_2 surface before exposure to atomic oxygen did not vary with temperature. The total concentration of defects on the quartz surface remains relatively constant with temperature, while the total concentration of defects on the a-SiO_2 surface slightly increases at lower temperatures. Figure 3.8 also shows that the total concentration of defects on the a-SiO_2 surface also increases with pressure at 1500 K. The pressures used in these MD simulations are several orders of magnitude higher than those used in catalycity experiments (typically $\sim$100 Pa)[15], so no quantitative conclusions about the concentration of defects under experimental conditions can be drawn. However, given that the total concentration of defects increases with pressure and that the a-SiO_2 surface created with MD simulations should have more defects than real a-SiO_2 surfaces due to the short annealing time scale, we expect that the total concentration of defects here should be higher than the concentration of defects on real amorphous silica surfaces.

The undercoordinated silicon defect, NBO I defect, and peroxyl defect are similar in that they each contain a silicon atom with three bonds to the surrounding tetrahedral centers on the surface. The NBO I defect can form through the adsorption of an oxygen atom on the undercoordinated silicon defect, and the peroxyl defect can form through the adsorption of an additional oxygen atom on the NBO I defect. In contrast, the NBO II and NBO III defects both contain a silicon atom that has two bonds to the surrounding tetrahedral centers on the surface. Based on the structures present on the surfaces analyzed here, oxygen atoms adsorbing on the NBO II defect form the NBO III defect, as opposed to another type of peroxyl defect. Only one type of peroxyl defect

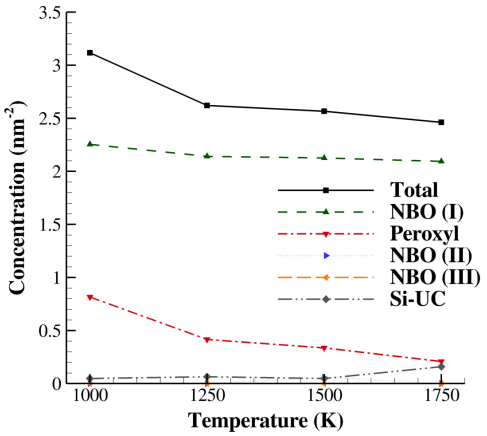

(a) a-SiO_2 surface, $P = 10$ atm, varying temperature

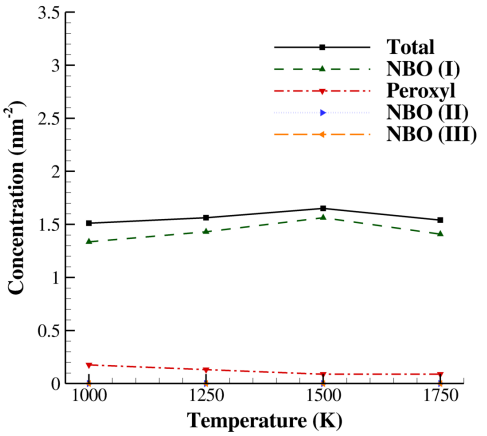

(b) Reconstructed (0001) α-quartz surface , $P = 10$ atm, varying temperature

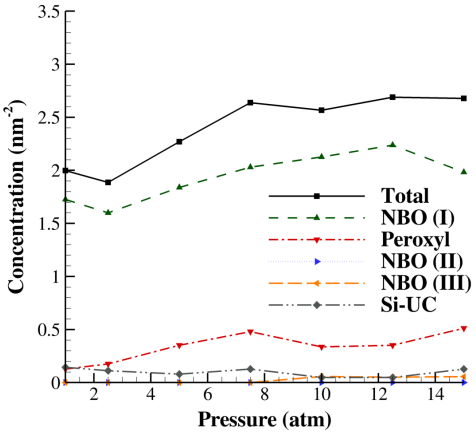

(c) a-SiO_2 surface, $T = 1500$ K, varying pressure

Figure 3.8: Concentration of defects vs. T, P

(see Fig. 3.6(d)) was observed on the surfaces analyzed here. However, we note that the ReaxFF$^{\text{GSI}}_{\text{SiO}}$ potential was not parametrized with configurations analogous to the NBO III defect, so the structure of this type of defect is not certain. The majority of defects on the surfaces presented here are either the undercoordinated silicon defect, the NBO I

defect, or the peroxyl defect under all conditions (see Fig. 3.8), so we expect that these defects will play more important roles in the surface chemistry than the NBO II and NBO III defects.

There is experimental evidence for the existence of the under-coordinated silicon defect (Si-UC) and NBO I defect on vacuum fractured quartz and a-SiO_2.[91, 92, 93] Additionally, these defects have been observed in simulations of amorphous silica surfaces using other interatomic potentials.[94, 95, 62] However, unique to the MD simulations in this work is the peroxyl defect predicted by the ReaxFF$^{\text{GSI}}_{\text{SiO}}$ potential. This defect has been experimentally identified on irradiated and mechanically ground silica in the presence of O_2.[96, 54] The peroxyl defect was not included in the training set of the ReaxFF$^{\text{GSI}}_{\text{SiO}}$ potential, and below we summarize DFT calculations from the work of Norman et al.[1] that compare the predictions of the ReaxFF$^{\text{GSI}}_{\text{SiO}}$ to the DFT results for this cluster.

3.5.1 Validation of ReaxFF$^{\text{GSI}}_{\text{SiO}}$ potential for the structure of the peroxyl defect

In the previous section we showed that the ReaxFF$^{\text{GSI}}_{\text{SiO}}$ potential predicts a peroxyl defect on quartz and amorphous silica surfaces exposed to atomic oxygen. To validate the geometry and energetics of this structure, a comparison to the results predicted by DFT were presented in the work by Norman et al.[1] For convenience these results are summarized here. Density Functional Theory results are limited to smaller systems, so the authors chose the cluster shown in Fig. 3.9 for a comparison between methods. Previous calculations have shown that clusters of this size were sufficient to represent the larger surface.[3] This cluster was created by selecting a peroxyl defect on a reconstructed (0001) α-quartz surface previously exposed to atomic oxygen and deleting all atoms more than one SiO_4 tetrahedral units away from the peroxyl defect. The oxygen atoms at the edges of this cluster were capped with hydrogen atoms to saturate the valencies for DFT calculations.

As in previous work,[3] the specific DFT model chemistry used was chosen based on which density functional and basis set best reproduced coupled cluster calculations (specifically RCCSD(T)-F12a/jun-cc-pVTZ),[70, 71] which are accurate, but not affordable for large systems. Based on a comparison of different model chemistries using

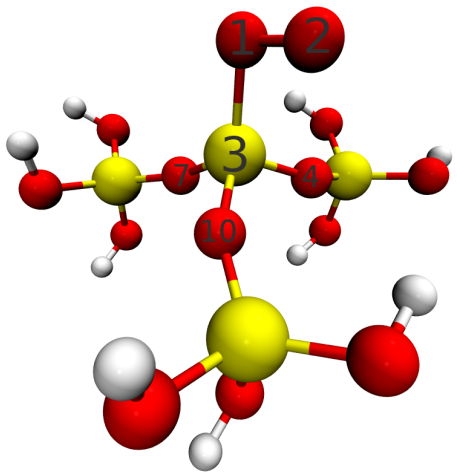

Figure 3.9: **T4O2** cluster. Hydrogen atoms are in white, oxygen atoms are in red, and silicon atoms are in yellow.

a $H_3Si\text{-}O_2$ cluster, the M06[73] density functional with the MG3S basis set[97] were chosen. Table 3.5 shows a comparison between $\text{ReaxFF}^{\text{GSI}}_{\text{SiO}}$ and M06/MG3S for various geometric parameters and for the binding energy of the O_2 molecule. For both DFT and $\text{ReaxFF}^{\text{GSI}}_{\text{SiO}}$ calculations, only the positions of atoms 1 and 2 in Fig. 3.9 were optimized. The binding energy is defined as:

$$E_{\text{binding}} = E_{\text{T}_3\text{Si-O}_2} - E_{\text{O}_2} - E_{\text{T}_3\text{Si}} \tag{3.4}$$

where T_3 represents the cluster of the structure without the adsorbed oxygen. As shown in Table 3.5, the $\text{ReaxFF}^{\text{GSI}}_{\text{SiO}}$ potential predicts bond lengths within 0.1 Å and bond angles within 10° of the values predicted by the M06/MG3S model chemistry. However, the $\text{ReaxFF}^{\text{GSI}}_{\text{SiO}}$ potential underpredicts the binding energy of the O_2 by approximately 0.9 eV. This shows that the $\text{ReaxFF}^{\text{GSI}}_{\text{SiO}}$ potential is able to reasonably predict structures outside of its training set; however, for reliable binding energies a higher level of theory (DFT) is required.

	$\text{ReaxFF}^{\text{GSI}}_{\text{SiO}}$	DFT (M06/MG3S)[1]
R(1-2) (Å)	1.225	1.333
R(1-3) (Å)	1.759	1.669
θ(2-1-3) (degrees)	96.7	105.3
θ(1-3-7) (degrees)	121.6	111.4
θ(1-3-4) (degrees)	109.8	117.11
θ(1-3-10) (degrees)	113.4	116.6
E_{binding} (eV)	-1.608	-2.567

Table 3.5: Geometric parameters and binding energy for the **T4O2** cluster. DFT results from [1]. See Fig. 3.9 for atom labels.

3.6 Conclusions

In this chapter we used molecular dynamics simulations with the $\text{ReaxFF}^{\text{GSI}}_{\text{SiO}}$ potential to identify the chemical surface structures and defects on both quartz and amorphous silica exposed to atomic oxygen at high temperature. We found that the most prevalent surface sites were a non-bridging oxygen atom defect (NBO I) and a peroxyl defect. Based on the binding energy of the oxygen atoms in these sites, we showed that both are potentially chemically active with respect of Eley-Rideal recombination. There is experimental evidence for the existence of these defects on mechanically ground and irradiated silica surfaces at low temperatures. The prediction of the peroxyl defect on silica surfaces by MD simulation is, however, unique to this work. We demonstrated that the structure of the peroxyl defect as predicted by the $\text{ReaxFF}^{\text{GSI}}_{\text{SiO}}$ potential agrees reasonably well with DFT calculations; however, the $\text{ReaxFF}^{\text{GSI}}_{\text{SiO}}$ potential underpredicts the binding energy of the O_2 molecule on this defect by 0.9 eV. The peroxyl defect was not included in the training set of the $\text{ReaxFF}^{\text{GSI}}_{\text{SiO}}$ potential, which shows the predictive value of this potential. Results of molecular dynamics simulations for surfaces exposed to atomic oxygen at a gas-phase pressure of 10 atm showed that the total concentration of defects on quartz and a-SiO_2 slabs did not vary significantly with temperature. The total concentration of defects on the a-SiO_2 surface increased with pressure over the pressure range 1-15 atm at a temperature of 1500 K. However, the gas-phase pressures

used in MD simulations were several orders of magnitude higher than those used in many experimental setups, so no quantitative conclusions about the total concentration of defects on silica surfaces under experimental conditions can be drawn. We note that some previous work on oxygen interactions with silica have used different surfaces and surface sites[44, 46] which reinforces the importance of the present work in identifying which sites on realistic silica surfaces exposed to atomic oxygen are potentially catalytic with respect to Eley-Rideal recombination.

We conclude that the defects predicted by our MD simulations are present on real silica surfaces exposed to dissociated oxygen at high temperatures, representative of surface conditions during hypersonic flight. The chemistry of the predicted surface structures is supported by density functional theory calculations, and the existence of such defects on silica surfaces is consistent with available experimental data. These defects provide a feasible pathway for the catalytic recombination of atomic oxygen. In the next chapter we show how these defects can be used as the basis for a finite rate catalytic model to describe oxygen recombination on silica surfaces.

Chapter 4

A Finite Rate Catalytic Model for Oxygen-Silica Gas-Surface Interactions

4.1 Introduction

This chapter describes the creation of a catalytic rate model for oxygen silica gas surface interactions. Our aim is to describe the surface catalyzed recombination of atomic oxygen with a system of rate equations, which can be integrated into a CFD code as a boundary condition. The rate model described in this chapter builds on the work in the previous chapter, where we determined which surface sites (or defects) on silica surfaces exposed to atomic oxygen were potentially catalytic with respect to direct gas-phase reactions. The reactions in the rate model are based on the interaction of atomic and molecular oxygen with these sites, which have been experimentally observed on silica surfaces. All rate equations take an Arrhenius form, which requires a pre-exponential factor and an activation energy for each reaction. To find Arrhenius parameters for forward reactions we use trajectory calculations with the $\mathrm{ReaxFF}^{\mathrm{GSI}}_{\mathrm{SiO}}$ potential. To find the rates of the reverse reactions we use estimates from transition state theory for the pre-exponential factors, while using energy balance to find the activation energies. Single point energies from DFT are used to calculate the activation energies of reverse

reactions because these values are expected to be more accurate than the predictions of the ReaxFF$^{\mathrm{GSI}}_{\mathrm{SiO}}$ potential for some reactions. Detailed balance is applied to the rate model to ensure that it maintains gas phase chemical equilibrium. The final rate model can be used to predict the oxygen recombination coefficient (γ_O) under different conditions, which can be compared to experimental results.

This chapter is organized as follows. Section 4.2 discusses the advantages of using a rate model, as opposed to simpler approaches, to describe gas-surface chemical reactions in CFD flow solvers. In Section 4.3 we describe the reactions that are used in the rate model and the functional forms of the rate constants. Section 4.4 describes how surface sites are represented and the results of trajectory calculations. Section 4.5 discusses how the rates of reverse reactions can be found through transition state theory and detailed balance. The results of the rate model are given in Section 4.6, and our conclusions drawn in Section 4.7.

4.2 Modeling Gas Surface Chemical Reactions in Computational Fluid Dynamics Solvers

In computational fluid dynamics solvers, there are various approaches to account for gas-surface chemical reactions and the resulting heat flux due to surface catalysis. As a lower bound for the heat flux, a non-catalytic wall boundary condition is used. This condition assumes that the surface does not alter the chemical composition of the gas. The upper limit of heating due to surface catalysis is calculated using a super catalytic wall boundary condition, which assumes that species diffusing to the wall recover their free stream enthalpy and mass fractions. However, it is possible that this boundary condition is unphysical. Because the mass fractions of species are imposed at the wall, the net flux of a species may be higher than what is allowed by kinetic theory.[9] To model heating in between these cases, the recombination of gas phase species on the surface is calculated from an experimentally based recombination coefficient (γ_O=const. or γ_O(T)). The heating on the surface is often calculated using the assumption that all of the energy released by surface catalyzed recombination is transferred to the wall (assuming a thermal accommodation coefficient of $\beta = 1$). However, there are some drawbacks to describing gas-surface chemical reactions with a recombination coefficient

based approach, which only accounts for the net effect of the surface on the gas, and not the underlying mechanisms contributing to catalysis. Moreover, to describe gas-surface chemical reactions over a range of conditions, it is necessary to have a recombination coefficient that is a function of temperature, pressure, and gas-phase compositions, data for which are not available experimentally. Additionally, an approach based on recombination coefficients alone encounters difficulties when describing gas-surface chemical reactions in situations with multiple recombining species. For example in systems containing both dissociated oxygen and dissociated nitrogen, atomic oxygen can recombine on the surface with either adsorbed oxygen (to form O_2) or adsorbed nitrogen (for form NO).[31] Thus, the recombination coefficients ($\gamma_{O,O}$, $\gamma_{O,N}$) for these two processes are not independent, and an additional preference factor would be needed to fully describe the reactions. Finally, a recombination coefficient based approach does not allow for molecules to undergo surface meditated dissociation, so such an approach can not maintain gas-phase equilibrium.

An alternative approach is to use a finite rate catalytic model, which describes surface chemistry with a system of elementary gas-surface chemical reactions, allowing for a description of surface catalytic processes from a molecular point of view. Several CFD solvers[98, 99, 100, 101, 102] already incorporate a finite rate catalytic model based approach to describe gas surface interactions. However, such an approach is only as accurate as the rates which are used in the rate model, and the parameters (such as activation energies and pre-exponential factors) which are used in the functional forms of the rate equations. There are no direct experimental results as to which reactions actually take place during gas-surface reactions, nor are there reliable data for the activation energies of these reactions. Experimental measurements typically report a recombination coefficient γ_O, which is a combination of all gas surface reactions. Some works have proposed rate models for explaining the experimental trends in recombination coefficients[6, 37], however the parameters in these models are ultimately a fit to experimental results (which as described in Chapter 2 often vary significantly from experiment to experiment). In contrast, computational chemistry calculations allow insight into which reactions contribute to gas-surface recombination and the rates of these reactions. In this chapter we focus on creating a finite rate catalytic model based on atomistic simulation of the interaction of gas phase species with the defects occurring

on realistic silica surfaces.

4.3 Description of Rate Model

The variables we use to denote gas phase and surface concentrations are shown in Table 4.1. Undercoordinated silicon atoms are called empty sites (E_s), non-bridging oxygen atoms are called adsorbed atomic oxygen (O_s), and peroxyl defects are called adsorbed molecular oxygen (O_{2s}).

Variable	Name	Units
[O]	Gas phase atomic oxygen concentration	$1/m^3$
$[O_2]$	Gas phase molecular oxygen concentration	$1/m^3$
$[O_s]$	Surface atomic oxygen concentration	$1/m^2$
$[O_{2s}]$	Surface molecular oxygen concentration	$1/m^2$
$[E_s]$	Surface empty site concentration	$1/m^2$
[S]	Total surface site concentration	$1/m^2$
θ_x	Surface coverage. (e.g. $\theta_o = [O_s]/[S]$)	
A_{site}	Area of a surface site	m^2

Table 4.1: Variables used in the rate model

The complete set of reactions we consider is given in Table 4.2. This set of reactions is based on the possible outcomes of the collision of atomic and molecular oxygen with all three surface sites.

Reaction			Reaction Name	#
$O + E_s$	$\rightleftharpoons$	O_s	Atomic Oxygen Adsorption	1
$O + O_s$	$\rightleftharpoons$	$E_s + O_2$	ER Recombination	2
$O + O_s$	$\rightleftharpoons$	O_{2s}	O_2 Formation	3
$O + O_{2s}$	$\rightleftharpoons$	$O_s + O_2$	ER Recombination II/O_2 Replacement	4
$O_2 + E_s$	$\rightleftharpoons$	O_{2s}	Molecular Oxygen Adsorption	5

Table 4.2: Reactions used in the rate model. Reactions are named by the forward reaction.

The rate equations and the functional forms of the rate constants are given in Table 4.3. All rates are given per unit area. For example, the form of a forward rate constant involving the reaction of gas phase species X with surface species Y is given by:

$$\begin{aligned}\text{Rate } (\mathrm{m^{-2}s^{-1}}) = (\text{Flux of species X to surface}) \ (\mathrm{m^{-2}s^{-1}})\times \\ (\text{Probability of X hitting surface site Y})\times \\ (\text{Probability of reaction})\end{aligned} \tag{4.1}$$

Assuming that all reaction probabilities follow an Arrhenius form ($A\ \mathrm{e}^{-E_a/(k_B T)}$) this expression becomes:

$$\text{Rate } (\mathrm{m^{-2}s^{-1}}) = ([\mathrm{X}]\bar{\mathrm{c}}_\mathrm{X}/4) \times (\mathrm{A_{site}[Y]}) \times (\mathrm{A_n^f e^{-E_n^f/(k_B T)}}) \tag{4.2}$$

where A_{site} is the area of a surface site and $\bar{c}_X$ is the average gas phase speed of a species X:

$$\bar{c}_X = \left(\frac{8k_B T}{\pi m_X}\right)^{1/2} \tag{4.3}$$

The primary purpose of trajectory calculations is to find the pre-exponential factors (A_n^f) and activation energies (E_n^f) of forward reactions. It is also possible to use potential energy surfaces to find the activation energies. For example, based on previous DFT results alone, the atomic oxygen adsorption reaction is non-activated.[3] However, trajectory calculations are useful for determining the reaction preference when a reaction has two possible outcomes. For example the collision of gas phase atomic oxygen

with adsorbed atomic oxygen (O + O_s) can lead to either ER recombination (reaction 2 in Table 4.2) or O_2 formation (reaction 3 in Table 4.2)). Additionally, the results of trajectory calculations in conjunction with the rate model can be used to determine a thermal accommodation coefficient (β) for the recombination of oxygen (however this will not be covered in this work).

Rate	Rate Equation	Rate Constant (k_i)	Rate Constant Units
r_1^f	$k_1^f[\mathrm{O}][\mathrm{E}_s]$	$(\bar{c}_O/4) \times A_{\mathrm{site}} \times (A_1^f \mathrm{e}^{-E_1^f/(K_B T)})$	m^3/s
r_1^r	$k_1^r[\mathrm{O}_s]$	$A_1^r \mathrm{e}^{-E_1^r/(K_B T)}$	$1/\mathrm{s}$
r_2^f	$k_2^f[\mathrm{O}][\mathrm{O}_s]$	$(\bar{c}_O/4) \times A_{\mathrm{site}} \times (A_2^f \mathrm{e}^{-E_2^f/(K_B T)})$	m^3/s
r_2^r	$k_2^r[\mathrm{O}_2][\mathrm{E}_s]$	$(\bar{c}_{O_2}/4) \times A_{\mathrm{site}} \times (A_2^r \mathrm{e}^{-E_2^r/(K_B T)})$	m^3/s
r_3^f	$k_3^f[\mathrm{O}][\mathrm{O}_s]$	$(\bar{c}_O/4) \times A_{\mathrm{site}} \times (A_3^f \mathrm{e}^{-E_3^f/(K_B T)})$	m^3/s
r_3^r	$k_3^r[\mathrm{O}_{2s}]$	$A_3^r \mathrm{e}^{-E_3^r/(K_B T)}$	$1/\mathrm{s}$
r_4^f	$k_4^f[\mathrm{O}][\mathrm{O}_{2s}]$	$(\bar{c}_O/4) \times A_{\mathrm{site}} \times (A_4^f \mathrm{e}^{-E_4^f/(K_B T)})$	m^3/s
r_4^r	$k_4^r[\mathrm{O}_2][\mathrm{O}_s]$	$(\bar{c}_{O_2}/4) \times A_{\mathrm{site}} \times (A_4^r \mathrm{e}^{-E_4^f/(K_B T)})$	m^3/s
r_5^f	$k_5^f[\mathrm{O}_2][\mathrm{E}_s]$	$(\bar{c}_{O_2}/4) \times A_{\mathrm{site}} \times (A_5^f \mathrm{e}^{-E_5^f/(K_B T)})$	m^3/s
r_5^r	$k_5^r[\mathrm{O}_{2s}]$	$A_5^r \mathrm{e}^{-E_5^r/(K_B T)}$	$1/\mathrm{s}$

Table 4.3: Rate constants and functional forms

Given the set of rate equations in Tables 4.2 and 4.3, the change in surface concentrations with respect to time is given by the sum of the appropriate rates:

$$\frac{d[\mathrm{O_s}]}{dt} = r_1^f - r_1^r - r_2^f + r_2^r - r_3^f + r_3^r + r_4^f - r_4^r \tag{4.4}$$

$$\frac{d[\mathrm{O_{2s}}]}{dt} = r_3^f - r_3^r - r_4^f + r_4^r + r_5^f - r_5^r \tag{4.5}$$

The total concentration of surface sites is conserved:

$$[\mathrm{O_s}] + [\mathrm{O_{2s}}] + [\mathrm{E_s}] = [\mathrm{S}] \tag{4.6}$$

We are interested in the rates of surface reactions at steady state surface concentrations, which have time to develop during sustained hypersonic flight:

$$\frac{d[\mathrm{O_s}]}{dt} = 0, \frac{d[\mathrm{O_{2s}}]}{dt} = 0 \tag{4.7}$$

Solving Eqs. 4.4-4.5 using a time marching approach, we have found that steady state surface coverages develop over microsecond time scales. To reduce the computational cost of the unsteady time marching approach, we solve this system of equations using a Newton-Raphson solver:

$$\begin{bmatrix} [\mathrm{O_s}] \\ [\mathrm{O_{2s}}] \end{bmatrix}_{k+1} = \begin{bmatrix} [\mathrm{O_s}] \\ [\mathrm{O_{2s}}] \end{bmatrix}_{k} - J^{-1} f \tag{4.8}$$

where:

$$f = \begin{bmatrix} r_1^f - r_1^r - r_2^f + r_2^r - r_3^f + r_3^r + r_4^f - r_4^r \\ r_3^f - r_3^r - r_4^f + r_4^r + r_5^f - r_5^r \end{bmatrix}, J = \begin{bmatrix} \frac{\partial f_1}{\partial [O_s]} & \frac{\partial f_1}{\partial [O_{2s}]} \\ \frac{\partial f_2}{\partial [O_s]} & \frac{\partial f_2}{\partial [O_{2s}]} \end{bmatrix} \tag{4.9}$$

Equation 4.8 is iteratively computed until there is no significant change in the concentrations of surface species. To compare with experimental results, we compute the recombination coefficient, γ_O, which is defined as:

$$\gamma_O = \frac{r_1^f + r_2^f + r_3^f + r_4^f - r_1^r - r_2^r - r_3^r - r_4^r}{[\mathrm{O}]\bar{c}_\mathrm{O}/4} \tag{4.10}$$

where all of the rates are computed with the steady state surface coverages.

4.4 Trajectory Calculations

To represent surface sites, we use a cluster consisting of 370 atoms which has been carved out from a lager reconstructed (0001) α-quartz surface with one central non-bridging oxygen defect, as shown in Fig. 4.1. This cluster is representative of the defects occurring on both quartz and a-SiO_2 surfaces, which were found to have similar binding energies (see Chapter 3, Fig. 3.5). A cluster of this size is needed to represent the PES of both the site and the surrounding surface. The surface defect can be changed to the undercoordinated silicon defect by deleting the top oxygen atom, or changed to a peroxyl defect by adding an oxygen atom above the non-bridging oxygen atom and performing an energy minimization. We found that using larger clusters did not affect the results of trajectory calculations or single point energy calculations.

In a gas-surface system, impinging gas phase species have the opportunity to hit surface sites at a variety of incident angles and impact factors. The impact factor is

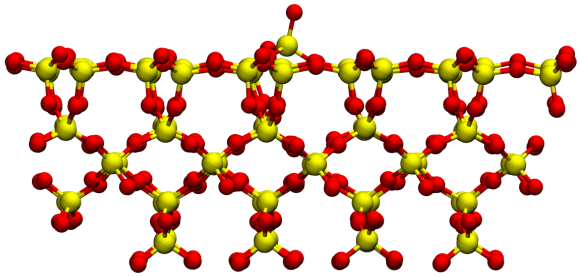

Figure 4.1: Cluster of 370 atoms with one central defect

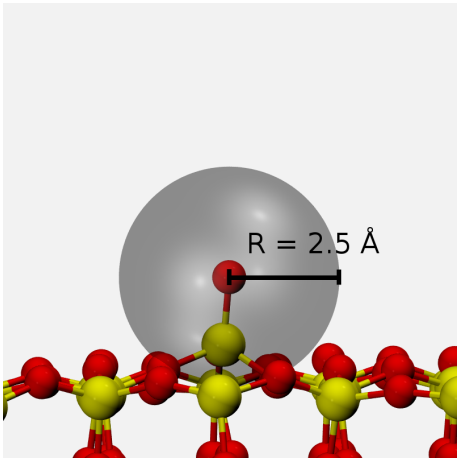

(a) Sites are considered as spheres having a radius of 2.5 Å, represented by the gray sphere

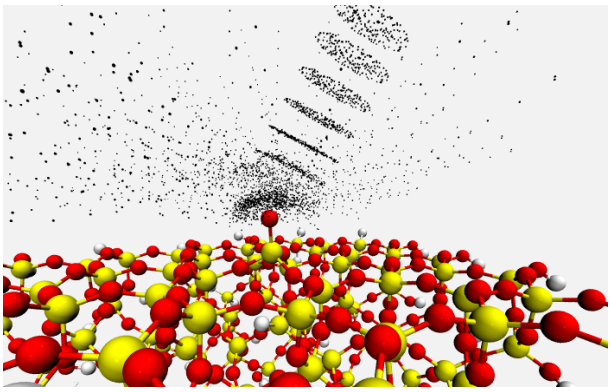

(b) Off normal collisions at ϕ= 30^o for the O + O$_s$ reaction. Positions of impinging atoms shown every 250 time steps in black. Cluster is frozen in its minimum energy configuration

Figure 4.2: Three-dimensional surface sites

defined as the distance of closest approach between the center of the impinging species and center of the surface site if there were zero interatomic potential. We define a spherical coordinate system where the angle ϕ is the angle between a vector and the surface normal vector, and the angle θ is the angle between the x-axis (which is parallel

to the surface) and the projection of a vector on to the surface. To account for the possibility of both normal and off-normal collisions, we approximate a surface site as a sphere resting on a flat surface, as shown in Fig. 4.2(a) for the non-bridging oxygen defect. In the case of the peroxyl defect this sphere is centered on the oxygen atom directly bonded to the surface, while for an undercoordinated silicon defect this sphere is centered on the location of the adsorption minimum of atomic oxygen. Based on the potential energy surfaces of atomic oxygen interacting with the defects, we have chosen a site radius (r_{site}) of 2.5 Å (for example, see Fig. 4.3(b)). For the purpose of the rate model, it is necessary to find the effective area of spherical sites, which is discussed below.

From Vincenti and Kruger[103], at thermal equilibrium the flux of atoms of species [X] hitting a flat surface is:

$$F_s = [X]\left(\frac{m_X}{2\pi k_B T}\right)^{\frac{3}{2}} \int_{-\infty}^{\infty}\int_{-\infty}^{\infty}\int_{0}^{\infty}(C_3)f(C_i)dC_1dC_2dC_3 \tag{4.11}$$

where C_i is an individual velocity component, and the surface normal vector is parallel to C_3. Converting to spherical coordinates, this becomes:

$$F_s = [X]\left(\frac{m_X}{2\pi k_b T}\right)^{\frac{3}{2}} \int_{0}^{\pi/2} sin(\phi)cos(\phi)d\phi \int_{0}^{2\pi} d\theta \int_{0}^{\infty} C^3 e^{-mC^2/2k_B T}dC \tag{4.12}$$

If sites are considered as two-dimensional discs resting on the surface, the flux of impinging atoms hitting surface sites [Y] is:

$$F_{\text{site,2D}} = \frac{[X]\overline{c}_x}{4} \times ([\text{Y}] * \pi \times \text{r}_{\text{site}}^2) \tag{4.13}$$

Where [Y] is the concentration of sites on the surface (m^{-2}). However, if we consider sites as spheres resting on a surface, the effective area of the site varies with the incident angle of the impinging atom (ϕ). The effective area of a spherical site is the area of the orthographic 'shadow' cast by the site, which is an ellipse with an area of $\pi r_{\text{site}}^2/cos(\phi)$. Considering this, the flux of atoms hitting three dimensional spherical sites is given by:

$$F_{\text{site,3D}} = ([\text{Y}] * \pi \times \text{r}_{\text{site}}^2)[\text{X}]\left(\frac{\text{m}_\text{X}}{2\pi \text{k}_\text{b}\text{T}}\right)^{\frac{3}{2}} \int_{0}^{\pi/2} \sin(\phi)\text{d}\phi \int_{0}^{2\pi} \text{d}\theta \int_{0}^{\infty} \text{C}^3 \text{e}^{-\text{mC}^2/2\text{k}_\text{B}\text{T}}\text{dC} \tag{4.14}$$

which is:

$$F_{\text{site,3D}} = \left(\frac{[\text{X}]\bar{c}_{\text{X}}}{4}\right)\left([Y]2\pi r_{\text{site}}^2\right) = 2F_{site,2D} \tag{4.15}$$

Therefore, for the purpose of the rate model, we will consider the area of a site to be $A_{\text{site}} = 2\pi r_{\text{site}}^2$.

For trajectory calculations, the velocities of impinging atoms are sampled from the Maxwell-Boltzmann distribution for atoms passing through a plane in one direction, as described by Garcia and Wagner[90]:

$$C_1 = \sqrt{\frac{k_B T}{m_X}} R_G \tag{4.16}$$

$$C_2 = \sqrt{\frac{k_B T}{m_X}} R_G \tag{4.17}$$

$$C_3 = -\sqrt{\frac{2k_B T}{m_X}} \sqrt{-\log R_U} \tag{4.18}$$

$$\tag{4.19}$$

where R_G is a random number sampled from a normal Gaussian distribution with zero mean and unit variance, and R_U is a uniformly distributed random number between zero and one. The velocities C_1, C_2, and C_3 dictate the angles (ϕ, θ) that a species impinges towards the surface with. Atoms are randomly placed within a disc of radius of r_{site} at a distance of 10 Å above the surface. For example, a set of trajectories at ϕ = 30^o and $\theta = 0^o$ is shown in Fig. 4.2(b).

Trajectory calculations are carried out as follows. All trajectory calculations are performed with the LAMMPS molecular dynamics program[57] with a time step of 0.25 fs. Atoms at the edge of the cluster are kept fixed, while atoms adjacent to these are thermalized with the Langevin thermostat to maintain the temperature of the cluster over the course of a trajectory calculations. Atoms in a cluster are given initial velocities sampled from the Maxwell-Boltzmann distribution at the desired temperature. Before the impinging species is added to the system, the positions of atoms in the cluster are integrated for 0.5 ps with LAMMPS. We found that this was sufficient to randomize the initial positions and velocities of the atoms in the cluster, and that longer initial integration times did not change the results of simulations. The impinging species was then added to the simulation and given a velocity, position, and impact angle as described above. The simulation was propagated until the impinging species collided

with the surface site, and then for an additional 0.5 ps to allow the system to reach a final state. The outcome of a reaction was determined by the final positions and connectivity of the atoms. The averaged results of many trajectory calculations were used to find the probability of a reaction vs. temperature, which can be used to find the pre-exponential factor and activation energy. The results of trajectory calculations for all of the forward reactions in Table 4.2 are given below.

4.4.1 Atomic Oxygen Adsorption ($O + E_s \rightarrow O_s$)

A diagram of this reaction is shown in Fig. 4.3(a). A 2D potential energy surface for this reaction, which is created by rastering the atom on a plane perpendicular to the surface, is shown in Fig. 4.3(b). In this PES, and all subsequent potential energy surfaces, zero potential energy is defined as when the gas phase species is an infinite distance away from the surface. As shown in Fig. 4.3(b), there is no barrier for the adsorption of atomic oxygen for this reaction. The results of trajectory calculations in Fig. 4.4 show that the probability of this reaction is nearly unity, and does not vary significantly with temperature. Oxygen atoms that do not adsorb are scattered back to the gas phase. The weak trend with temperature that is seen in Fig. 4.4 is due to the slightly repulsive regions surrounding the surface site. Impinging oxygen atoms with high incident angles and more energy have a higher probability of penetrating these regions to reach the adsorption minimum than lower energy atoms. The uncertainty in the reaction probabilities in Fig. 4.4 is estimated with the Wald method[104], with a 95% confidence interval. According to the ReaxFF$^{\mathrm{GSI}}_{\mathrm{SiO}}$ potential this reaction is exothermic with ΔE_1 = -5.01 eV for the reaction on the cluster in Fig. 4.1. This single point energy, and all subsequent single point energies, are calculated by taking the difference in the potential energies of the products and reactants. In single point ReaxFF$^{\mathrm{GSI}}_{\mathrm{SiO}}$ energy calculations, the positions of all atoms in the system other than those at the edges of the cluster are optimized. The value predicted by the the ReaxFF$^{\mathrm{GSI}}_{\mathrm{SiO}}$ potential is similar to the value predicted by DFT calculations (ΔE_1 = -5.09 eV, taken from [2]). For the rate model, we also need the activation energy of the reverse reaction (atomic oxygen desorption). The activation energy for the reverse reaction is calculated as E_1^r = -ΔE^1 + E_1^f = 5.00 eV. If using the DFT value, this value is E_1^r = 5.10 eV. The activation energies of all other reverse reactions are calculated similarly.

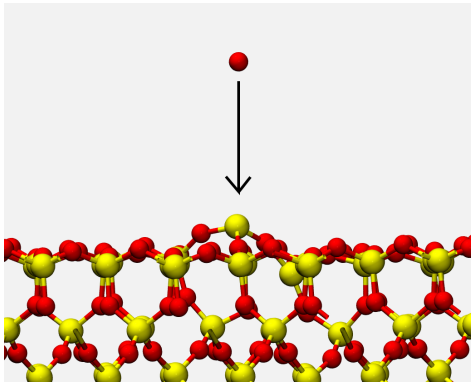

(a) Diagram of atomic oxygen adsorption reaction

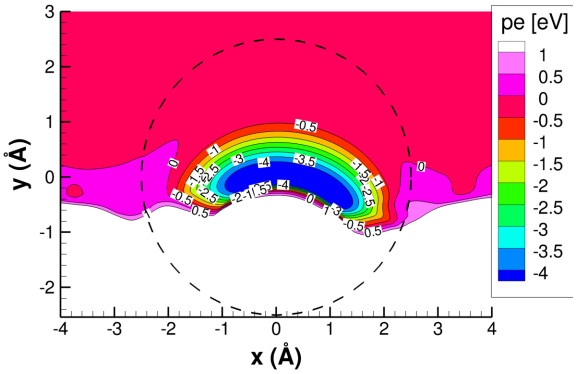

(b) Potential Energy Surface. Plot origin centered at adsorption minimum. The dotted circle has a radius of 2.5 Å, and represents the radius of the site

Figure 4.3: Atomic oxygen adsorption

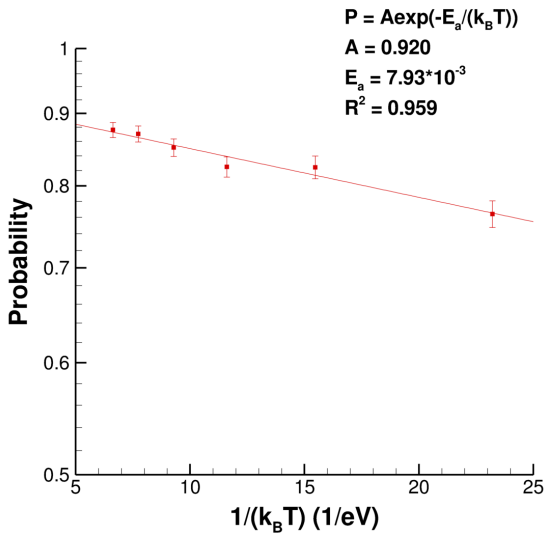

Figure 4.4: Probability of atomic oxygen adsorption reaction vs. $1/(k_BT)$

4.4.2 ER Recombination ($O + O_s \rightarrow E_s + O_2$) and O_2 Formation ($O + O_s \rightarrow O_{2s}$)

A gas phase oxygen atom colliding with a non-bridging oxygen atom can react to form gas phase molecular oxygen (ER recombination), or bond to the non-bridging oxygen on the surface to form the peroxyl defect (O_2 Formation). A diagram of this reaction is shown in Fig. 4.5(a), and the potential energy surface for this reaction is shown in Fig. 4.5(b). There are two adsorption minima, corresponding to two different geometries of the peroxyl defect, and there is no significant energy barrier for the approach of atomic oxygen to the cluster. As shown in Fig. 4.6, the probability of O_2 formation does not vary significantly with temperature, and is much higher than the probability of ER recombination. The ER recombination reaction is an activated process, with an activation energy of $E_2^f = 0.279$ eV.

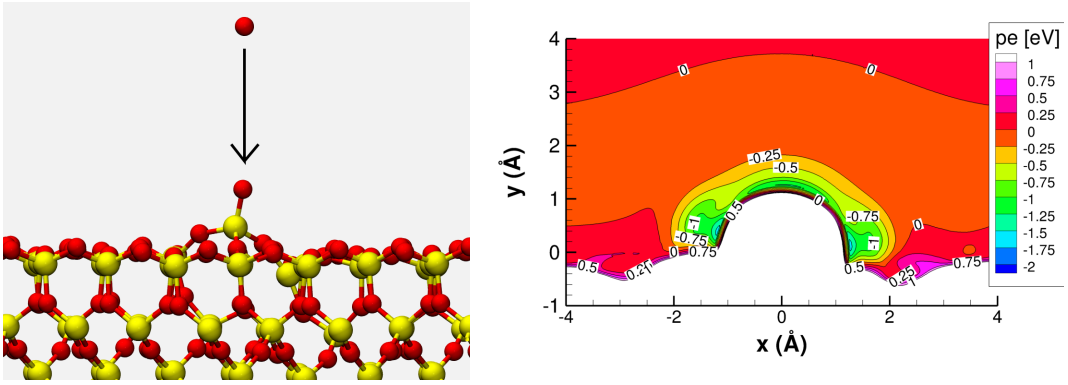

(a) Diagram of reaction

(b) Potential Energy Surface. Plot origin centered on the non-bridging oxygen atom

Figure 4.5: ER Recombination/O_2 Formation

Single point potential energies from the ReaxFF$^{GSI}_{SiO}$ and DFT[2] are shown in Fig. 4.6(b). According to the ReaxFF$^{GSI}_{SiO}$ potential, the energy change in the O_2 formation reaction is ΔE_3 = -2.48 eV. This value is slightly higher than the value predicted by DFT (ΔE_3 = -2.66 eV[2]). According to the ReaxFF$^{GSI}_{SiO}$ potential, the ER Recombination reaction is ΔE_2 = -1.19 eV. This value is significantly lower than the value predicted by DFT (ΔE_2 = -0.10 eV[2]). The differences between DFT and the ReaxFF$^{GSI}_{SiO}$ potential arise

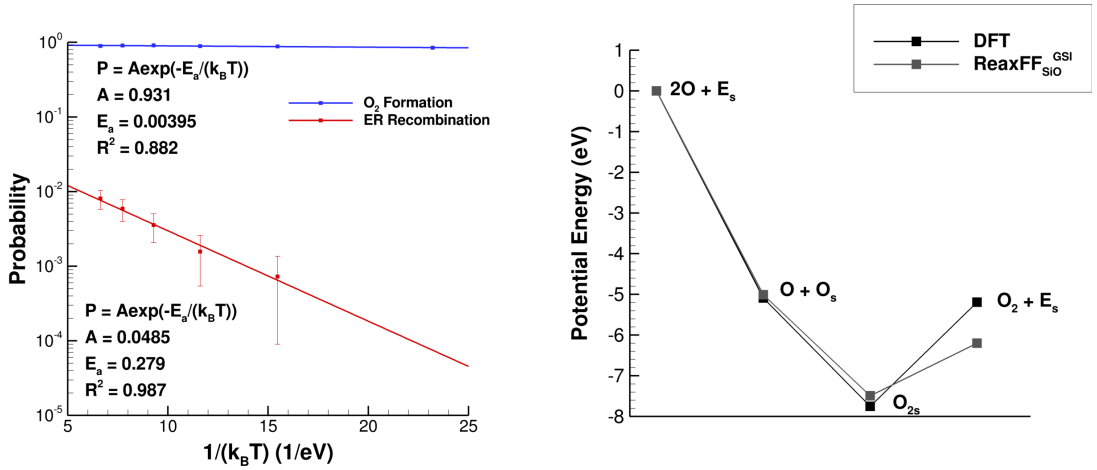

(a) Probability of the O_2 formation and ER recombination reactions vs. $1/(k_BT)$

(b) Potential Energy of O_2 Formation and ER Recombination. DFT values from [2]

Figure 4.6: Results for the O_2 Formation and ER Recombination reactions

from the fact that the ReaxFF$^{\text{GSI}}_{\text{SiO}}$ potential over-predicts the O_2 bond energy (E_{bond} = 6.20 eV). It is difficult to predict how the probability of the ER recombination reaction would be altered if the ReaxFF$^{\text{GSI}}_{\text{SiO}}$ potential were more accurate. It is possible that the probability ER Recombination reaction would be even lower because ReaxFF$^{\text{GSI}}_{\text{SiO}}$ potential predicts that this reaction is more exothermic than it should be according DFT results.

4.4.3 O_2 Replacement/ER Recombination II ($O + O_{2s} \rightarrow O_s + O_2$)

When a gas phase oxygen atom collides with a peroxyl defect, it can replace the O_2 on the surface (O_2 replacement) or combine with the terminal oxygen atom in the peroxyl defect to form gas phase molecular oxygen (ER Recombination II). The products of both reactions are the same. A diagram of this reaction is shown in Fig. 4.7(a), and the potential energy surface is shown in Fig. 4.7(b). There is no significant barrier for the approach of the oxygen atom to the adsorbed oxygen molecule. The PES in Fig. 4.7(b) shows that there is a potential energy minimum, which indicates that three oxygen atoms (which we call O_{3s}) can adsorb on the surface.

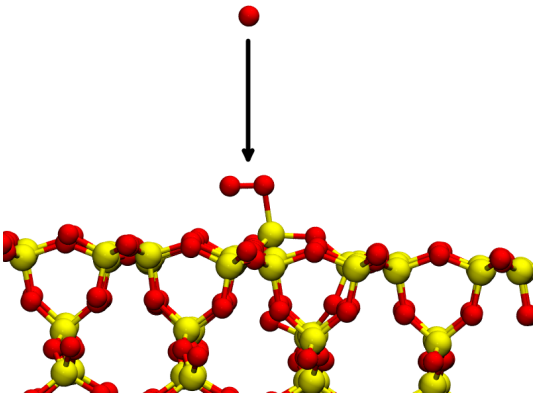

(a) Diagram of reaction

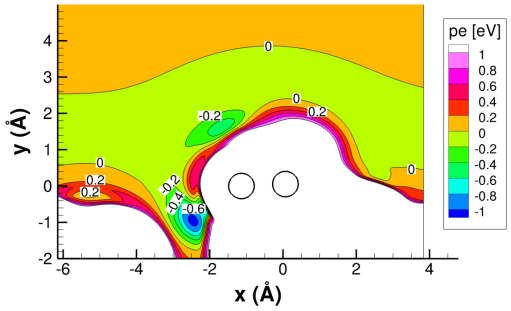

(b) Potential Energy Surface. Black circles represent locations of oxygen atoms in the peroxyl defect

Figure 4.7: Results for O_2 Replacement/ER Recombination II reactions

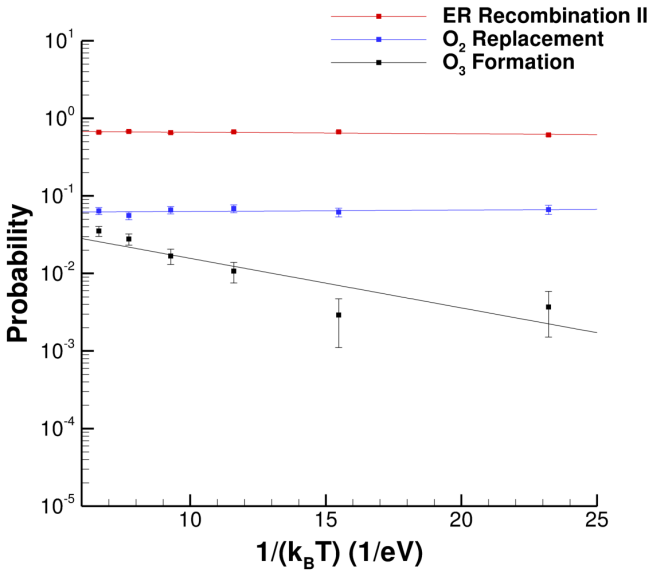

Figure 4.8: Probability of reactions vs. $1/(k_BT)$

The results of trajectory calculations are shown in Fig. 4.8. The two most probable

reactions are ER Recombination II and O_2 Replacement. Additionally, Fig. 4.8 shows that there is a small probability of O_{3s} forming, and that the probability of O_{3s} formation decreases with temperature. After selected trajectory calculations where O_{3s} formed, we performed an energy minimization to analyze the final state of the O_3 molecule. We found that the majority of adsorbed O_3 took configurations similar to the geometry shown in Fig. 4.9, with a clearly defined oxygen molecule interacting with a non-bridging oxygen atom.

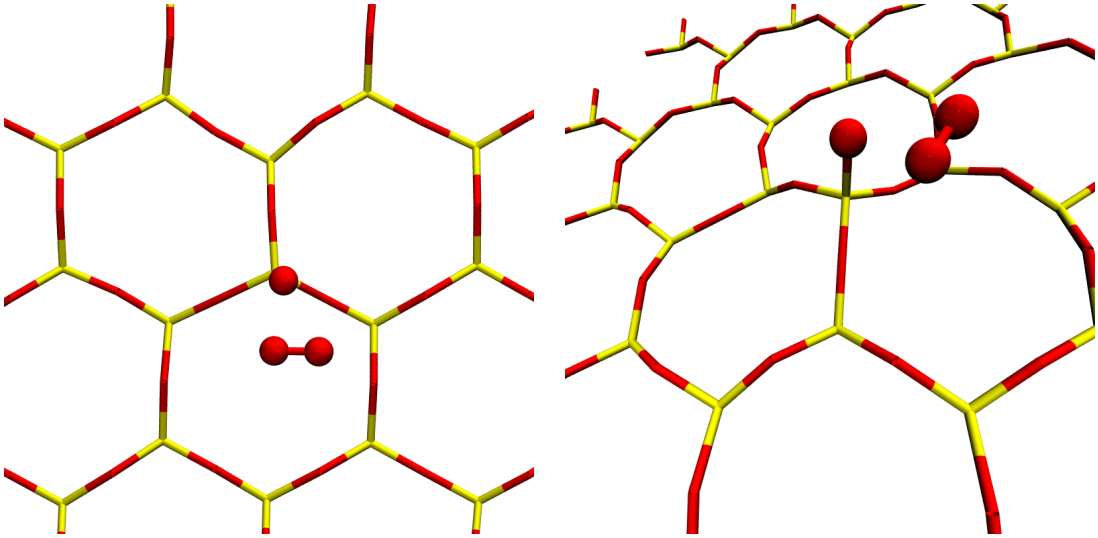

(a) Top view (b) Side view

Figure 4.9: Adsorbed O_3. Distance between oxygen atoms is 1.13 Å, 1.8 Å, and 2 Å. The top layer of the cluster is displayed in wire frame

The formation of O_{3s} is somewhat surprising because the reaction $O+O_{2s} \rightarrow O_2 + O_s$ is very exothermic. For example, Fig. 4.10 shows the potential energy change for this reaction with the O_{3s} geometry displayed in Fig. 4.9. The DFT values are for a geometry predicted by DFT optimization of the three adsorbed oxygen atoms. Evidently, the surface of the cluster is capable of rapidly damping the energy released by O_{3s} formation to keep an O_2 molecule from desorbing. However, DFT predicts that the difference in energy between the O_{3s} and $O_2 + O_s$ is much smaller (Δ E = 0.11 eV[2]) than the value predicted by the ReaxFF$^{GSI}_{SiO}$ potential (Δ E = 0.65 eV). Therefore, we expect that trajectory calculations with the ReaxFF$^{GSI}_{SiO}$ are significantly over-predicting the probability of O_{3s} forming on the surface. We will consider reactions that result in O_{3s} as actually forming gas phase molecular oxygen, an identical result to the O_2 Replacement or ER Recombination II reactions. It may be necessary to consider the O_{3s} as a surface species at lower temperatures, however at present this species will not be included in the rate model.

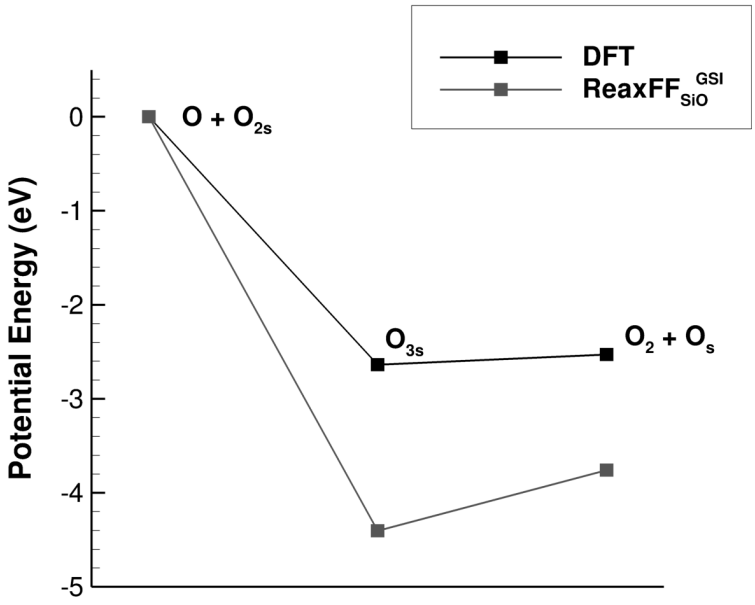

Figure 4.10: Energy of O + O_{2s}, O_{3s}, O_2 + O_s. DFT values are from [2]

For the purposes of the rate model, we add the probabilities of O_2 replacement, ER Recombination II, and O_3 formation to find the probability of the reaction ($O + O_{2s} \rightarrow O_2 + O_s$). This yields a reaction that has a pre-exponential factor of $A_4^f = 0.784$ and an activation energy of $E_4^f = 5.02\times10^{-3}$ eV. According to the $\text{ReaxFF}_{\text{SiO}}^{\text{GSI}}$ potential, the energy change in the reaction is ΔE_4 = -3.75 eV, which is higher than the value predicted by DFT (ΔE_4 = -2.53 eV).[2]

4.4.4 Molecular Oxygen Adsorption ($O_2 + E_s \rightarrow O_{2s}$)

A diagram of this reaction is shown in Fig. 4.11(a). Previous DFT/$\text{ReaxFF}_{\text{SiO}}^{\text{GSI}}$ results showed that there is a potential energy barrier for both parallel and perpendicular approaches of O_2 to the under-coordinated silicon defect.[3] However, it is possible that there are pathways for this reaction that have no energy barrier. The results of trajectory calculations are shown in Fig. 4.11(b). For trajectory calculations the molecular rotational and vibrational energies are sampled from the quantum rigid rotor/harmonic oscillator distributions. As shown in Fig. 4.11(b), the probability of the O_2 adsorption reaction does not change significantly with temperature. The pre-exponential factor for this reaction is $A_5^f = 0.239$, and the activation energy is $E_5^f = 0.0387$ eV. The $\text{ReaxFF}_{\text{SiO}}^{\text{GSI}}$ potential underpredicts the binding energy of the O_2 molecule ΔE_5 = -1.18 eV (the DFT value is ΔE_5 = -2.56 eV[2], taken from Table 2, Cluster C).

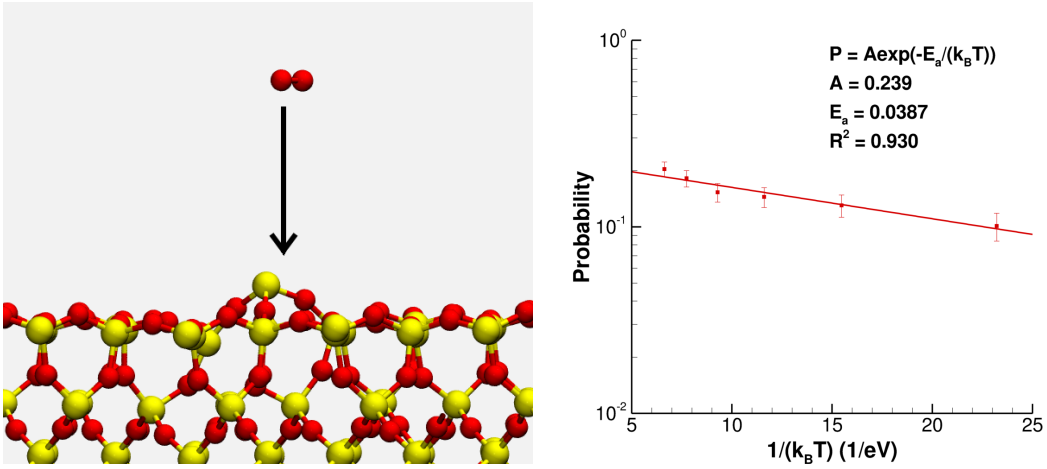

(a) Diagram of reaction (b)

Figure 4.11: Results for molecular oxygen adsorption

4.5 Finding the Rates of Reverse Reactions

The activation energies of the forward and reverse reactions, as well as the pre-exponential factors for the forward reactions are given in Table 4.4. The activation energies of the reverse reactions based on $\text{ReaxFF}^{\text{GSI}}_{\text{SiO}}$ and DFT are significantly different. We will use the values predicted by DFT, which are expected to be much more accurate. To complete the rate model, we need estimates of the pre-exponential factors for the reverse reactions. The reverse reactions are relatively endothermic and difficult to simulate with molecular dynamics due to the rarity or long time scales of these reactions. Therefore, we will use estimates of the pre-exponential factors from within a reasonable range to determine select reverse rate constants, and apply detailed balance to find the remaining reverse rate constants.

For the reverse reactions that involve gas surface collisions, the pre-exponential factors should fall between zero and one. For reactions that involve desorption, pre-exponential factors are estimated from transition state theory (TST) as between 10^{13} - 10^{15} (s^{-1}), as described by Lieberman and Lichtenberg.[55] It would be possible to pick all of the pre-exponential factors from the reverse reactions from within these reasonable

	ReaxFF$^{\mathrm{GSI}}_{\mathrm{SiO}}$				DFT	
n	A^f_n	E^f_n (eV)	Δ E_n (eV)	E^r_n (eV)	Δ E_n (eV)	E^r_n (eV)*
1	0.92	7.93×10^{-3}	-5.01	5.00	-5.09	5.08
2	0.0485	0.279	-1.18	1.46	-0.10	0.379
3	0.931	3.95×10^{-3}	-2.48	2.48	-2.66	2.66
4	0.795	6.23×10^{-3}	-3.75	3.74	-2.53	2.52
5	0.239	0.0387	-1.29	1.33	-2.56	2.53

Table 4.4: Energetics of reactions according to ReaxFF$^{\mathrm{GSI}}_{\mathrm{SiO}}$ and DFT.[2]
* calculated as -$\Delta\mathrm{E}_n$ (from DFT) + E^f_n (from ReaxFF$^{\mathrm{GSI}}_{\mathrm{SiO}}$)

bounds. However, when putting a gas-surface chemical rate model into a continuum level simulation, it is desirable to have a rate model that maintains detailed balance and gas-phase chemical equilibrium. To make sure the rate model maintains detailed balance, we will pick values for two of the pre-exponential factors of reverse reactions, and use detailed balance to find the rate constants of the three remaining rate constants of reverse reactions.

Detailed balance is applied to the rate model as described in the work by Sorenson, Valentini, and Schwartzentruber.[99] The equilibrium constants for the five reactions in the rate model are given by the following equations:

$$K_1^{eq} = \frac{[\mathrm{O_s}]}{[\mathrm{O}][\mathrm{E_s}]} \tag{4.20}$$

$$K_2^{eq} = \frac{[\mathrm{E_s}][\mathrm{O_2}]}{[\mathrm{O}][\mathrm{O_s}]} \tag{4.21}$$

$$K_3^{eq} = \frac{[\mathrm{O_{2s}}]}{[\mathrm{O}][\mathrm{O_s}]} \tag{4.22}$$

$$K_4^{eq} = \frac{[\mathrm{O_2}][\mathrm{O_s}]}{[\mathrm{O}][\mathrm{O_{2s}}]} \tag{4.23}$$

$$K_5^{eq} = \frac{[\mathrm{O_{2s}}]}{[\mathrm{E_s}][\mathrm{O_2}]} \tag{4.24}$$

We also include the rate constant for gas phase dissociation:

$$K_6^{eq} = \frac{[\mathrm{O}]^2}{[\mathrm{O_2}]} \tag{4.25}$$

Multiplying equations (4.20) and (4.21) we find an expression relating reactions (1) and (2):

$$\frac{1}{K_6^{eq}} = K_1^{eq} K_2^{eq} \tag{4.26}$$

Multiplying equations (4.22) and (4.23) we find an expression relating reactions (3) and (4):

$$\frac{1}{K_6^{eq}} = K_3^{eq} K_4^{eq} \tag{4.27}$$

Multiplying (4.20) and (4.22), then dividing by (4.24) be find an expression relating reactions (1),(3), and (5):

$$\frac{1}{K_6^{eq}} = \frac{K_1^{eq} K_3^{eq}}{K_5^{eq}} \tag{4.28}$$

Equations (4.26), (4.27), and (4.28) serve as the means to apply detailed balance to find the rate constants for the reverse reactions. An equilibrium constant is the ratio of two rate constants:

$$K_x^{eq} = \frac{k_x^f}{k_x^r} \tag{4.29}$$

With this in mind equation (4.26) becomes:

$$\frac{1}{K_6^{eq}} = \frac{k_1^f}{k_1^r} \frac{k_2^f}{k_2^r} \tag{4.30}$$

There are two unknowns in this equation: k_1^r and k_2^r. We can set the value for one rate constant by using a pre-exponential factor in a reasonable range, and use the equation for detailed balance to solve for the other rate constant. According to equations 4.26-4.28, only two reverse rate constants need to be chosen to determine the other three rate constants in this system of equations. When applying detailed balance, we therefore specify A_1^r and A_3^r to find k_1^r and k_3^r, while the remaining reverse rate constants are found through:

$$k_2^r = k_2^f K_1^{eq} K_6^{eq} = \frac{k_2^f k_1^f}{k_1^r} K_6^{eq} \tag{4.31}$$

$$k_4^r = k_4^f K_3^{eq} K_6^{eq} = \frac{k_4^f k_3^f}{k_3^r} K_6^{eq} \tag{4.32}$$

$$k_5^r = \frac{k_5^f}{K_1^{eq} K_3^{eq} K_6^{eq}} = \frac{k_5^f k_1^r k_3^r}{k_1^f k_3^f} \frac{1}{K_6^{eq}} \tag{4.33}$$

In addition to ensuring that detailed balance is obeyed at equilibrium, this method acts as a sanity check for the reverse reactions in the rate model: if the parameters used in the the chosen rate constants are selected from within reasonable bounds, so should the parameters in the rate constants determined from detailed balance. The equilibrium constant for the gas phase concentration of atomic and molecular oxygen is given by:

$$ln(K_p) = \frac{-\Delta G}{RT} \tag{4.34}$$

We find ΔG by using the partition functions of atomic oxygen and harmonic-oscillator rigid-rotor molecular oxygen with the first few electronic energy levels included, as described by McQuarrie (pp. 148).[105] As a validation, this equilibrium constant was compared to the predictions of NASA's CEA program[106] and found to be in excellent agreement over the temperature range 300-2000 K.

4.6 Rate Model Results

One surface property that must be set in rate model calculations is $[S]$, the total concentration of surface sites. In the present calculations, we assume that the total concentration of surface sites is constant and does not change with temperature or pressure. Molecular Dynamics results in Chapter 3 indicated that the total concentration of surface sites could vary with temperature and pressure, although these were carried out at pressures much higher ($P > 10^5$ Pa) than those present in reentry or experimental conditions. Changes in the total concentration of surface sites with gas-phase temperature and pressure warrant further investigation with molecular dynamics simulations. However, it is noted that atomistic simulations alone cannot be used to determine $[S]$ due to macroscopic surface roughness.

First, we consider a case with a surface site concentration of $[S] = 10^{16}$ m^{-2} and a partial pressure of atomic oxygen of $P_O = 100$ Pa and $P_{O_2} = 100$ Pa. For the purposes of finding the reverse rate coefficients we use $A_1^r = 1{\times}10^{14}$, $A_3^r = 1{\times}10^{14}$ s^{-1}. Fig. 4.12(a) shows the total recombination coefficient, γ_O, as well as the contributions of different

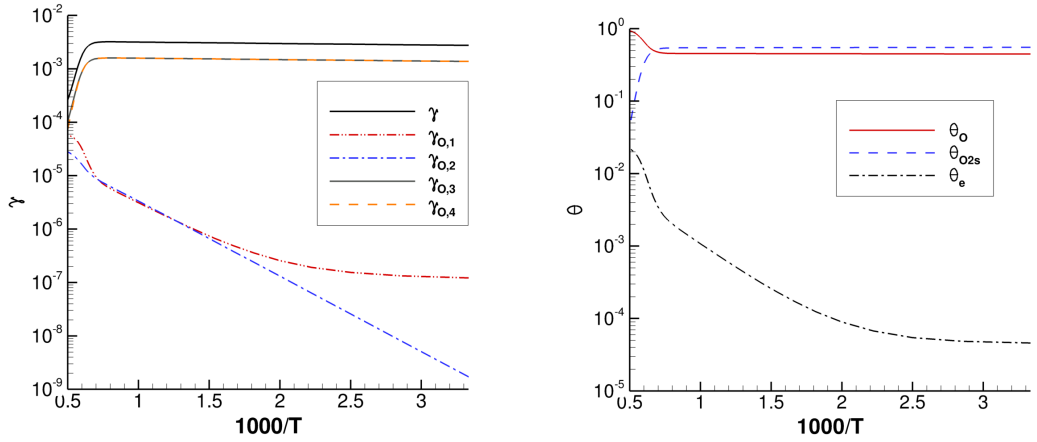

(a) γ_O vs. 1000/T

(b) Surface coverages vs. 1000/T

Figure 4.12: Rate model results with $[S] = 10^{16}$ m^{-2}, $P = 1000$ Pa, $A_1^r = 1{\times}10^{14}$, $A_3^r = 1{\times}10^{14}$ s^{-1}

reactions to γ_O. For example:

$$\gamma_{O,r1} = \frac{r_2^f - r_2^r}{[O]\bar{c}/4} \tag{4.35}$$

As shown in Fig. 4.12(a), at lower temperatures γ_O is relatively constant with temperature, while at higher temperatures γ_O decreases. The to most important reactions that contribute to the recombination coefficient are the O_2 Formation reaction and the O_2 Replacement/ER Recombination II reactions. The O_2 Replacement/ER Recombination II reaction produces molecular oxygen that leaves the surface, while the O_2 Formation reaction replenishes adsorbed molecular oxygen. These reactions have small activation energies (< 0.01 eV), which is why the recombination coefficient does not vary with temperature below 1500 K. As shown in Fig. 4.12(b), at temperatures greater than 1500 K, the surface coverage of $[O_{2s}]$ decreases, which inhibits the ER Recombination II/O_2 Replacement reaction and lowers γ_O. The decrease in $[O_{2s}]$ is a result reverse of reaction 4 in Table 4.2, the desorption of an oxygen atom from adsorbed molecular oxygen.

To evaluate how well detailed balance predicts the reverse rate constants k_r^2, k_r^4, and k_r^5, we plot the reverse rate constants vs. T in Fig. 4.13. In this plot k_r^2 and k_r^4

are normalized by $A_{\text{site}} \times \bar{c}_{O_2}/4$ so the values represent reaction probabilities. We use exponential fits of the data points in Fig. 4.13 to find the pre-exponential factors and activation energies of the rate constants. As shown in Table 4.5,the values of A_1^r, A_3^r used do not significantly affect the activation energies of the reverse reactions, which are close to the DFT values in Table 4.4. When using $A_1^r = A_3^r = 10^{14}$ s^{-1}, the pre-exponential factor for A_4^r falls outside of the acceptable range ($A_4^r = 23$), however, the probability of this reaction never exceeds unity (see Fig. 4.13). A more realistic value for A_4^r can be found by setting $A_1^r = A_3^r = 10^{15}$ s^{-1}, as shown in Table 4.5.

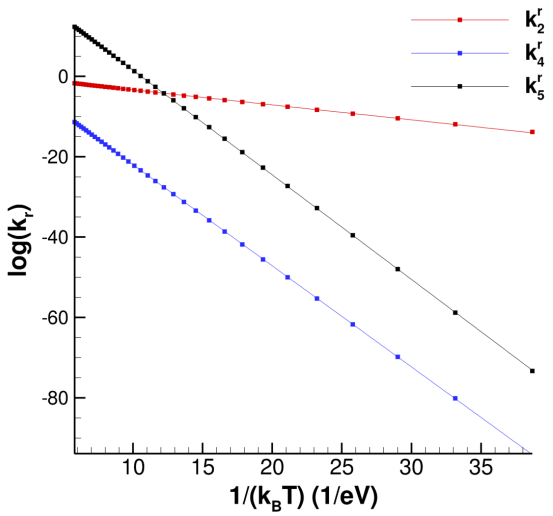

Figure 4.13: Rate constants of reverse reactions (k_r^2, k_r^4 and k_r^5) vs. T

The drop off in γ_O at high temperatures is caused by the desorption of atomic oxygen from adsorbed molecular oxygen (the reverse of reaction 4 in Table 4.2). Figure 4.14 shows the reaction rates of the highest two forward and reverse reactions as a function of temperature. The value of r_3^r substantially increases at higher temperatures, which leads to a lower concentration of O_{2s} on the surface, and the corresponding drop off in the recombination coefficient. Choosing higher values of A_3^r decreases the temperature at which this drop off occurs.

When applying detailed balance, we picked the pre-exponential factors A_1^r and A_3^r

	$A_1^r = A_3^r = 10^{14}$	$A_1^r = A_3^r = 10^{15}$
A_2^r	1.41	0.14
A_4^r	23.08	2.52
A_5^r	8.82×10^{11}	8.81×10^{13}
E_2^r (eV)	0.372	0.372
E_4^r (eV)	2.52	2.51
E_5^r (eV)	2.60	2.60

Table 4.5: Activation energies and pre-exponential factors of reverse reactions

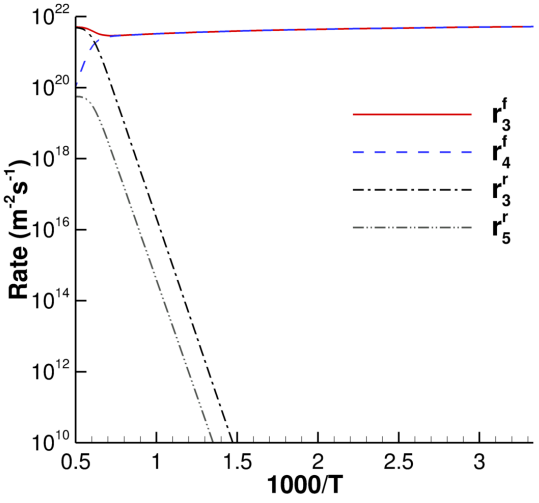

Figure 4.14: reaction rates of the highest two forward and reverse reactions vs. T

from within a reasonable range. However, we alternatively could have chosen two different reactions to achieve detailed balance. Therefore, it is important to consider the full range of reasonable parameters for the pre-exponential factors of reverse reactions to check how this could affect the predictions of the rate model. As shown in Fig. 4.14, the rate of molecular oxygen desorption (r_r^5), is the second most important reverse reaction. We will consider a case where $A_5^r = 10^{15}$ s^{-1}, and $A_3^r = 10^{13}$ s^{-1}. In this case the remaining pre-exponential factors are unaltered from the values used when

applying detailed balance above (although the rates of these reactions are so low that changing their pre-exponential factors would not alter the results of the rate model). As shown in Fig. 4.15, this increases temperature that the drop off γ_O in occurs at to ∼2700 K. Between 1500 - 2700 K, a second mechanism for oxygen recombination becomes more important. In this temperature range recombination proceeds through atomic oxygen adsorption, followed by molecular oxygen formation, followed by molecular oxygen desorption. In this case the drop off at high temperatures is due to atomic oxygen desorption (the reverse of reaction 1 in Table 4.2). With the current approach for finding the rates of the reverse reactions, the exact temperature at which γ_O begins to drop off is not known.

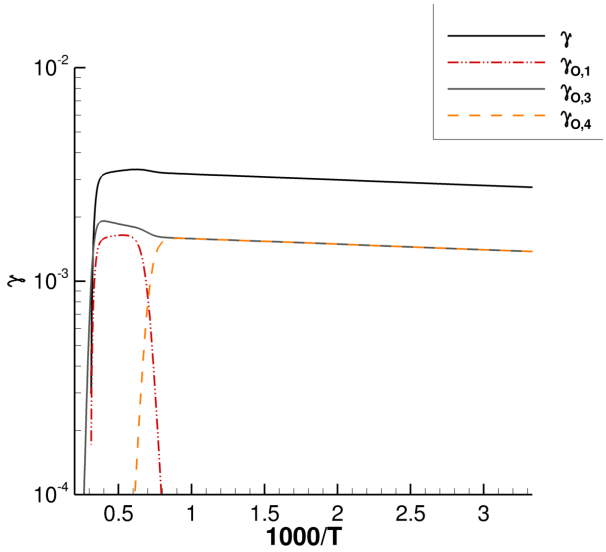

Figure 4.15: Effect of setting $A_5^r = 10^{15}\ s^{-1}$ and $A_3^r = 10^{13}\ \mathrm{s}^{-1}$

4.6.1 Effect of varying $[S]$

Here we consider the effect of varying $[S]$, the total concentration of surface sites which is an input to the rate model. Generally, we will take the approach of choosing $[S]$ to match the magnitude of experimental recombination coefficients. In this case we use pressures of $P_O = 100$ Pa, $P_{O_2} = 0$ Pa and $A_1^r = A_3^r = 10^{14}\ \mathrm{s}^{-1}$. As shown in Fig. 4.16,

varying [S] does not change the trend of γ_O vs. T, but does change the magnitude of γ_O. The surface coverages are not altered by varying [S].

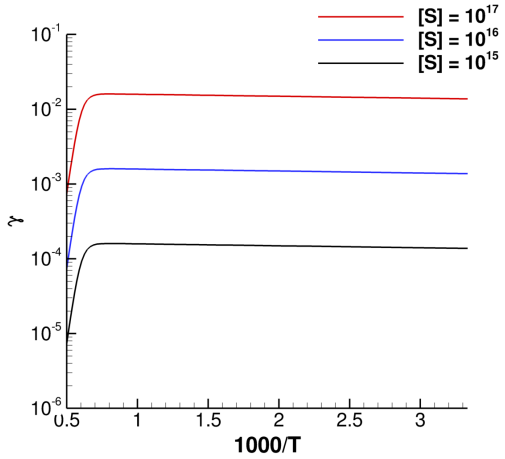

Figure 4.16: γ_O vs. 1000/T. Effect of varying [S]

4.6.2 Effect for varying partial pressures of atomic and molecular oxygen

Here we consider the effect of varying the partial pressures of atomic and molecular oxygen. In this case $A_1^r = A_3^r = 10^{14}$ s^{-1} and [S]=10^{16} m^{-2}. When varying the pressure we use $P_O = P_{O_2}$. We have found that the influence of the partial pressure of molecular oxygen (P_{O_2}) in the rate model is minimal, and that the recombination coefficient and surface coverages are not significantly altered by setting $P_{O_2} = 0$ or to any other value between 0-10,000 Pa. As shown in Fig. 4.17, increasing the total pressure shifts the location of the drop off in γ_O to higher temperatures. This is because at lower pressures, the rate of O_{2s} desorption increases relative to the rate of gas phase species colliding with surface sites. The surface coverages of O_s, O_{2s}, and E_s are given in Fig. 4.17(b-d).

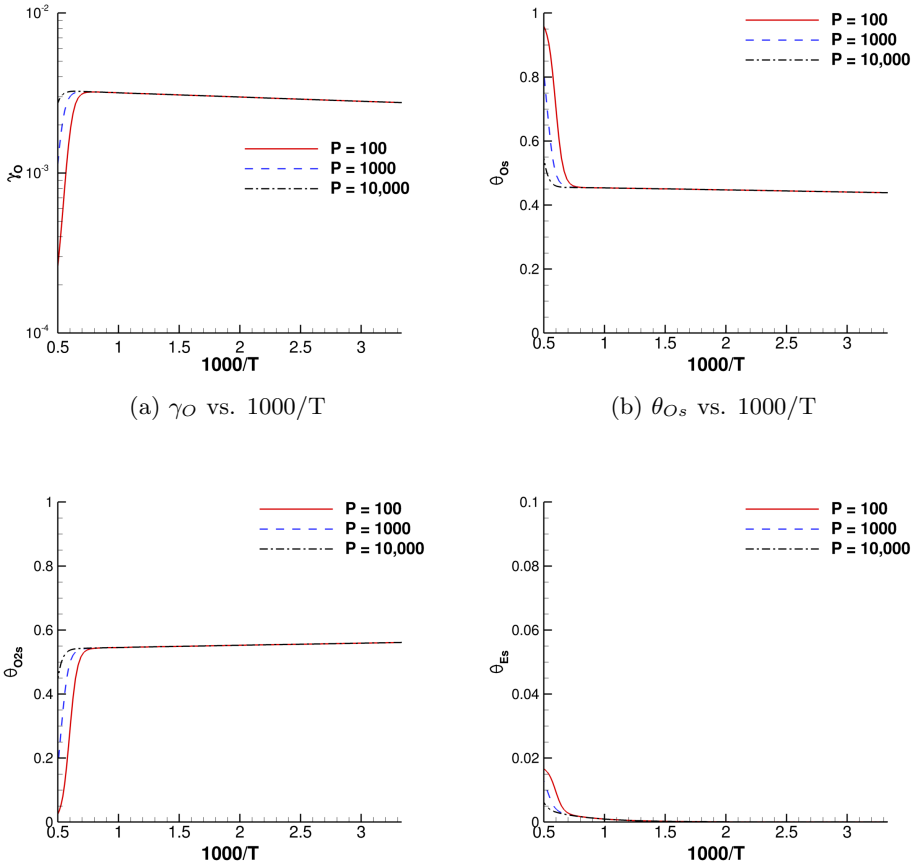

(a) γ_O vs. 1000/T

(b) θ_{Os} vs. 1000/T

(c) θ_{O2} vs. 1000/T

(d) θ_E vs. 1000/T

Figure 4.17: γ_O vs. 1000/T. Effect of varying P

4.6.3 Comparison to Experiment

Finally, we compare the predictions of the rate model to experimental results for γ_O. It is emphasized that this comparison is tentative because of the uncertainty in experimental measurements. We are primarily interested in evaluating how well the rate model predicts experimental trends in γ_O vs. T. We compare to the results of Balat et al.[5], Kim and Boudart[6], and Marshcall[7] for oxygen recombination on quartz. All of these experiments were carried out at pressures near 100 Pa, so for the rate model

we use a partial pressure of oxygen of $P_O = 100$ Pa. We choose a total surface site concentration of $[S] = 1{\times}10^{15}$ m^{-2} and use $A_1^r = A_3^r = 10^{15}$ s^{-1}. A comparison of the rate model to experimental results is shown in Fig. 4.18. The rate model is generally in agreement with experimental results at lower temperatures in that it predicts that γ_O does not vary significantly with temperature between 300-1000 K. The results of Kim and Boudart[6] indicate that γ_O begins to decrease below $\sim$250 K (this trend is also supported by the results of Macko et al.[14] for oxygen recombination on Pyrex). The rate model is not consistent with experimental trends at $T < 250$ K (although it is noted that we are primarily interested in the higher temperature regimes, which are of interest for reentry conditions). At $T > 1000$ K, we see that the experimental results predict that the oxygen recombination coefficient increases with temperature, whereas the recombination coefficient predicted by the rate model remains constant. The drop off in γ_O predicted by the rate model occurs at higher temperatures than the range provided by experimental results. There are some experimental results that predict a drop off in the recombination coefficient of oxygen on silica at higher temperatures, however these results also show γ_O increases exponentially with temperature at temperatures below the drop off.[12, 107]

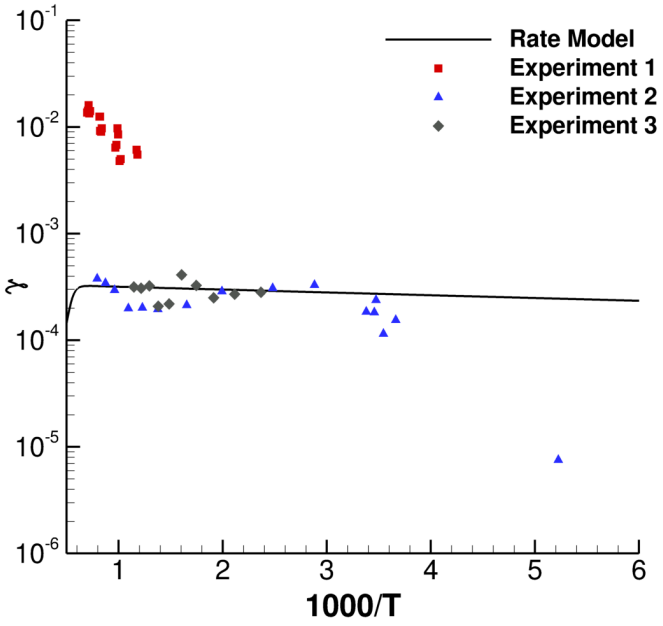

Figure 4.18: Comparison of rate model to experimental results. Experimental results from Balat et al.[5] (Experiment 1), Kim and Boudart[6] (Experiment 2), and Marshcall[7] (Experiment 3)

4.7 Conclusions

This chapter demonstrates how a catalytic rate model for oxygen recombination on silica surfaces can be created from first principles calculations. In the previous chapter we used MD simulations to model silica surfaces exposed to atomic oxygen with the goal of finding which surface structures (or defects) were potentially catalytic with respect to direct gas-phase reactions. We determined that the most common defects were the undercoordinated silicon defect, non-bridging oxygen defect, and peroxyl defect. These defects have been observed experimentally on silica surfaces under mechanical fracture and irradiation, and the structure and energetics of these defects were verified with DFT.[3, 1] In this work we created a rate model based on the reaction of gas-phase atomic and molecular oxygen with these defects using trajectory calculations with the $\text{ReaxFF}^{\text{GSI}}_{\text{SiO}}$ potential and DFT results. Trajectory calculations with the $\text{ReaxFF}^{\text{GSI}}_{\text{SiO}}$ potential were used to find the activation energies and pre-exponential factors of the forward reactions. The activation energies of reverse reactions were calculated based on DFT single point energies because the $\text{ReaxFF}^{\text{GSI}}_{\text{SiO}}$ potential did not accurately predict the energy change for all of the reactions.

The reverse reactions are difficult to model with trajectory calculations or MD simulations due to the rarity or long time scales of these reactions. To find the pre-exponential factors of reverse reactions, we used a combination of detailed balance and reasonable estimates from transition state theory. Values for the pre-exponential factors were picked from within a reasonable range for two reactions, and detailed balance was used to find the remaining reverse rate constants. We validated that the reverse constants found through this method had activation energies and pre-exponential factors within reasonable bounds. Additionally, we showed that varying the pre-exponential factors over their reasonable range did not affect trends in the recombination coefficient with temperature. Applying detailed balance is desirable because it ensures that the rate model can maintain gas-phase equilibrium between O and O_2.

The total concentration of surface sites $[S]$ is an input to the rate model. This quantity cannot be determined from atomistic calculations alone due to macroscopic surface roughness, and we set $[S]$ so that the magnitude of γ_O predicted by the rate model was in agreement with experimental results. We assumed that $[S]$ was constant,

but it is possible that in reality $[S]$ varies with temperature and pressure. We observed that $[S]$ varied with T and P in molecular dynamics simulations in Chapter 3, albeit under higher pressure conditions (P $> 10^5$ Pa) than are of interest in experiments(P $\sim$ 1000 Pa).

We found that a rate model is necessary to describe surface catalyzed recombination because a number of competing reactions contribute to the overall recombination coefficient, which varies with both temperature and gas-phase pressure. In many aerospace applications a constant value or a temperature based value of γ_O is used, which is not able to capture the complex behavior of γ_O at different temperatures and pressures.

According to our rate model, at most conditions the ER Recombination II reaction is the most important recombination reaction. This reaction is not activated, so our rate model predicts that γ_O does not vary significantly with temperature below 1500 K. At higher temperatures, our rate model predicts that γ_O significantly decreases due to desorption reactions. Our rate model agrees with the trends in experimental results at T (300-1000 K), where recombination coefficients do not vary significantly with temperature. However, there is experimental evidence that recombination coefficients increase exponentially with temperature at $T > 1000$ K, which is not predicted by our rate model. It is thought that the experimentally observed exponential trend in γ_O at $T > 1000$ K is due to an activated ER recombination reaction[6], with the trend in γ_O with T following the activation energy of the ER recombination reaction. Neither type of ER recombination reactions in our rate model confirm this hypothesis. The ER Recombination (reaction 2 in our rate model) reaction is not important because the O_2 formation reaction has the same reactants and is much more probable, while the ER Recombination II reaction (reaction 4 in our rate model) is essentially non-activated. Therefore, we conclude that the exponential trend in recombination coefficient at $T >$ 1000 K is not due to an activated ER recombination type reaction.

It is possible that other recombination mechanisms, such as Langmuir-Hinschelwood (LH) recombination contribute to recombination. It is thought that LH recombination between physisorbed oxygen atoms and chemisorbed oxygen atoms results in the slight maximum in recombination coefficients at low temperatures ($T \sim 300$ K).[6, 14, 37] However our rate model already predicts a relatively constant γ_O at low temperatures, so including this mechanism would not significantly alter the trends in γ_O vs. T. At higher

temperatures, it is possible that LH recombination between chemisorbed oxygen atoms can take place. For example, in an earlier work we observed that non-bridging oxygen atoms could diffuse through the surface via lattice diffusion.[108] There is experimental evidence that lattice diffusion of atomic oxygen occurs through bulk SiO_2[109], and there are computational works modeling this process.[110, 111] In our previous work we found that diffusing non-bridging oxygen atoms could combine on the surface to form adsorbed O_2, which could eventually desorb to complete the recombination process.[108] Further investigation of the diffusion and LH recombination of non-bridging oxygen atoms on silica surfaces with both molecular dynamics simulations and DFT is warranted.

Chapter 5

Classical Trajectory Calculation Direct Simulation Monte Carlo

5.1 Introduction

In a dilute gas the average time between molecular collisions (the mean collision time τ) can be orders of magnitude larger than the time required for a collision event itself. From kinetic theory, τ scales as $\frac{1}{\rho\sqrt{T}}$ where ρ and T are the gas density and temperature. For low density gases typical of high-altitude flight ($\rho \approx 10^{-4}\ kg/m^3$), τ is of the order of microseconds ($10^{-6}\ s$). From a molecular simulation standpoint, this introduces disparate simulation time scales as the integration of atomic trajectories during a collision event requires time steps on the order of femtoseconds ($10^{-15}\ s$). Despite this, Molecular Dynamics (MD) simulation of select flow features (such as one-dimensional normal shock waves or expansions), in which the complete system of atoms is integrated with femtosecond scale time steps, is now possible with moderate parallel computer resources.[98, 112, 113] Furthermore, such MD simulations can be greatly accelerated by adopting a combined Event-Driven/Time-Driven (EDTD) MD algorithm[114] where molecules are advanced directly to their next collision and each collision is integrated using standard Time-Driven MD. In this case the simulation evolves at a time scale approaching τ while exactly reproducing the corresponding pure MD solution. For both pure MD and EDTD-MD methods the only required input is a model for atomic interactions, often specified by a set of potential energy surfaces (PES) developed for

the collisions of interest, and the paths of molecules through the simulated domain are deterministic.

Because changes in the state of a dilute gas occur via molecular collisions, the relevant spatial scale is the mean free path (λ). Below this spatial scale ($O(\lambda)$) no changes in the gas state are possible, and likewise no changes are possible below a time scale of $O(\tau)$. In a dilute gas there are an enormous number of atoms within a volume of λ^3, ranging from tens-of-thousands at sea level to billions at an altitude of 50 km. Therefore, full MD or EDTD-MD simulations of three dimensional flows, which involve many many mean free paths, are not feasible with existing computational resources. However, to describe the non-equilibrium state of a dilute gas it is unnecessary to account for the properties of all real atoms, rather, their local distribution functions (for velocity, internal energy, chemical species, etc.) are sufficient. Such distribution functions can be accurately constructed by considering only a small fraction of the real molecules. The direct simulation Monte Carlo (DSMC) method[16] takes advantage of these inherent properties of dilute gases by operating with time steps and cell sizes on the order of τ and λ, respectively, and by using simulator particles which represent a large number of real molecules. However, the DSMC method goes one step further and also uses probabilistic rules to determine the local collision rate and collision outcomes, thus introducing a collision *model*. Most DSMC collision models are phenomenological in that they are formulated to be consistent with macroscopic constitutive laws or rate models, and are parametrized with experimental data (often obtained near thermal equilibrium and at low temperatures). For example, the popular Variable Hard Sphere (VHS) model contains two parameters which are used to match an experimentally measured reference viscosity and the local dependence of viscosity on temperature.[16]

For complex flows involving rotational, vibrational, and chemical non-equilibrium at high temperatures (characteristic of hypersonic shock layers), recent research has investigated the use of accurate *ab initio* based PES to inform DSMC collision models. It has been shown that trajectory calculations using sufficiently accurate PES have the ability to reproduce molecular beam experimental results for both collision cross-sections and product energy distributions (for example, see review in Ch. 9 of Steinfeld, Francisco and Hase[21]). In general, a large number of individual trajectory calculations can be

performed and used to generate a state resolved collision model, which maps the probability of two colliding molecules with given translational, rotational, and vibrational energies transitioning to new energy states. This approach was taken by Kim and Boyd to create a state resolved model to describe energy transfer and chemical reactions in H_2-H_2[18] and N-N_2 collisions[17, 18] based on the results of Quasi-Classical Trajectory (QCT) collisions carried out on *ab initio* based potential energy surfaces.[19, 20] Although highly desirable, compiling databases of state-to-state cross-sections and implementation in a state resolved flow solver is not a trivial process and often involves a number of further modeling steps, such as the grouping of ro-vibrational states and enforcing microscopic reversibility to maintain detailed balance and the equipartition of energy.

An alternate approach, and the focus of this chapter, is to perform trajectories of individual collisions on-the-fly during a DSMC simulation. Because the equations of motion for molecular collisions are inherently time reversible, this approach naturally satisfies microscopic reversibility which leads to detailed balance and equipartition of energy under equilibrium conditions. However, the high computational cost of calculating trajectories during a simulation has been one significant barrier to the widespread application of this method.[23] There are only a few publications that have addressed this approach, referred to as either Classical Trajectory Calculation (CTC-DSMC) or Quasi-Classical Trajectory Calculation (QCT-DSMC). In one series of publications, Koura combined null-collision DSMC with CTC to simulate translational and rotational non-equilibrium in nitrogen shock waves and a spherical expansion, including comparison with experimental data.[22, 115, 116] Koura also extended the same method to simulate dissociation of oxygen in an argon heat bath.[117] In another series of conference publications, Fujita *et al.* combined the no-time-counter (NTC) DSMC method, using the VHS collision model, with QCT to first study rotational/vibrational excitation and dissociation of nitrogen[118, 119] and later the dissociation of carbon monoxide through collisions with atomic oxygen.[120] However, combining a collision rate dictated by a phenomenological model such as VHS with QCT analysis for reaction cross-sections can lead to unphysical reaction probabilities, especially when the VHS model is extrapolated and used at high temperatures.[121] It is desirable for CTC-DSMC and QCT-DSMC simulations to be dependent only on the specification of a PES and not on any other

phenomenological collision model.

A number of topics important in CTC-DSMC calculations are discussed in this chapter. First, we outline a CTC-DSMC implementation that uses the NTC scheme with a cross-section that is determined by the PES and is consistently applied as the maximum impact parameter for the trajectory calculations. Results for translational and rotational relaxation within 1D normal shock waves are directly compared with pure MD simulations[98, 113], where both CTC-DSMC and MD simulations employ the same PES. Through such comparison, any discrepancies between stochastic approach of DSMC and deterministic approach of MD (where the trajectory of every individual atom in a flow is calculated) can be precisely studied. Second, we present a preliminary algorithm for determining the three body collision rate in CTC-DSMC simulations. This algorithm is validated with MD simulations for the simple case of constant cross-section molecules with no interatomic potential. An accurate description of three body collisions is essential to describing gas phase recombination reactions, which play an important role in the non-equilibrium chemistry in the shock layer of reentry vehicles. Third, we present a hybrid CPU/GPU parallelization technique for CTC-DSMC simulations involving only two body collisions. The high computational cost of calculating trajectories during a simulation has been one significant barrier to the widespread application of this method. [23] GPU acceleration has previously been successfully applied to full molecular dynamics simulations[122, 57] and to numerical solutions of the Boltzmann Transport Equation[123], however, the present work is the first to apply GPU acceleration to the CTC-DSMC method. The parallelization strategy presented here is straight-forward and has the potential to scale to large CPU/GPU clusters, which would enable the application of CTC-DSMC to 2D and 3D flows with complex geometries. Finally, we discuss some of the issues that arise when using CTC-DSMC simulations to model rotating, vibrating molecules. At lower temperatures ($T < \theta_v$), there are differences in the average energy in the vibrational mode based on classical and quantum descriptions of the gas. This causes issues for the jump conditions in 1D shocks, because a shock composed of classically vibrating molecules cannot be forced to take boundary conditions based on a gas with a quantum mechanical description of vibration. A modification to the quantum boundary conditions which allows upstream

and downstream flow variables close to the exact values is presented. At higher temperatures, rovibrational effects must be accounted for to correctly define rotational and vibrational temperature.

This chapter is organized as follows: In section 5.2 we outline our CTC-DSMC implementation. In section 5.3 we present an algorithm for determining the three body collision rate. Section 5.4 shows detailed comparisons of Molecular Dynamics simulations to CTC-DSMC simulations for 1-D shocks. In section 5.5 we present our CPU/GPU parallelization scheme. Section 5.6 discusses simulating vibration in CTC-DSMC simulations, and in section 5.7 we present our conclusions.

5.2 The CTC-DSMC method

5.2.1 Collision Cross-section

In CTC-DSMC calculations, the collision cross-section is used to determine the number of trajectory calculations performed per cell, per DSMC time step, and also used to set the maximum impact parameter for the trajectories. It is emphasized that the cross-section used in CTC-DSMC simulations (hereafter referred to as σ_{CTC}) is dissimilar to the total collision cross-section (σ_T), which is calculated by integrating the differential cross-section over all possible scattering angles as shown by Vincenti and Kruger.[103] As described below, the cross-section σ_{CTC} should be dictated by a conservative value of the maximum impact parameter beyond which the energy transfer between colliding particles is known to be negligible. From the perspective of the NTC collision algorithm[16], the cross-section is used identically to the total cross-section when calculating the collision probability (P_{col}) between two particles:

$$P_{col} = \frac{\sigma_T |\vec{g}|}{(\sigma_T |\vec{g}|)_{max}} \tag{5.1}$$

where $\vec{g}$ is the relative velocity between molecules and $(\sigma_T |\vec{g}|)_{max}$ is a cell based maximum of the cross-section and relative velocity.

There is some inconsistency in the literature about how the collision cross-section should be determined in CTC-DSMC simulations. In one series of works the authors use the VHS collision cross-section[118, 119, 120], while in another series of works the authors uses a cross-section dictated by the potential energy surface.[22, 115, 117] Clearly,

it is desirable to use the approach that is based only on the potential energy surface and not the VHS model, which relies on experimental data for parametrization. Additionally, when extrapolated to high temperatures and combined with CTC calculations, it has been shown that unphysical reaction probabilities can result from using the VHS based cross-section.[121] To define the collision cross-section for trajectory calculations based on the interatomic potential, an approach similar to that of typical MD simulation is used: at long distances the force between atoms decreases significantly and the exchange of energy between molecules becomes negligible. This can be implemented through the two approaches described below.

In the first approach, called the constant cross-section approach, particles have a constant cross-section with a diameter corresponding to a fixed interatomic potential cutoff (D_{Cutoff}). The collision cross-section is then:

$$\sigma_{CTC} = \pi D_{Cutoff}^2 \tag{5.2}$$

When two particles are selected to collide, trajectory calculations are carried out as follows:

1. The DSMC simulation generates a collision pair with a relative velocity $\vec{g}$ and rotational energies $e_{rot,1}$, $e_{rot,2}$ (if particles are molecules). This data is sent to a collision subroutine that calculates the outcome of the collision.

2. Particle A is placed at the origin, and particle B is placed at a distance D_{Cutoff} from particle A on the x-axis. Particle B is displaced by an impact parameter b = D_{Cutoff}*$(R_f)^{\frac{1}{2}}$ at a random angle $\theta = 2\pi R_f$ on the y-z plane (R_f is a random number between zero and one). The particles are given a relative speed of $|\vec{g}|$ along the x-axis.

3. Particle B is rotated about the origin so the relative velocity vector is aligned with $\vec{g}$.

4. If particles are molecules, the particles are assigned rotational energies $e_{rot,1}$ and $e_{rot,2}$. Each molecule is given a random initial orientation and direction of angular momentum.

5. The collision is integrated until particles are at a distance greater than D_{Cutoff} apart.

6. The atomic velocities are transformed back to the collision relative velocity ($\vec{g}$) and rotational energies ($e_{rot,1}$, $e_{rot,2}$) if the particles are molecules. The collision is complete and these quantities are updated for the DSMC collision pair.

We have found that an interatomic potential cutoff $D_{Cutoff} = 4\sigma_{LJ}$ is sufficient for CTC-DSMC simulations of argon and diatomic nitrogen and that larger values of D_{Cutoff} did not affect the results of simulations. Thus as long as the cross-section used to select the number of trajectories is conservative, then it is the interatomic potential that determines the collision rate (collisions resulting in a finite scattering angle χ). A diagram illustrating the impact factor (b), interatomic potential cutoff (D_{Cutoff}) and scattering angle χ is shown in Fig. 5.1.

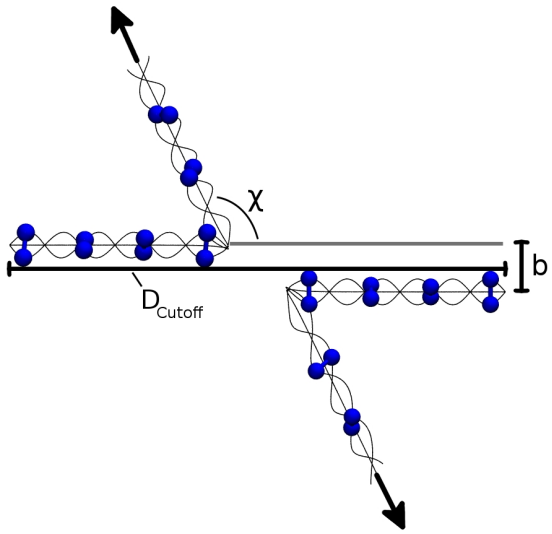

Figure 5.1: Diagram illustrating collision parameters: Impact parameter (b), scattering angle (χ), and interatomic potential cutoff (D_{Cutoff})

In the second approach, called the variable cross-section approach, the cross-section of colliding particles is a function of their relative velocity. This approach was originally outlined in the work by Matsumoto and Koura.[124] The cross-section of particles is set based on the maximum impact factor (b_{max}) that gives a scattering angle χ_{Cutoff} at some relative speed $|\vec{g}|$. The scattering angle χ_{Cutoff} is set to a small value (for example 1° or 0.1°), thereby disregarding all collisions that will result in a scattering angle less than this value. For both argon and diatomic nitrogen collisions we have found that a value of $\chi_{Cutoff} = 1°$ is conservative, and that reducing this value does not affect the results of CTC-DSMC simulations. The collision cross-section is then given by:

$$\sigma_{CTC} = \pi(b_{max}(|\vec{g}|))^2 \tag{5.3}$$

and the following formula is used to set the interatomic potential cutoff:

$$D_{Cutoff} = \max(4\sigma_{LJ}, 1.5b_{max}(|\vec{g}|)) \tag{5.4}$$

This expression for D_{Cutoff} ensures that the interatomic potential cutoff is sufficiently large enough to maintain adequate energy conservation at low values of b_{max}, and that at larger values of b_{max} the interatomic potential cutoff is large enough to capture the full range of scattering. We have found that the factors of 4 and 1.5 in the above expression are sufficiently conservative for both argon and diatomic nitrogen collisions, and that increasing these parameters did not affect the results of CTC-DSMC simulations. Trajectory calculations using the variable cross-section method are carried out in a similar manner as described above for the constant cross-section approach, with the exception that in step 2 particle B is initialized with an impact factor between zero and b_{max} at a distance D_{Cutoff} away from particle A.

Figure 5.2 shows a contour plot of the absolute value of the scattering angle ($|\chi|$) for argon-argon collisions with respect to the non-dimensional translational collision energy ($\epsilon^* = \frac{e_{trans}}{\epsilon_{LJ}}$) and non-dimensional impact factor ($b^* = \frac{b}{\sigma_{LJ}}$). A description of trajectory calculations for argon-argon collisions is given in section 5.4. The translational collision energy (e_{trans}) is a function of the relative velocity of the molecules:

$$e_{trans} = \frac{1}{2}\mu|\vec{g}|^2 \tag{5.5}$$

where μ is the reduced mass. The maximum impact factors (b_{max}) for the variable and constant cross-section approaches are also shown in Fig. 5.2, where it is clearly seen that

all collisions resulting in significant scattering occur at smaller impact factors than these conservative maxima. For the variable cross-section approach, the value of b_{max} shown in Fig. 5.2 lies precisely along the $|\chi| = 1°$ contour. In this case the $|\chi| = 1°$ contour is well fit with a power law $b_{max} = A|\vec{g}|^B$ ($A = 69.0$, $B =$ -0.333), although in principle any functional form may be used for this fit. For N_2-N_2 collisions a similar fit gives $A = 58$ and $B =$ -0.333, where the maximum scattering angle of many collisions with a random rotational energy at a given impact factor and collision energy are considered. We have found that both approaches produce identical results in CTC-DSMC simulations as long as the criteria for the collision cross-section are sufficiently conservative. The variable cross-section approach is faster than the constant cross-section approach because it reduces the number of collisions with almost no scattering (by roughly a factor of 2 for the shocks considered below), while allowing a higher DSMC time step due to the decreasing nature of the cross-section at higher collision speeds. For the CTC-DSMC simulations presented in this work, we used the variable cross-section approach.

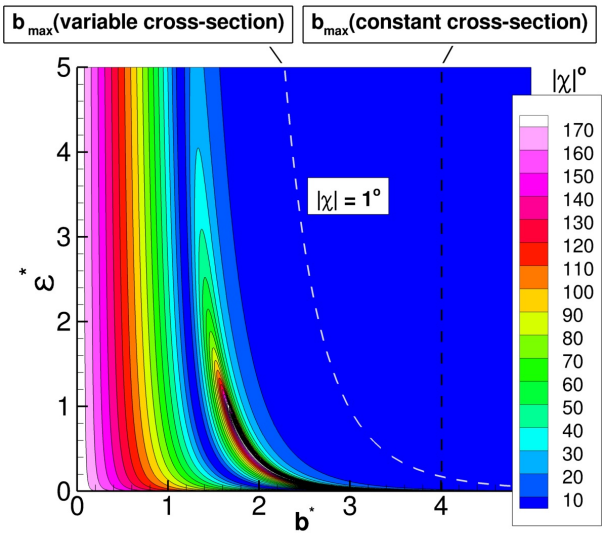

Figure 5.2: Contour plot of scattering angle $|\chi|$ vs. non-dimensional impact parameter b^* and collision energy ϵ^*. Maximum impact factors (b_{max}) for the variable cross-section (white dashes) and constant cross-section (black dashes) approaches.

5.3 Three body collisions in CTC-DSMC

5.3.1 Long Lived Two Body Collisions

One important phenomenon not previously considered in CTC-DSMC simulations is long lived two body collisions. Although classically two bodies can never form a bond without a third body to adsorb some of the collisional kinetic energy, it is still possible to have long lived two body collisions in quasi-orbiting metastable states. We have found that these collisions are likely to occur in low energy N_2-N_2 collisions. A description of trajectory calculations for nitrogen-nitrogen collisions is given in section 5.4. For example, in a typical long lived N_2-N_2 collision the translational energy of two colliding molecules is partially converted to rotational energy, reducing the translational energy below the value needed to escape the potential well. The two molecules exist in this metastable state until the complex exchange between rotational and translational energy allows the molecules to gain enough translational energy to escape the potential well. Collisions between argon atoms do not typically enter long lived states because they lack a rotational energy mode. An example of such a long lived collision between two nitrogen molecules is shown in Fig. 5.3(a). From a quantum perspective, long lived two body collisions can also occur in the form of metastable resonance states due to the effective rotational potential of colliding molecules.[125]

Figure 5.3(b) shows a plot of the average collision length (τ_{avg}) vs. temperature for N_2-N_2 collisions. This figure also shows the temperature dependence of $\tau_{99\%}$, which is defined as the maximum time taken for 99% of collisions at a given temperature (1% of collisions take longer than $\tau_{99\%}$). The relative velocity of collisions was set based on the average relative velocity of colliding nitrogen molecules in a hard sphere gas ($|\vec{g}| = \sqrt{(9\pi k_B T)/(8m_N)}$), and the rotational energy of colliding molecules was sampled from the classical rotational energy distribution function ($e_{rot} = -k_B T \times \ln(R_f)$).[16] At lower temperatures both τ_{avg} and the gap between τ_{avg} and $\tau_{99\%}$ significantly increase. Thus, it is important to consider $\tau_{99\%}$ to fully describe the length of the majority of long lived collisions at a given temperature. Long lived two body collisions are important in the context of DSMC simulations because in some cases these collisions can take longer than the DSMC timestep. Such physics, captured naturally by MD, are not explicitly modeled by either the DSMC or CTC-DSMC methods. For example, these still-colliding

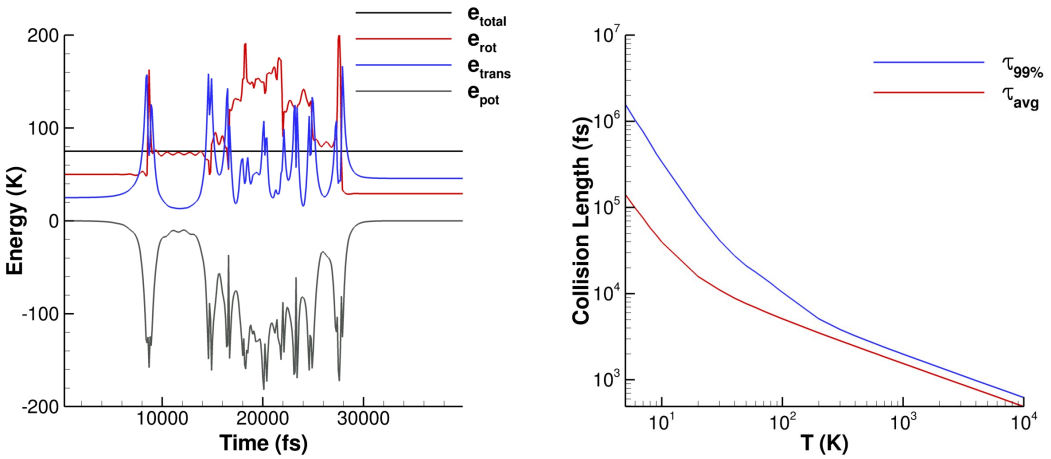

(a) Total translational energy (e_{trans}), rotational energy (e_{rot}), potential energy (e_{pot}), and total energy ($e_{tot} = e_{trans} + e_{rot} + e_{pot}$) during a long lived N_2-N_2 collision.

(b) τ_{avg} and $\tau_{99\%}$ vs. temperature for N_2-N_2 collisions.

Figure 5.3: Long lived N_2-N_2 collisions.

particles should not be considered as separate particles in the next DSMC timestep, but rather as pseudo-particles that can in turn collide with other molecules.

In this work we set a trajectory time cutoff equal to the DSMC timestep. If a collision is not complete after being integrated for this maximum trajectory time cutoff, the collision is discarded and the post-collision rotational and translation velocities are not updated. For the cases studied here, this does not have a significant influence on the results. For example, in the $M_1 = 7$, $T_1 = 28.3$ K, $\rho_1 = 0.1$ kg/m^3 (the subscript 1 designates the upstream shock conditions) diatomic nitrogen shock described in the subsequent section, only 0.25% of collisions (primarily in the cold upstream region of the shock) are cut off due to the maximum trajectory time. Because this is only a small fraction of the total number of collisions, it is not expected to significantly influence the results of the shock. We also tried using a trajectory time cutoff of $2\times$ or $4\times$ the DSMC timestep and confirmed that the results were not affected.

5.3.2 Three Body Collisions

One important topic not previously considered in CTC-DSMC simulations is three body collisions. Several works have addressed the phenomenon of three body collisions in DSMC simulations[126, 127, 128, 129] In this work, we take an approach similar to that outlined by Bird.[126], where the three body collision rate is calculated by considering the collision of two body collisions (called pseudo-particles) with other gas phase molecules. Moreover, two body collisions taking any length of time (and especially those long-lived two body collisions) have a finite probability of colliding with a third molecule during a DSMC timestep. Such physics, naturally captured by MD, are not explicitly modeled by either the DSMC or CTC-DSMC methods without additional considerations. One of the difficulties associated with implementing three body collisions in a DSMC code is a description of the life-time and collision cross-section of pseudo-particles, which are ill-defined for typical DSMC collision models.[129] In CTC-DSMC simulations we can readily calculate both of these values, enabling an unambiguous description of the three body collision rate (Z_{3B}). Additionally, the results of CTC-DSMC simulations can be compared to MD simulations with an identical interatomic potential, ensuring a rigorous validation of the three body collision algorithm.

In this work, we consider the simple case of constant cross-section molecules with no interatomic potential (although molecules collide, their velocities are not altered by collisions) with a diameter D_{Cutoff}. The three body collision rate for identical particles interacting with *any* interatomic potential at a temperature T is:

$$Z_{3B} = n_{2B} n_A (\pi d_{3B}^2) \left(\frac{8 k_B T}{\pi \mu_{2B,A}} \right)^{1/2} \tag{5.6}$$

Where n_{2B} is the number density of two body collisions, n_A is the number density of molecules, $\pi \mathrm{d}_{3B}^2$ is the average cross section of two body collisions with other molecules, and $\mu_{2B,A}$ is the reduced mass of a two body collision and another molecule. The concentration of two body collisions, n_{2B}, is defined as:

$$n_{2B} = Z_{AA} \times \overline{\tau}_{2B} \tag{5.7}$$

Where Z_{AA} is the collision rate per unit volume for species A:

$$Z_{AA} = \frac{n_A^2}{2} (\pi D_{Cutoff}^2) \left(\frac{8 k_B T}{\pi \mu_{A,A}} \right)^{1/2} \tag{5.8}$$

and $\overline{\tau}_{2B}$ is the average life time of a two body collision. The quantity $\overline{\tau}_{2B}$ is given by the average distance traveled by an individual atom in the center of mass frame during a collision ($\overline{d}$) divided by average relative speed in during the collision ($\overline{g_c}$):

$$\overline{\tau}_{2B} = \frac{\overline{d}}{\overline{g_c}} \tag{5.9}$$

For the case of constant cross-section particles with zero interatomic potential, there is an analytic expression for $\overline{\tau}_{2B}$. The quantity $\overline{d}$ is the average height of a sphere of radius D_{Cutoff} integrated over a central disk:

$$\overline{d} = \frac{1}{\pi D_{cutoff}^2} \times 2 \int_0^{2\pi} \int_0^{D_{cutoff}} (D_{cutoff}^2 - r^2)^{1/2} r dr d\theta = \frac{4}{3} D_{cutoff} \tag{5.10}$$

and the inverse average relative velocity of colliding hard sphere particles, $1/\overline{g}_c$ is:

$$\overline{g}_c^{-1} = \left(\frac{8 k_B T}{\pi m_A / 2} \right)^{-1/2} \tag{5.11}$$

Even for the simple case of molecules with no interatomic potential d_{3B} must be determined from the three body collision rate found from MD or CTC-DSMC calculations. However, value of d_{3B} must lie between D_{Cutoff} and $\frac{3}{2} D_{Cutoff}$, which gives bounding values of Z_{3B} for constant cross-section collisions with no interatomic potential. From the results of CTC-DSMC and MD simulations shown below, $\mathrm{d}_{3B} \approx 1.26\ D_{Cutoff}$.

5.3.3 CTC-DSMC Three Body Collision Algorithm

To implement three body collisions in CTC-DSMC, we use the algorithm below, which is based on the NTC algorithm. To account for the life-time of a two body collision, the probability of a collision between a pseudo-particle and another molecule is multiplied by the fraction of a DSMC time step over which a two body collision exists.

1. Execute the standard two body NTC collision algorithm with classical trajectory collisions.

   (a) Save each two body collision in a list `list_2B`. Each two body collision has a time (`tau_2B`) and center of mass velocity (`v_com[3]`) associated with it. Additionally, save the two molecules that participate in the collision in a list

list_1B. Each of these molecules is saved with the time not colliding during a DSMC time step (tau_1B = delta_t_DSMC - tau_2B) and the molecule's velocity (v[3]).

(b) Save all non-colliding molecules in the list list_1B, each with the time tau_1B = delta_t_DSMC and the molecule's velocity (v[3]).

2. Randomize the positions of molecules within the lists: list_1B, list_2B

3. Find a maximum number of expected collision pairs:
   double max_pairs = sigma_g_max3B × list_2B_size × average_list_1B_size × wp × delta_t_DSMC / cell_volume
   int int_max_pairs = floor(max_pairs) + 1
   double corr_factor = int_max_pairs/max_pairs
   where sigma_g_max3B is a cell based maximum of the cross-section and relative velocity for three body collisions, average_list_1B_size is the average number of particles in the cell, and wp is the molecule weight.

4. For each item i in list_2B[] up to max_pairs:

   (a) To prevent a two body collision from colliding with one of its constituent bodies: If the molecule at list_1B[i] is a participant in the two body collision, swap it with list_1B[i+1]. If the new particle at list_1B[i] is also a participant in the two body collision, swap this particle with list_1B[i+2].

   (b) Get the collision cross-section for the two particles:
   g_3B[] = list_2B[i].v_com[] -list_1B[i].v[]
   sigma_g_3B = get_sigma(list_2B[i], list_1B[i])^1 × |g_3B[]|

   (c) Find the pair collision probability:
   time_frac = (list_2B[i].tau_2B × list_1B[i].tau_1B)/ (delta_t_DSMC^2)
   P_collide = corr_factor × sigma_g_3B × time_frac / sigma_g_max3B

   (d) Collide Particles:
   if(R_F < P_collide) then collide_particle_3B(list_2B[i], list_1B[i])
   In the CTC collision, the the two-body collision is first integrated for a time $R_F \times \tau_{2B}$, and the third body is added at a random point on the leading face of the two body collision.

[1] This subroutine is described in Appendix A

To find the three body collision rate for constant cross-section particles with no interatomic potential, we conducted 0D adiabatic CTC-DSMC simulations in a periodic box at range of temperatures (7500 - 12500 K) and number densities (7.5×10^{23} - 2.25×10^{24}). We also carried out MD simulations for identical systems with LAMMPS.[57] For all cases we used a molecular diameter of D_{cutoff} = 10 Å, and domain with 500,000 molecules. The CTC-DSMC three body collision rate as a function of temperature and number density is shown in Figs 5.4(a,b). The trends in temperature and density of the CTC-DSMC collision rate are mirrored by the bounding analytic expressions given in Eqs. 5.6-5.11. Figure 5.4 also shows the predictions of MD simulations for the three body collision rate, which are in exact agreement with CTC-DSMC results.

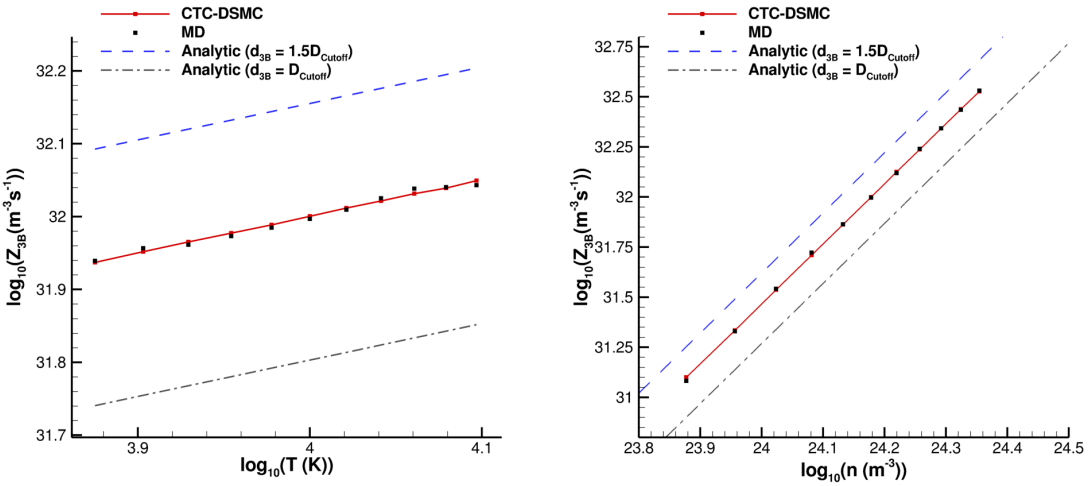

(a) Z_{3B} vs. T, n = 1.51×10^{24}(m^{-3})

(b) Z_{3B} vs. n, T = 10,000 K

Figure 5.4: Comparison of Z_{3B} as predicted by CTC-DSMC, MD, and a bounding analytic expression

To extend this algorithm to three body collisions with non-zero interatomic potentials, a number of additional factors must be considered. Specifically, a two body collision can collide with any other body in a cell during a DSMC timestep. If a two

body collision collides with a molecule that has been selected to participate in a separate two body collision during a DSMC timestep, this raises concerns about which collision should actually occur (this does not affect particles with no interatomic potential, because collisions do not alter molecular velocities). One approach might be to assign each two body collision a random time within the DSMC timestep, and use this to determine which collision occurs first, discarding the collision that occurs at a later time. Another concern is the phenomenon of long-lived two body collisions. For particles with no interatomic potential, the length of a collision is relatively short (typically < 1 ps), however, for collisions with an interatomic potential the collision length can exceed the DSMC timestep. For example, we observed that this occurred for a small fraction (0.25%) of N_2-N_2 collisions in the 1D shock discussed in the next section. For the purposes of calculating three body collisions, these long-lived two body collisions could be extended over multiple timesteps and decay back into two particles when the collision is finished. Ultimately, any additions to the above algorithm that are made to account for these phenomena can be thoroughly evaluated with MD simulations using the same interatomic potential. The case of non-interacting particles gives a reasonable approximation of the three body collision rate for atoms interacting with the LJ potential. We found that the three body collision rate for atoms interacting with the Ar-Ar LJ potential as predicted by MD simulations was within a few percent of the value predicted by non-interacting particles.

5.4 Comparison of CTC-DSMC to MD

In this section we compare the results of CTC-DSMC simulations of 1D shocks composed of Ar and N_2 to molecular dynamics simulations of the same systems carried out by Valentini et al.[98, 113] For both cases we use the same interatomic potential as MD calculations, enabling a consistent comparison of the two numerical methods.

5.4.1 Trajectory Calculations

The collision integration scheme in CTC-DSMC simulations should be chosen such that it accurately describes the collision phenomenon of interest. In this section we consider cases where a purely classical treatment of collisions is appropriate: Ar-Ar collisions and

N_2-N_2 collisions at low temperatures where the vibrational motion can be neglected. For more complex cases involving vibrationally excited molecules or chemical reactions, more advanced techniques, such as the quasi-classical and semi-classical methods[130, 131], are necessary. To integrate trajectories we use the same integration method used in MD simulations: the Velocity-Verlet algorithm.[132] Trajectories are integrated with a time step of $\Delta t = 1$ fs, which maintains sufficient energy conservation in both N_2-N_2 and Ar-Ar collisions (this time step is identical to that used in MD simulations[98, 113]). For example, the average relative error in the total kinetic energy of colliding molecules:

$$E_{rel} = \left| \frac{e_{tot,i} - e_{tot,f}}{e_{tot,i}} \right| \tag{5.12}$$

(where e_{tot} is the total kinetic energy, the subscripts i and f denote pre and post collision) is $E_{rel} = 9.6\times10^{-7}$ in a uniform 300 K nitrogen flow as simulated by CTC-DSMC. For N_2-N_2 collisions we use the RATTLE algorithm to maintain fixed bond length[133], as energy transfer into vibrational modes is negligible at the temperatures considered.

Another essential ingredient in accurately predicting the outcomes of collisions is the potential energy surface. For argon-argon collisions we use the Lennard-Jones (LJ) potential, and for N_2-N_2 collisions we use a site-to-site LJ potential, both of which are identical to the potentials used in the MD simulations.[98, 113] The functional form of the LJ potential is given by:

$$V(r_{ij}) = 4\epsilon_{LJ}\left[\left(\frac{\sigma_{LJ}}{r_{ij}}\right)^{12} - \left(\frac{\sigma_{LJ}}{r_{ij}}\right)^{6}\right] \tag{5.13}$$

where r_{ij} is the distance between atoms. The LJ parameters used for nitrogen and argon are given in Table 5.1. Although the LJ potential is too simplistic to describe more complex collisions, for the flow conditions considered here it is sufficiently accurate, as MD simulations using these potentials were found to be in good agreement with available experimental results.[98, 113] We also tried the *ab initio* Ar-Ar potential developed by Patkowski and Szalewicz[134], and found no significant differences in the results of CTC-DSMC simulations for 1-D Argon shocks.

Element	σ_{LJ} (Å)	ϵ_{LJ} (K)
Argon	3.42	119.18
Nitrogen	3.17	47.22

Table 5.1: LJ Potential parameters for Argon and Nitrogen.

5.4.2 Argon Shock

A comparison between CTC-DSMC and MD was performed for a $M_1 = 5$, $T_1 = 300$ K, $\rho_1 = 1.0$ kg/m^3 shock. The downstream boundary conditions were found using the Rankine-Hugoniot jump conditions. The one-dimensional CTC-DSMC simulation domain consisted of 600 cells ($\sim 70\lambda_1$) with a uniform length of 10 nm ($\sim \lambda_1/9$), and boundary conditions were imposed by 10 buffer cells on the ends of the domain that were refreshed at every DSMC timestep. The upstream mean free path λ_1 is estimated using:

$$\lambda_1 = \frac{1}{\sqrt{2} n \pi d_{ref}^2} \left(\frac{T}{T_{ref}} \right)^{\omega - \frac{1}{2}} \cong 88.4\ nm \tag{5.14}$$

where the VHS reference parameters for argon are $d_{ref} = 4.17$ Å, $T_{ref} = 273$ K, $\omega = 0.81$[16] and n is the number density. The CTC-DSMC time step was 5 ps ($\sim \tau_1/40$), where τ_1 is estimated using:

$$\tau_1 = \frac{1}{4 d_{ref}^2 n} \sqrt{\frac{m_{Ar}}{\pi k_B T_{ref}}} \left(\frac{T}{T_{ref}} \right)^{\omega - 1} \cong 222\ ps \tag{5.15}$$

where m_{Ar} is the mass of an argon atom. The CTC-DSMC timestep is necessarily smaller than the timestep used with the VHS collision model (typically $\tau/4$) because the CTC-DSMC collision cross-section is much larger than the VHS cross-section. For example, the constant cross-section model has a value of $d_{ref} \cong 13$ Å. The simulation domain contained $\sim 10^6$ particles, and the flow was initialized to the upstream and downstream conditions with a jump in the center of the domain. The CTC-DSMC simulation was run until it reached steady state ($\sim$500 CTC-DSMC time steps), after which macroscopic variable (ρ, T) and velocity distribution sampling began. The average density in a cell is given by:

$$\rho = \frac{\langle n_p \rangle w_p}{V_{cell}} \tag{5.16}$$

where n_p is the number of particles in a cell, w_p is the particle weight, V_{cell} is the cell volume, and the brackets $\langle\rangle$ indicate a time averaged sample. Temperature is sampled as:

$$T = \frac{m_{Ar}}{3k_B}\left[\left\langle v_x^2 + v_y^2 + v_x^2\right\rangle - \left(\langle v_x\rangle^2 + \langle v_y\rangle^2 + \langle v_x\rangle^2\right)\right] \tag{5.17}$$

where v_x is the particle velocity parallel to the flow. For plotting purposes, the generic flow variable q is normalized:

$$q_n = \frac{q - q_1}{q_2 - q_1} \tag{5.18}$$

where q_1 is the upstream value and q_2 is the downstream value. A comparison of the results for normalized temperature and density is shown in Fig. 5.5(a). A comparison of the velocity distribution functions $f(v_x)$ at different values of the normalized density in the shock is shown in Fig. 5.5(b). In these plots the x-axis is scaled by the most probable speed c_1:

$$c_1 = \left(\frac{2k_B T_1}{m_{Ar}}\right)^{\frac{1}{2}} \tag{5.19}$$

The bin width used for the velocity distribution functions is $c_1/10$, and all velocity distribution functions are normalized. In all cases we find that the CTC-DSMC and MD results are in perfect agreement.

5.4.3 Molecular Nitrogen Shock

We also compare the results of CTC-DSMC to MD for a $M_1 = 7$, $T_1 = 28.3$ K, $\rho_1 = 0.1$ kg/m^3 diatomic nitrogen shock. The CTC-DSMC simulation domain was 600 ($\sim 120\lambda_1$) cells in length, with a cell length of 67 nm ($\sim \lambda_1/5$). The CTC-DSMC time step was 50 ps ($\sim \tau_1/50$). The upstream mean free path is estimated as $\lambda_1 = 349$ nm, and the upstream mean collision time is estimated as $\tau_1 = 2.29$ ns using the VHS parameters for nitrogen: $d_{ref} = 4.17$, $\omega = 0.74$, $T_{ref} = 273$ K.[16] The DSMC domain was populated with $\sim 10^6$ particles. The rotational temperature is defined as:

$$T_{rot} = \frac{\langle e_{rot}\rangle}{k_B} \tag{5.20}$$

where e_{rot} is the rotational energy of a particle. A comparison between CTC-DSMC and MD for the normalized density and temperatures is shown in Fig. 5.6(a). The rotational energy distribution functions at different values of T_{rot} (normalized as in Eq. 10) in the

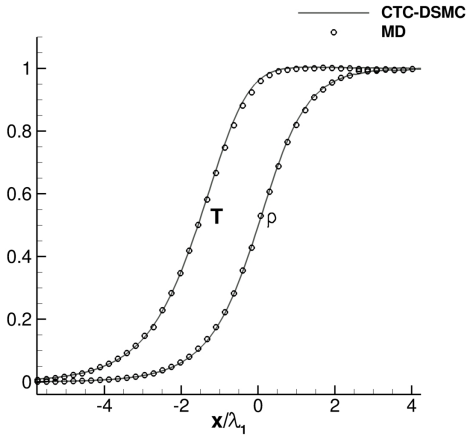

(a) Comparison of normalized density and temperature.

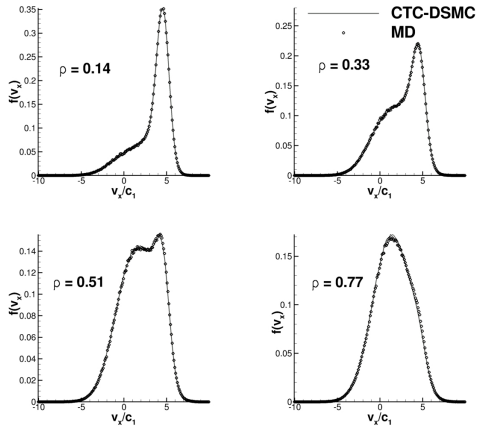

(b) Comparison of $f(v_x)$ distribution functions at different normalized densities.

Figure 5.5: Comparison of CTC-DSMC to MD for $M_1 = 5$, $T_1 = 300$ K, $\rho_1 = 1.0$ kg/m^3 argon shock.

shock are shown in Fig. 5.6(b). Rotational energies are binned to the nearest value of $j/10$, where j is the rotational quantum number for rigid rotor molecular nitrogen with a bond length of 1.094 Å. All of the rotational distribution functions are normalized. The results of CTC-DSMC and MD simulations are again in perfect agreement.

The MD density and rotational temperature profiles and rotational distribution functions shown in Fig. 5.6 have been previously validated with experimental data.[113] It is noted that no DSMC collision model exists that is able to exactly reproduce the MD results to this level of precision.[113] Thus for the flows considered in this work (and potentially for more complex flows), CTC-DSMC is shown to be purely a numerical acceleration technique for the MD simulation of dilute gases, as both methods require only the PES as a model input.

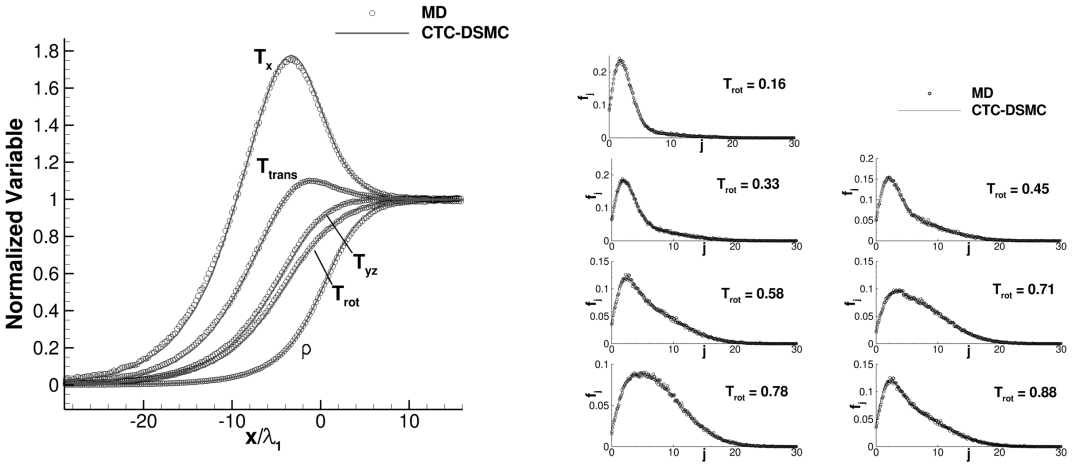

(a) Comparison of T, T_x, T_{yz}, T_{trans}, T_{rot}, ρ.

(b) Comparison of rotational distribution functions at different normalized rotational temperatures in the shock.

Figure 5.6: Comparison of CTC-DSMC to MD for $M_1 = 7$, $T_1 = 28.3$ K, $\rho_1 = 0.1$ kg/m^3 nitrogen shock

5.5 CTC-DSMC Acceleration with a CPU/GPU Parallelization Scheme

Even as a serial computation, the CTC-DSMC technique is less computationally intensive than parallel MD simulations because it eliminates the long periods of free flight between collisions and is not constrained to simulating every molecule in the flow. For example, a typical CTC-DSMC simulation for a 1D shock took days on one CPU in serial, while MD simulations took weeks on hundreds of CPUs.[98, 114, 112, 113] Nevertheless, to apply the CTC-DSMC technique to larger problems a parallelization scheme is needed. Code profiling of CTC-DSMC simulations has revealed that collisions take >99.9% of the total processor time during a simulation. Our parallelization approach is to execute the relatively cheap DSMC simulation steps (particle movement, sorting, collision pairing, sampling) on a single CPU in serial, while the more expensive trajectory calculations are processed in parallel across multicore CPUs and GPUs. At every DSMC time step the CTC-DSMC code must calculate the outcomes of a large number

of independent collisions. This type of problem lends itself to a Single Instruction Multiple Data (SIMD) approach. We will demonstrate a parallelization technique that makes use of multicore CPUs and GPUs. Graphical processing units are chosen because they have a high computational floating point performance and because their architecture is well suited to SIMD problems.[135]

Our test system consists of a computer with two Intel Xeon x5675 six-core 3.06 GHz processors (peak performance 73 GFlops/CPU) and four NVIDIA M2070 GPUs (peak performance 515 GFlops/GPU). Parallelization is accomplished using OpenMP[136] on the multicore CPUs and the NVIDIA's CUDA programming language[135] on the GPUs. The collision handling portion of the CTC-DSMC code is written in C and, with the exception of random number generation and memory read/writes, the collision code compiled on CPU/GPUs is identical. All GPU calculations are double precision, and we verified that both the CPU and GPU collision routines predicted identical results. The CPU code was compiled with the publicly available open source Gnu GCC compiler.[137] In both cases, the code is compiled with aggressive compiler optimization (-O3).

Parallelization of the collision code with OpenMP is easily accomplished by adding a `#pragma` statement over the loop executing collisions. The pseudocode for this approach is given in the Appendix A. We found that OpenMP parallelization resulted in a speedup of $\sim$11.5$\times$ vs. serial computation, demonstrating good use of the two six core processors on our test system. Parallelization is accomplished differently using CUDA. A GPU device has its own memory, and to carry out collisions on a GPU collision data must first be sent to the GPU and then retrieved after the GPU calculations are complete. We have found that the time taken to transfer collision data to and from the GPU is significantly less than the cost of carrying out collisions. For advanced interatomic potentials that are more computationally expensive than the LJ potential, this trend will continue. A typical CUDA subroutine is carried out using a large number of threads, which are organized into groups of blocks. Threads are executed in groups of 32 called warps.[135] A warp of threads must execute the same instruction simultaneously, and any code branching within the warp will result in serialization and significant decrease in performance. We have found that the naturally varying length of collisions is a significant cause of code branching in the present application. Before we show how to mitigate the effects of code branching on GPU performance due to variable collision

length, we will demonstrate a test case where this does not affect the GPU performance. In this case we use a simple code that measures the time taken to compute a group of 131,072 identical N_2-N_2 collisions. The GPU collision subroutine is executed with 512 blocks of 256 threads, with one collision per thread. Timing is accomplished with the OpenMP omp_get_wtime() function[136], and the transfer of collision data to and from the GPU is included in the timing. The colliding nitrogen molecules have a relative collision velocity of 421 m/s, rotational energies of 4.14×10^{-21} J, and identical impact parameters and molecular orientations. As shown in Table 5.2, the speedup from OpenMP is 11.53× the serial CPU time while the GPU speedup is 42.93× the serial CPU time. The GPU speedup over the CPU with OpenMP is $\sim$ 3.7×, which is close to the ratio of the peak floating point operations per second of the GPU and CPU ($\sim$ 3.5).

	CPU (Serial)	CPU (OpenMP)	GPU
Time (s)	145.91	12.65	3.34
Speedup	1	11.53	42.93

Table 5.2: Timing and speedups for a set of 131,072 identical N_2-N_2 collisions.

The GPU speedup can decrease due to the effects of variable collision length. For example, we considered a second test case where the velocities and rotational energies of colliding N_2 molecules were sampled from an equilibrium distribution at 300 K and the impact factors and initial molecular orientations were randomized. In this case, we found that the GPU speedup vs. serial was 9.48×. To decrease the effects of code branching due to variable collision length, we use an approach where each thread processes multiple collisions. Each block of threads is assigned a chunk of memory with collisions to process. After a thread is finished computing a collision, it uses a block-wise shared variable to determine the next collision available in memory. Detailed pseudocode for this algorithm is given in Appendix A.

This approach to processing collisions on GPUs reduces the effect of variable collision length on parallel efficiency. This is because an individual thread processes multiple collisions (on average `coll_per_thread`, as defined in the Appendix A), and threads can process a different number of collisions depending on the lengths of the collisions

they encounter. The effect of processing multiple collisions per thread is shown in the thread scheduling diagram in Fig. 5.7. If one thread is processing a collision that is longer than the other collisions within a warp (for example, the thread highlighted in red in Fig. 5.7(a)), this can significantly reduce the parallel efficiency because the other threads in the warp remain idle while waiting for this thread to finish. As shown in Fig. 5.7(b), with multiple collisions per thread this effect is significantly reduced. With this approach we are able to approach the speedup seen for identical collisions (shown in Table 5.2) for a sufficiently large values of `coll_per_thread`. Alternatively, it would be possible prevent code branching by assigning all collisions in a warp constant length. This could be accomplished by stopping all collisions within a warp (or block) only after the longest collision was finished by using a shared variable to communicate between threads. However, this approach would introduce inefficiency because some collisions would be integrated long after molecules were a distance D_{Cutoff} apart, after which no energy exchange between molecules occurs. The speed up of this approach vs. the time taken on a CPU in serial would be comparable to using only one collision per thread. For example, the idle threads shown in Fig. 5.7(a) would continue running until the longest collision in the warp finished, which would not alter the total time taken to calculate the outcomes of all of the collisions.

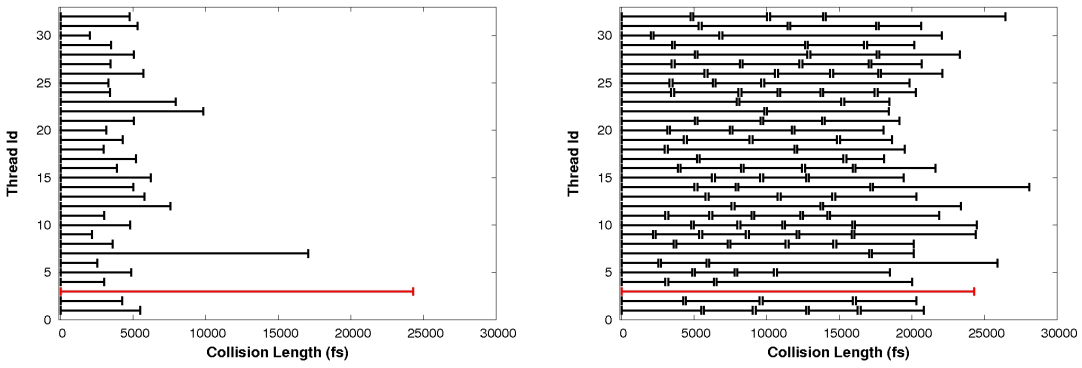

(a) `coll_per_thread` = 1 (b) `coll_per_thread` = 4

Figure 5.7: Thread Scheduling for a group of 32 threads. Thread #3 is highlighted in red. Each collision is represented by a bracketed line.

5.5.1 GPU parameter optimization

The parameters `threads_per_block`, `coll_per_thread`, and `n_blocks` (outlined in the Appendix A) are chosen to maximize the performance of the code on our specific GPU architecture. We have found that to maximize performance, it is optimal to have the largest value of `coll_per_thread` while not lowering the total number of threads running concurrently on the GPU to a value that decreases the overall efficiency. For the present calculations we use a constant value of `threads_per_block` = 64, with `coll_per_thread = rnd_down_pwr2(`N_{coll}`/4096)` and `n_blocks = rnd_up_pwr2(`N_{coll}`)/(colls_per_thread*threads_per_block)`. This approach keeps the number of blocks between 64 and 128 for any number of collisions. The GPU speedup for batches of collisions with velocities sampled from a Maxwell-Boltzmann distribution at 300 K are shown in Fig. 5.8. Notably, the GPU speedup increases with the number of collisions due to the increasing value of `coll_per_thread`. At very high numbers of collisions the benefits of increasing the `coll_per_thread` level off, with a maximum GPU speedup of around 32. The GPU speedup significantly drops off when the number collisions calculated simultaneously is below ∼64,000 (which corresponds to `coll_per_thread` = 16).

5.5.2 Load Balancing

When accelerating a CTC-DSMC simulation with a heterogeneous CPU/GPU combination, we apply load balancing to take maximum advantage of both resources. Specifically, the CPU processes all collisions with relative speeds under some threshold g_{div}, while the remaining collisions are equally distributed to the GPUs. This approach gives a higher overall speedup than allowing the CPU and separate GPUs to handle individual domains within the flow. It increases the number of collisions handled by GPUs by sending a larger number of shorter collisions to the GPUs and a smaller number of longer collisions to the CPU. This increases the number of collisions processed simultaneously per GPU, leading to a greater overall speedup. Additionally, because GPUs process collisions at higher relative velocities, this reduces the deviation in collision lengths and increases the efficiency of the thread handling approach described in the previous section. To perform dynamic load balancing, at each time step the value of g_{div} is modified

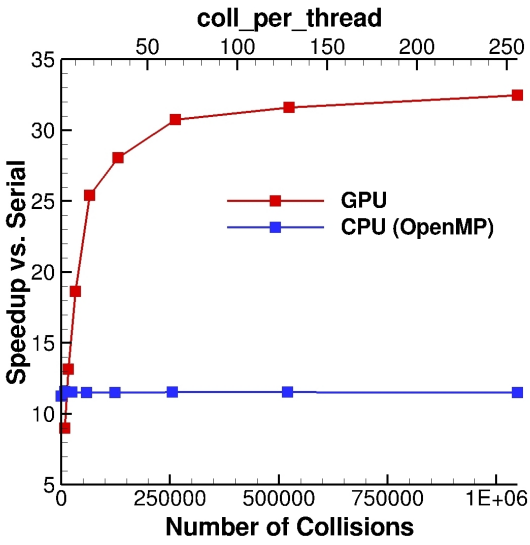

Figure 5.8: GPU and CPU speedup for various collision batch sizes. Molecule translational and rotational energies are sampled from a Boltzmann distribution at 300 K.

based on a simple diffusion model:

$$\Delta g_{div} = D\frac{(t_{GPU,avg} - t_{CPU})}{(t_{GPU,avg} + t_{CPU})} \times g_{div} \tag{5.21}$$

where D is a diffusion constant (0.25 here), $t_{GPU,avg}$ is the average time taken for all of the GPUs to carry out collisions, and t_{CPU} is the time taken for the CPU to carry out collisions. For a system of 2 GPUs and 1 CPU, the results of load balancing for the nitrogen shock simulation described in section 3.2 are shown in Fig. 5.9. Figure 5.9(a) shows the number of collisions processed by each CPU/GPU vs. CTC-DSMC iteration. The GPUs process many more collisions than the CPU, because the collisions they process are shorter. The CPU processes all collisions with $g < g_{div}$, and the evolution of g_{div} with time is shown in Fig. 5.9(b). As shown in Fig. 5.9(c), the load balancing achieves equal load between the CPU/GPUs after about 25 CTC-DSMC time steps for the chosen initial value for g_{rel}. The cost of a load balancing step is 2× the cost of a non-load balancing step if the loads are equally balanced between the CPU/GPUs because the CPU and GPUs are timed separately. For non-load balancing steps, the CPU and GPU computations are run simultaneously.

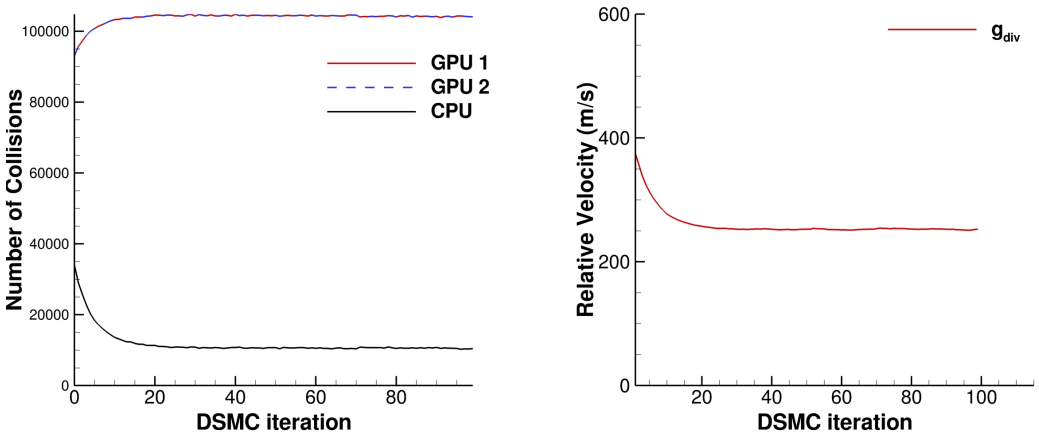

(a) Number of collisions vs. DSMC iteration.

(b) g_i vs. DSMC iteration

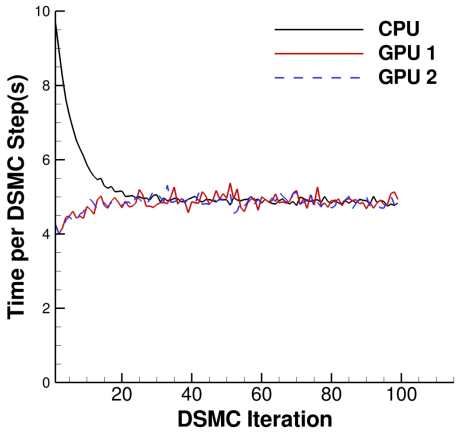

(c) Computational time vs. DSMC iterations.

Figure 5.9: Load balancing between two GPUs and CPU.

5.5.3 Acceleration of 1-D Nitrogen Shock

To demonstrate the efficiency of the parallelization scheme, we consider a test case of the $M_1 = 7$ nitrogen shock described in section 5.4. We consider test configurations with 1, 2, and 4 GPUs. In each case, load balancing is performed for 50 CTC-DSMC

time steps to find the appropriate value of g_{rel} for each configuration. The time taken to run the subsequent 100 CTC-DSMC steps serves as a basis for the average time per DSMC step shown for various configurations in Table 5.3. While the shock has not reached steady state at such short times, we have found that the computational cost and load balancing does not change significantly at steady state.

	$\sim 10^6$ molecules			$\sim 4\times10^6$ molecules		
	$\frac{\text{time}}{\text{step}}$(s)	speedup	speedup/GPU	$\frac{\text{time}}{\text{step}}$(s)	speedup	speedup/GPU
CPU (serial)	373.31	1	-	1491.43	1	-
CPU (omp)	32.39	11.52	-	129.66	11.50	-
1 GPU	7.79	47.91	36.41	29.86	49.94	38.44
2 GPU	5.17	72.27	30.39	17.79	83.85	36.17
4 GPU	3.69	101.23	22.44	10.59	140.81	32.33

Table 5.3: Parallel scaling for GPU accelerated CTC-DSMC simulations. OMP = OpenMP. The speedup/GPU is calculated as (speedup-11.5)/(# of GPUs).

As shown in Table 5.3, the maximum speedup achieved is 140.81× for a shock with 4×10^6 particles. We present this case to show how the GPU enabled speedup would scale to larger flows requiring more particles. The GPU speedup is higher for simulations with a larger number of particles because GPUs process more collisions per time step. For the the shock with 10^6 particles there are ∼220,000 collisions per CTC-DSMC time step, and for the shock with 4×10^6 particles there are ∼880,000 collisions per CTC-DSMC time step. A maximum speedup per GPU of 38.44× is achieved for the case with 4×10^6 particles with 1 GPU+CPU(OMP), which closely approaches the speedup achieved for identical collisions (42.93×). This implies that our simple approach of performing multiple collisions per thread and performing the slowest collisions on the CPU is effective, and more elaborate schemes are not expected to increase the parallel performance significantly. For the case with the fewest number of collisions per GPU (4 GPUs + CPU(OMP), 10^6 particles in shock), the speedup per GPU drops to 22.44×. The speedup per GPU remains above 30× for all of the cases where each GPU handles >110,000 collisions per CTC-DSMC time step.

The parallel speedup achieved by our CTC-DSMC implementation is similar to

the speedup achieved in other works with similar hardware. For example, although flow-problem dependent, Su *et al.* achieved a maximum speedup of 15×/GPU when parallelizing the entire DSMC algorithm with a similar hardware configuration.[138] However, the DSMC simulations employed a uniform Cartesian grid, a uniform time step, planar geometry, and a pure argon gas. These specific simplifications enable the movement, indexing, and collision routines of DSMC to be efficiently threaded on GPUs. By comparison, more complex DSMC collision models (which include internal energy exchange and chemistry) and raytracing movement (which is necessary for more complex grids/geometries) involve algorithm branching and thus pose significant challenges for SIMD techniques.[139]

In contrast, the CTC-DSMC method is inherently suited for SIMD implementation and, as outlined in this paper, parallelizing a serial CTC-DSMC code requires minimal programming effort. One important point (often not addressed in similar GPU articles) is that our speedup values are obtained by comparing essentially identical trajectory integration code on both the CPU and GPUs, thus providing a rigorous and fair comparison between the methods. We believe that such a CTC-DSMC implementation is scalable to large CPU/GPU clusters. Because the DSMC contribution to the computational load is very small for CTC-DSMC and is not threaded across the GPUs, large problems can be partitioned using spatial domain decomposition across compute nodes (using MPI) while maintaining all state-of-the-art DSMC capabilities.[140, 141, 142, 143] Subsequently, within each node (consisting of multi-core CPUs and/or GPUs) the CTC collision algorithms can be threaded using the SIMD approach.

The shock wave test cases presented in this article demonstrate that high parallel efficiency is achieved if roughly one million particles are simulated per GPU (see Table 5.3). A simulation where each GPU is loaded with one million particles can run ∼10,000 DSMC steps in one day, which is quite fast considering the large amount of data processed by a CTC-DSMC simulation. Many large clusters of CPU/GPU compute nodes, such as the Air Force Research Laboratory (AFRL) Condor cluster in Rome, NY, are already in use today. This cluster is comprised of 84 compute nodes, each containing a dual six-core CPU and 2 Nvidia GPUs (164 GPUs in total). Existing DSMC parallelization strategies are scalable over $O(100)$ partitions, so the speedups reported in this article within a single compute node (a single partition) would directly scale on such

a parallel cluster. The Condor cluster would thus enable simulations on the order of 164 million particles to be obtained in the order of days for the N_2-N_2 collision model presented here. This problem size is adequate to simulate near-continuum flow over axisymmetric geometries or rarefied flow over 3D geometries, and parallel computing power is certain to increase further in the coming years.

5.6 Simulating Rotating Vibrating Molecules with CTC-DSMC

Classical trajectory calculations are expected to provide only an approximate description of molecular vibration at vibrational temperatures below the characteristic vibrational temperature of nitrogen ($T_v < \theta_v$) due to the large spacing between vibrational energy levels. At higher temperatures ($T_v > \theta_v$) where vibrational quantum levels are closely spaced, a classical description of vibration is expected to be more accurate.

There are several issues that need to be addressed in order carry out CTC-DSMC simulations with vibrating molecules. One issue is how the boundary conditions of 1D shocks should be determined. The jump conditions for a shock composed of a gas with classical and quantized vibration are different because of differences in the amount of energy in the vibrational mode between the classical and quantum descriptions. Because CTC-DSMC simulations are classical in nature, the quantum boundary conditions cannot be exactly matched. A modification to the quantum boundary conditions which allows upstream and downstream flow variables close to the exact quantum values is presented in section 5.6.2. At higher temperatures, molecules experience rovibrational coupling, which causes issues with molecular initialization based on the rigid rotor/harmonic oscillator approximation. A partial fix which accounts for centrifugal bond stretching is given in section 5.6.1. Additionally, the definition of vibrational and rotational temperature must be corrected to account for the additional energy in these modes due to rovibrational effects.

To describe N_2-N_2 interactions, we use the site-to-site LJ potential described in section 5.4. This potential is not expected to provide an accurate description of the vibrational relaxation rate, however, none of the phenomena addressed here depend on this rate. Unless otherwise specified, molecular vibration is described by a harmonic

potential with a spring constant corresponding to a vibrational temperature (θ_v) of 3374 K[105]:

$$\theta_v = \frac{h\sqrt{k/\mu}}{2\pi k_B} \tag{5.22}$$

where h is Planck's constant, k is the spring constant, and μ is the reduced mass. Solving for k gives a spring constant of $k = 2269$ (N/m).

5.6.1 High Temperature Effects: Rotation-Vibration Coupling

At high temperatures, the model of diatomic molecules as a rigid rotor/harmonic oscillator is no longer valid due to rotational and vibrational coupling. From the perspective of CTC-DSMC simulations, this has consequences in two areas: molecular initialization (how vibrational and rotational velocities are set based on vibrational and rotational energies) and temperature sampling (how temperature is determined from the cell averaged vibrational/rotational energy). In the rigid rotor/harmonic oscillator approximation, we use initialization scheme 1:

1. Set bond length: $r = r_0 = 1.094$ Å
2. Set rotational velocity: $v_r = \sqrt{E_r/m_N}$
3. Set vibrational velocity: $v_v = \sqrt{E_v/m_N}$

where v_r and v_v are the rotational and vibrational velocities, E_r and E_v are the rotational and vibrational energies, and r_0 is the equilibrium bond length. After or during a collision, the rotational and vibrational energy are determined as:

$$E_r = m_N v_r^2 \tag{5.23}$$

$$E_v = m_N v_v^2 \tag{5.24}$$

To determine the rotational and vibrational temperatures, we use temperature definition 1:

$$T_r = \langle E_r \rangle / k_B \tag{5.25}$$

$$T_v = \langle E_v \rangle / k_B \tag{5.26}$$

Where the brackets $\langle\rangle$ denote cell based averages. This definition of vibrational temperature is classical, and a different definition based on quantized vibration is given in the next section. The rotational and vibrational energy at flow boundary conditions are sampled from the classical distribution for a fully excited mode with two degrees of freedom[16]:

$$E_{r/v} = -k_B T \ln(R_f) \tag{5.27}$$

However, the above molecular initialization scheme and temperature definitions are not adequate at higher temperatures. For example, Figure 5.10 shows T_t, T_r, T_v in a uniform $M = 3$ flow with an upstream temperature of 10,000 K as simulated by CTC-DSMC. Notably, at the inflow T_v is much higher than T_r, and neither are equivalent to T_t. This is a molecular initialization issue, and a partial fix is discussed below. Additionally, Fig. 5.10 shows that T_v (based on the definition in Eq. 5.26) does not equilibrate with T_r, T_t. This is because the definition of temperature given in Eqs. 5.25-5.26 does not account for the fact that the specific heat of rotating, vibrating molecules is not constant, but rather changes with T due to rovibrational effects.[103] A better way to define $\mathrm{T}_v(\langle E_v \rangle)$ is also discussed below.

At the high temperature in Fig. 5.10, we would expect real molecular nitrogen to almost completely dissociate. However, here we are using a harmonic potential, which does not allow for molecular dissociation. While using a potential that allows for dissociation is desirable, at present we only focus on CTC-DSMC simulations of bound molecules, which can be useful in determining vibrational relaxation/excitation rates before dissociation occurs.

Molecular Initialization

The most easily characterized rovibrational effect is bond stretching due to centrifugal force. For a molecule with zero vibrational energy, we can find the rotating equilibrium bond length r_{req} by balancing the centrifugal and bond forces:

$$F_{\text{cent}} + F_{bond} = 0 \tag{5.28}$$

For a harmonic oscillator with a spring constant k this becomes:

$$\frac{m_N v_r^2}{r_{req}/2} - k_a(r_{req} - r_0) = 0 \tag{5.29}$$

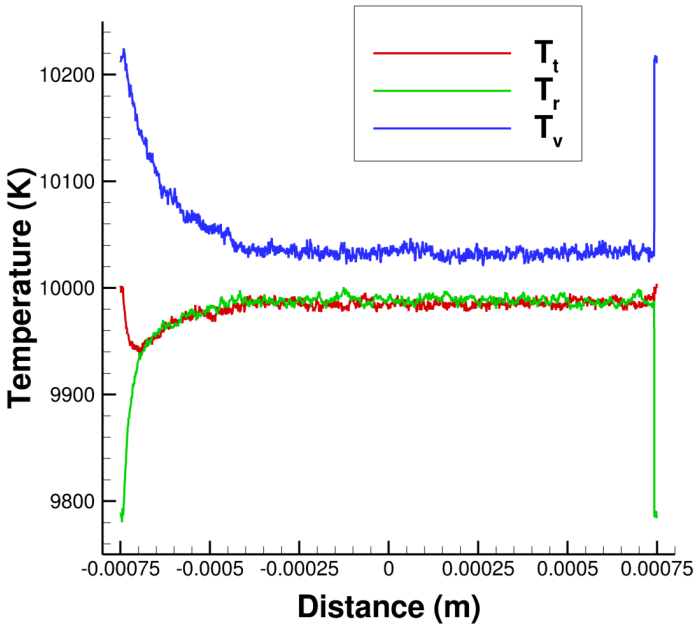

Figure 5.10: Translational, rotational and vibrational temperature for uniform 10,000 K, $M = 3$, $\rho = 0.1$ kg/m^3 flow with initialization scheme 1 and temperature definition 1

where k_a is $k/2$ (k_a is the force experienced by an individual atom) and r_0 is the equilibrium bond length. Solving for r_{req} gives:

$$r_{req} = \frac{r_0 + \sqrt{r_0^2 + 4m_N v_r^2/k_a}}{2} \tag{5.30}$$

For molecules that are rotating and vibrating, a useful concept is that of the effective rotational potential[21]:

$$U_{eff}(r) = \frac{L^2}{2m_n(r/2)^2} \tag{5.31}$$

$$U_{tot}(r) = U_{bond}(r) + U_{eff}(r) \tag{5.32}$$

$$U_{tot}(r) = \frac{1}{2}k(r - r_0^2) + \frac{2L^2}{m_n r^2} \tag{5.33}$$

where L, the angular momentum of the molecule, does not vary with time because it is conserved. As shown in Fig. 5.11(a), the addition of the effective rotational potential to the harmonic potential gives a total potential with a minimum at r_{req}, which is always greater than or equal to r_0. Rotating vibrating molecules also experience rovibrational coupling. For example, E_r, E_v vs. time for a molecule initialized with rotational and vibrational energy of 20,000 K are shown in Fig. 5.11(b). The vibrational and rotational energy vary significantly with time ($\pm$ 5000 K) due to rovibrational coupling. The anharmonicity of the oscillations of E_r, E_v causes the time averaged values ($\overline{E_r}$, $\overline{E_v}$) to not be equivalent to their initialized values. This anharmonicity is caused by the effective rotational potential.

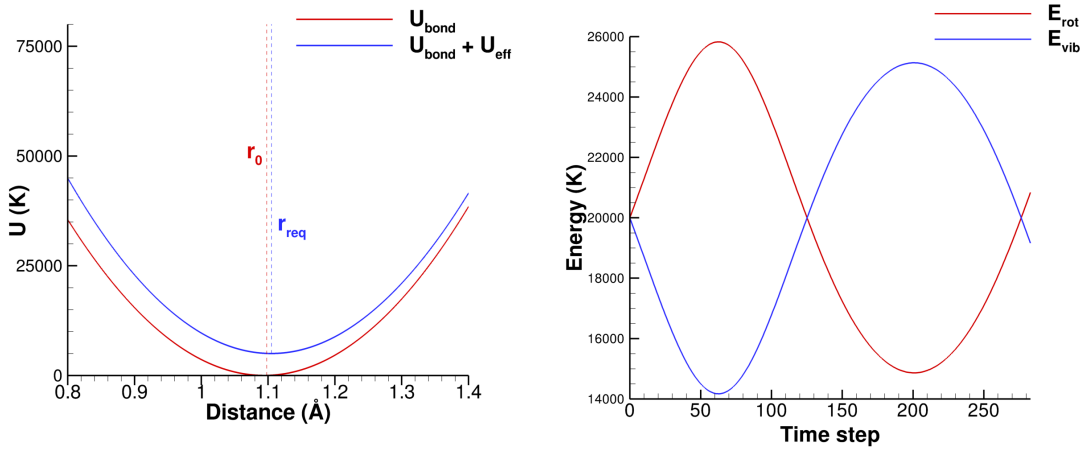

(a) U_{bond}, $U_{bond} + U_{eff}$

(b) First period of the oscillation of E_r, E_v

Figure 5.11: Rovibrational couping due to the effective rotational potential

The effect of centrifugal bond stretching and anharmonic oscillations in the rotational and vibrational energies causes a molecule initialized with some $E_{r,i}$,$E_{v,i}$ to not maintain these values in a time average. This is the cause of the difference between T_v, T_r and T_t at the inflow in Fig. 5.10. A complete solution to this problem would entail solving the equations of motion of the rotating, vibrating molecule to find some mapping between $E_{r,i}$, $E_{v,i}$ and $\overline{E}_r$, $\overline{E}_v$. Additionally, a complete solution would have to address how to correctly sample from the rovibrational energy distribution. Currently,

vibration and rotation are sampled independently. This is somewhat incorrect, as some combinations of $\overline{E}_r$, $\overline{E}_v$ cannot exist. For example a molecule with a high rotational energy will on average have some vibrational energy due to centrifugal bond stretching.

A simple way to reduce the initialization error in T_r, T_v is to account for centrifugal bond stretching (initialization scheme 2):

1. Set rotational velocity: $v_r = \sqrt{E_r/m_N}$
2. Set bond length: $r = r_{req} = \frac{r_0+\sqrt{r_0^2+4m_N v_r^2/k_a}}{2}$
3. Calculate energy due to centrifugal bond stretching: $E_{v,cent} = \frac{1}{2}k(r_0 - r_{req})^2$
4. Set vibrational velocity: $v_v = \sqrt{(E_v - E_{v,cent})/m_N}$
   In cases where $E_v < E_{v,cent}$, use $v_v = \sqrt{E_{v,cent}/m_N}$

As shown in Fig. 5.12, initialization scheme 2 reduces the magnitude of the the difference between T_r, T_v by about a factor of two, while also switching their values relative to T_t. It would be possible to make additional adjustments to molecular initialization to further reduce the error. For example, we have observed that the next order correction is linearly proportional to the initial rotational and vibrational energy:

$$e_{anh} = CE_{r,i}E_{v,i} \tag{5.34}$$

However, in practical terms the initialization error is relatively minor ($\sim 1\%$ with initialization scheme 2), and can always be mitigated by allowing the flow to propagate a small distance.

Sampling of Rotational and Vibrational Temperature

To determine the effect of temperature on the energy in rotation and vibration, we ran 0D simulations with the translational velocity of each molecule sampled from a Boltzmann distribution at the desired temperature at each DSMC time step, effectively thermostatting the system. As shown in Fig. 5.13(a), for a system at 40,000 K the vibrational energy is ∼700 K higher than the translational temperature, while the rotational temperature is ∼50 K higher than the translational temperature. As shown in

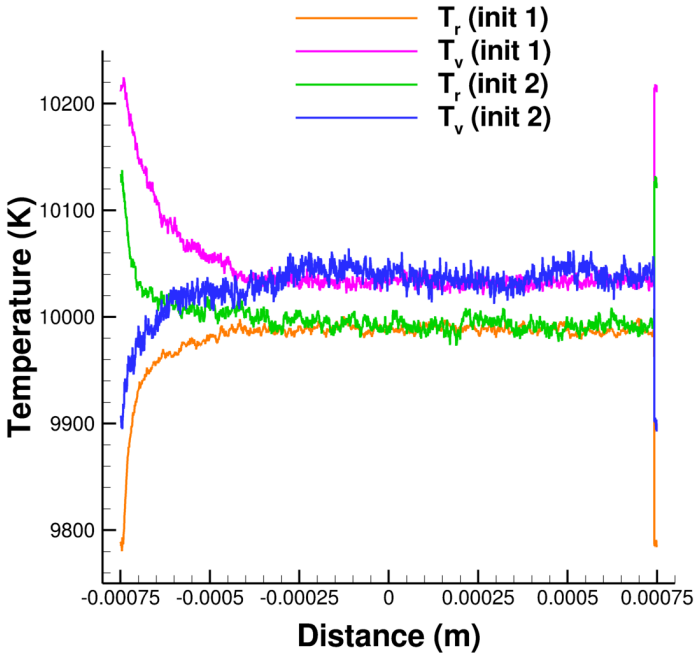

Figure 5.12: Comparison of different molecular initialization methods. Translational, rotational and vibrational temperature for uniform 10,000 K, $M = 3$, $\rho = 0.1$ kg/m^3 flow

Fig. 5.13(b), the trends in rotational and vibrational energy both follow a second order polynomial with temperature:

$$\langle E_{\text{anh,r}}(T)\rangle = \langle E_r\rangle - k_B T = C_{\text{anh,r}} T^2 \tag{5.35}$$

$$\langle E_{\text{anh,v}}(T)\rangle = \langle E_v\rangle - k_B T = C_{\text{anh,v}} T^2 \tag{5.36}$$

where $C_{\text{anh,v}} = 4.513\times10^{-7}$ (K^{-1}) and $C_{\text{anh,r}} = 4.695\times10^{-8}$ (K^{-1}). These expressions are in agreement with the expression from Vincenti and Kruger[103]:

$$E_{anh}(T) = CR\frac{\theta_r}{\theta_v}T^2 \tag{5.37}$$

although it is unclear whether this is meant to be applied to rotation, vibration, or both combined. This expression was originally derived by Landau and Lifshitz[144],

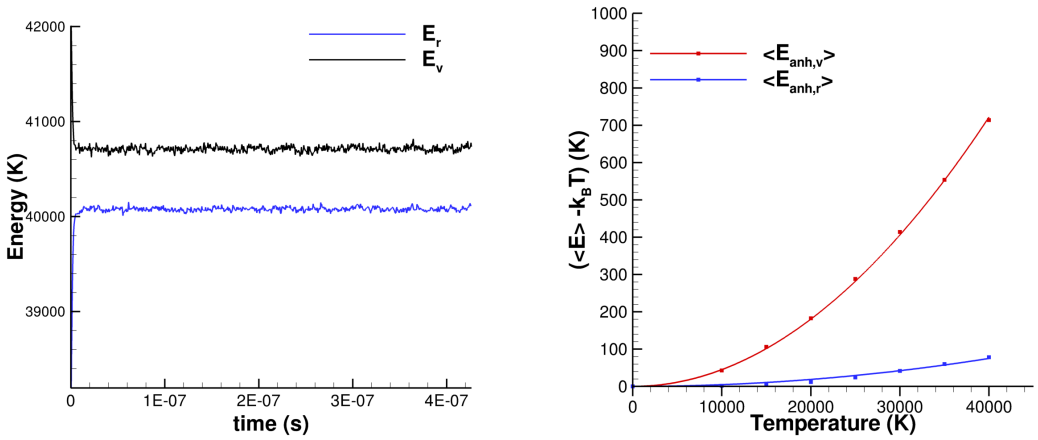

(a) E_r, E_v vs. time in 0D thermostatted system at 40,000 K

(b) $\langle E_{anh,r} \rangle$, $\langle E_{anh,v} \rangle$ vs. T

Figure 5.13: Effect of T on E_r, E_v

and is based on classical statistical mechanics, which is why it works for these classical simulations.

To account for the extra energy in rotation and vibration, the rotational and vibrational temperatures are:

$$T_r = \frac{-1 + \sqrt{1 + 4C_{\text{anh,r}} \langle E_r \rangle / k_B}}{2C_{\text{anh,r}}} \tag{5.38}$$

$$T_v = \frac{-1 + \sqrt{1 + 4C_{\text{anh,v}} \langle E_v \rangle / k_B}}{2C_{\text{anh,v}}} \tag{5.39}$$

To sample energies from the classical distributions, we must modify the temperatures used in the sampling expressions to account for the extra energy in vibration and rotation:

$$E_r = -k_B T_r' log(R_f) \tag{5.40}$$

$$E_v = -k_B T_v' log(R_f) \tag{5.41}$$

where T_r' and T_v' are:

$$T_r' = T_r + C_{\text{anh,r}} T_r^2 \tag{5.42}$$

$$T_v' = T_v + C_{\text{anh,v}} T_v^2 \tag{5.43}$$

We call the above equations temperature definition 2. As shown in Fig. 5.14, with temperature definition 2, in the uniform flow at 10,000 K, T_t, T_r and T_v all equilibrate to 10,000 K.

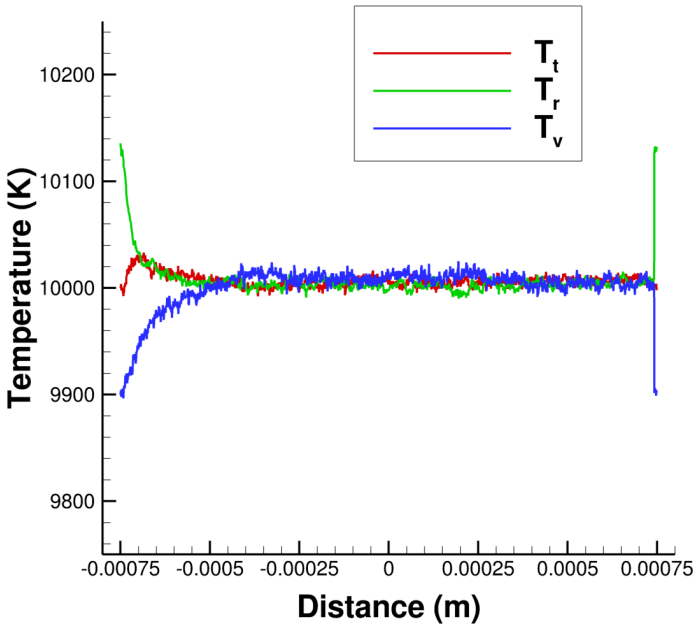

Figure 5.14: Translational, rotational and vibrational temperature for uniform 10,000 K, $M = 3$, $\rho = 0.1$ kg/m^3 flow with temperature definition 2

Effect of Anharmonic Corrections to the Harmonic Potential

At high temperatures it is also appropriate to consider the effect of using a more realistic potential for describing molecular vibration. The harmonic potential is only accurate in describing vibrational motion at lower energies. A better description can be provided

by the Morse potential:

$$V(r) = D_e \left(1 - e^{-a(r-r_0)}\right)^2 \tag{5.44}$$

We use the parameters: $D_e = 1.56853\times10^{-18}$ J[105], $a = 2.68948\times10^{10}$ m, where D_e is the bond dissociation energy and a is based on the harmonic spring constant (see below). For the present we only wish to consider bound molecules (no dissociation). Therefore, we will use a Taylor expansion of the Morse potential to create a more realistic anharmonic potential. If we consider the Morse potential in terms of $V(x)$, where $x = r - r_0$, the first 6 terms of the Taylor expansion are:

$$V(x) = V(0) + V'(0)x + \frac{V''(0)x^2}{2} + \frac{V'''(0)x^3}{6} + \frac{V''''(0)x^4}{24} + \frac{V'''''(0)x^5}{120} + \frac{V''''''(0)x^6}{720} + ... \tag{5.45}$$

$$V(x) = a^2 D_e x^2 - a^3 D_e x^3 + \frac{7}{12}a^4 D_e x^4 - \frac{1}{4}a^5 D_e x^5 + \frac{31}{360}a^6 D_e x^6 + ... \tag{5.46}$$

The first term is equivalent to a harmonic potential, and the parameter a is determined using the bond dissociation energy (D_e) and the harmonic spring constant k from above. We will consider the anharmonic potential created by using the Taylor expansion up to the fourth and sixth order terms (odd order terms allow dissociation at large x). As shown in Fig. 5.15, the 4th (subsequently abbreviated TAY4) and 6th (subsequently abbreviated TAY6) order Taylor expansions provide a good description of the repulsive wall of the Morse potential, while providing an increasingly accurate description of the attractive region of the potential for higher order expansions.

We are interested in how the addition of anharmonicity to the potential changes the energy in vibration and rotation at different temperatures. We carried out additional thermostatted 0D CTC-DSMC simulations as described above with the anharmonic vibrational potentials. As shown in Fig. 5.16, using the anharmonic potentials causes an increasing amount of energy to be present in the rotational and vibrational modes. Of particular interest is that for the TAY4 and TAY6 potentials, the energy in vibration is significantly greater than $k_B T$ at lower temperatures where nitrogen will not be fully dissociated. Thus it is likely that these rovibrational effects will also be important when using the Morse potential in CTC-DSMC simulations. The trends in $\langle E_{\mathrm{anh,v}}(T)\rangle$ vs. T in Fig. 5.16 do not follow a quadratic form for the anharmonic potentials, but rather have a maxima and begin to decrease.

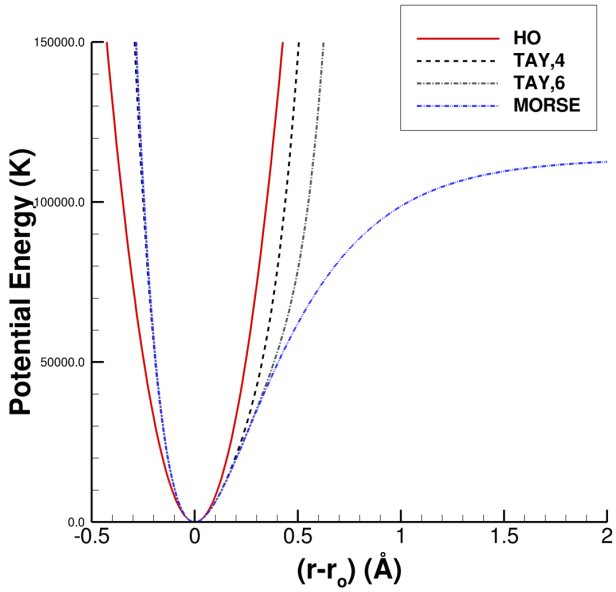

Figure 5.15: Morse potential approximated with different levels of Taylor expansion. HO = harmonic oscillator, TAY4 = 4th order Taylor expansion of the Morse potential, TAY6 = 6th order Taylor expansion of the Morse potential

5.6.2 Low Temperature Effects: Quantum vs. Classical Vibration

At lower temperatures ($T < \theta_v$), the differences between classical and quantum description of molecular vibration become significant. For the flows considered here, we will neglect the high temperature rovibrational corrections discussed above. All molecules are initialized with initialization scheme 1 from above.

Boundary Conditions

There are difficulties associated with attempting to describe molecular vibration with classical mechanics. One issue is the amount of energy in the vibrational mode at lower temperatures. At equilibrium the average vibrational energy of a system of quantum harmonic oscillators, including the zero point vibrational energy, is[103]:

$$E_{v,\text{quant}} = R\theta_v \left(\frac{1}{2} + \frac{1}{\exp(\theta_v/T) - 1} \right) \tag{5.47}$$

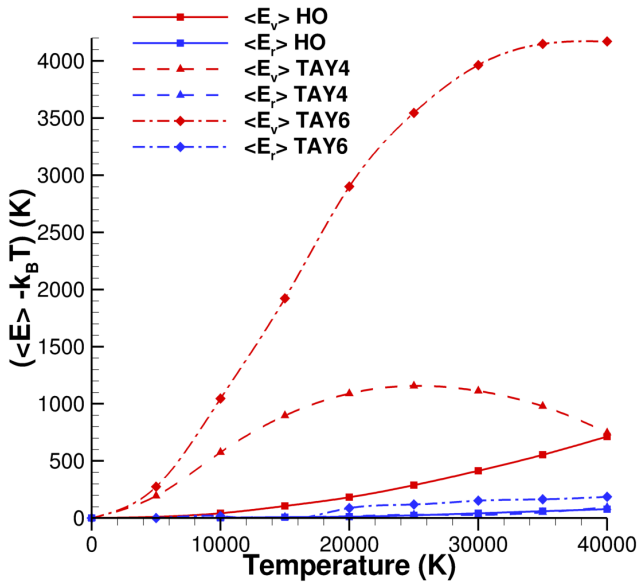

Figure 5.16: $\langle E_{anh,r} \rangle$, $\langle E_{anh,v} \rangle$ vs. T for different potentials. HO = harmonic oscillator, TAY4 = 4th order Taylor expansion of the Morse potential, TAY6 = 6th order Taylor expansion of the Morse potential

where R is the specific gas constant for molecular nitrogen. In contrast, the average vibrational energy of a system of classical harmonic oscillators is:

$$E_{v,\text{class}} = RT \tag{5.48}$$

This difference affects γ (in this context γ is the ratio of specific heats, and not a recombination coefficient), which is defined as:

$$\gamma = \frac{C_v + R}{C_v} \tag{5.49}$$

where C_v is the specific heat at constant volume. Therefore, the speed of sound ($a = \sqrt{\gamma RT}$) of the gas is also effected. For a gas composed of classical harmonic oscillators γ is constant ($\gamma_{\text{class}} = 9/7$), while γ varies with temperature for a gas composed of quantum harmonic oscillators ($\gamma_{\text{quant}}(T)$ is shown in Fig. 5.17).

This difference between classical and quantized vibration alters the boundary conditions of a 1D shock. To find the boundary conditions for a 1D shock we solve shock

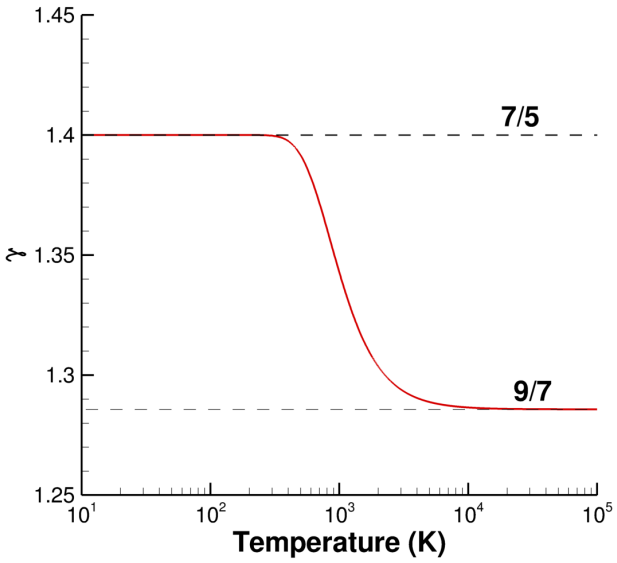

Figure 5.17: $\gamma_{\text{quant}}(T)$ for quantum harmonic oscillator N_2

jump conservation conditions for mass, momentum, and energy[103]:

$$\rho_1 u_1 = \rho_2 u_2 \tag{5.50}$$

$$p_1 + \rho_1 u_1^2 = p_2 + \rho_2 u_2^2 \tag{5.51}$$

$$h_1 + u_1^2/2 = h_2 + u_2^2/2 \tag{5.52}$$

For a classical gas we use:

$$h_{\text{class}} = \frac{9}{2} RT \tag{5.53}$$

while for a quantum gas we use:

$$h_{\text{quant}} = R\left(\frac{7}{2}T + \frac{\theta_v}{e^{\theta_v/T} - 1} + \frac{\theta_v}{2}\right) \tag{5.54}$$

As a test case we will consider a $M_1 = 10$, $T_1 = 300$ K, $\rho_1 = 0.1$ kg/m^3 shock (a similar shock was experimentally measured by Alsmeyer[145]). As shown in Table 5.4,

the upstream and downstream flow boundary conditions are different for the classical and quantum gases. In the shock composed of classical gas, the upstream flow speed (u_1) differs from the value predicted for a quantum gas by ∼350 (m/s) because the speed of sound differs for these two models. The downstream flow variables are also different due to the different definitions of enthalpy. In subsequent calculations, we refer to the values in Table 5.4 as the classical and quantum boundary conditions.

	Classical	Quantum
u_1 (m/s)	3383.5	3530.7
ρ_1 (kg/m^3)	0.1	0.1
T_1 (K)	300	300
u_2 (m/s)	452.5	499.1
ρ_2 (kg/m^3)	0.748	0.707
T_2 (K)	4509.0	5140.4

Table 5.4: Upstream and downstream boundary conditions for classical and quantum gases

Vibrational Energy Distribution Sampling

For classical harmonic oscillators, the vibrational energies of molecules at a given temperature are initialized using the expression in Eq. 5.27 and the vibrational temperature is given by the expression in Eq. 5.26. For quantum harmonic oscillators, the vibrational energy is initialized with the following expression using tabulated probabilities:

$$P(j) = \frac{e^{-E_v(j)/(k_B T)}}{q_{vib}(T)} \tag{5.55}$$

where j is the vibrational quantum number[105]. The vibrational energy at a given vibrational energy level j is:

$$E_v(j) = (j + 1/2)k_B\theta_v \tag{5.56}$$

and the vibrational partition function is:

$$q_v(T) = \frac{e^{-\theta_v/2T}}{1 - e^{-\theta_v/T}} \tag{5.57}$$

The difference between the classical and quantum initialization methods is significant at low temperatures. For example, if initializing molecules from the quantum energy distribution at $T = 300$ K, this means that $\mathrm{T}_{v,\mathrm{class}} \cong \theta_v/2$. To define the quantum vibrational temperature we use the expression:

$$\langle E_v \rangle = k_B \left(\frac{\theta_v}{2} + \frac{\theta_v}{e^{\theta_v/T} - 1} \right) \tag{5.58}$$

and invert it to obtain:

$$T_{v,\mathrm{quant}} = \frac{\theta_v}{\ln\left(\left(\frac{1}{\langle E_v \rangle / k_B\theta_v - 1/2} \right) + 1 \right)} \tag{5.59}$$

The classical and quantum expressions for temperature as a function of vibrational energy are shown in Fig. 5.18. In cases where $\langle E_v \rangle < k_B\theta_v/2$, we set $T_{v,\mathrm{quant}} = 0$. For flows simulated with CTC-DSMC, the classical vibrational temperature ($\mathrm{T}_{v,\mathrm{class}}$) is always more meaningful for describing the state of the system than the quantum vibrational temperature ($\mathrm{T}_{v,\mathrm{quant}}$) because the classical vibrational temperature will always eventually reach equilibrium with the translational and rotational temperatures.

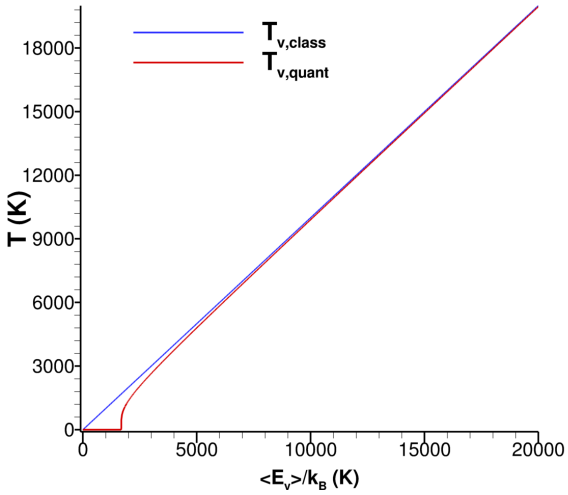

Figure 5.18: Temperature as a function of average vibrational energy with classical and quantum approaches

CTC-DSMC Simulation Results for a 1D shock with Rotating Vibrating Molecules

This section describes CTC-DSMC simulations of the $M_1 = 10$, $T_1 = 300$ K, $\rho_1 = 0.1$ kg/m^3 shock with the boundary conditions given in Table 5.4. For the shock with quantum boundary conditions the vibrational energies of molecules are sampled from the quantum distribution (Eq. 5.55), while for the shock with classical boundary conditions the classical definition is used (Eq. 5.27). In both cases, we use a domain populated with 500,000 particles with a length of 1.0 μm. A uniform 1D grid consisting of 1250 cells is used, giving a cell length of 80 nm. Based on the VHS parameters for nitrogen ($d_{ref} = 4.17$ Å, $\omega = 0.74$)[16], the mean free paths for the quantum boundary conditions are $\lambda_1 = 616$ nm and $\lambda_2 = 172$ nm. The DSMC time step was 10 ps and the MD timestep was 0.25 fs. The shock profile was allowed to develop for 40,000 DSMC time steps, after which sampling began.

Classical Boundary Conditions

In this case the boundary conditions and vibrational sampling are physically consistent with the properties of the gas being simulated. Therefore it is not surprising that in this CTC-DSMC simulation the shock location was steady. However, because vibration in a real nitrogen gas cannot be described classically at low temperatures, the flow boundary conditions are not the same as those for a realistic 1D nitrogen shock. The time averaged shock profile for the normalized flow variables after 80,000 DSMC steps is shown in Fig. 5.19(a), and the u velocity profile is shown in Fig. 5.19(b).

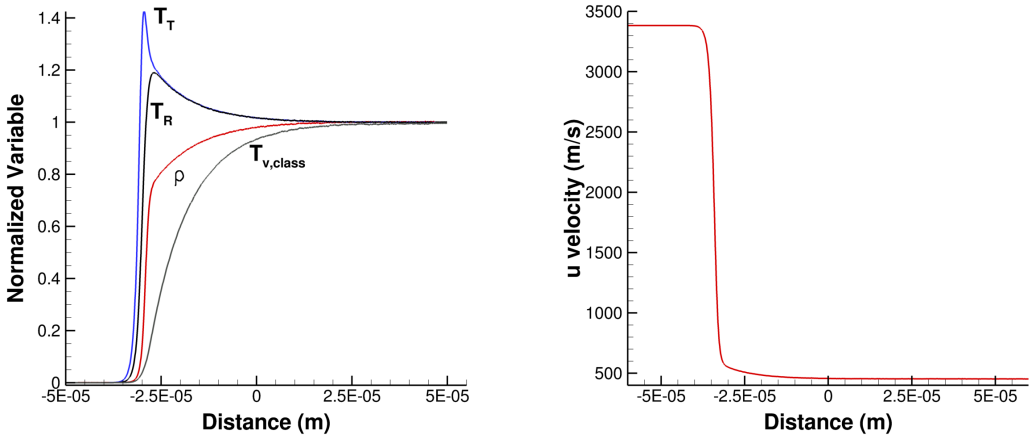

(a) Average shock profile at 40,000 steps

(b) Average u shock profile

Figure 5.19: $M_1 = 10$ shock with classical boundary conditions

Quantum Boundary Conditions

In this case the boundary conditions and vibrational sampling are inconsistent with the gas being simulated. However, these boundary conditions are representative of a realistic 1D nitrogen shock wave (not including chemical reactions). The normalized density profile at different times is shown in Fig. 5.20. As shown in Fig. 5.20(b), the shock is slowly moving upstream.

The temperature profiles in the shock are shown in Fig. 5.21. In the upstream region, we see that the classical vibrational temperature ($T_{v,class}$) is about $\theta_v/2$ ($\sim$1700 K), which is equivalent to the zero point vibrational energy. Because the transfer of

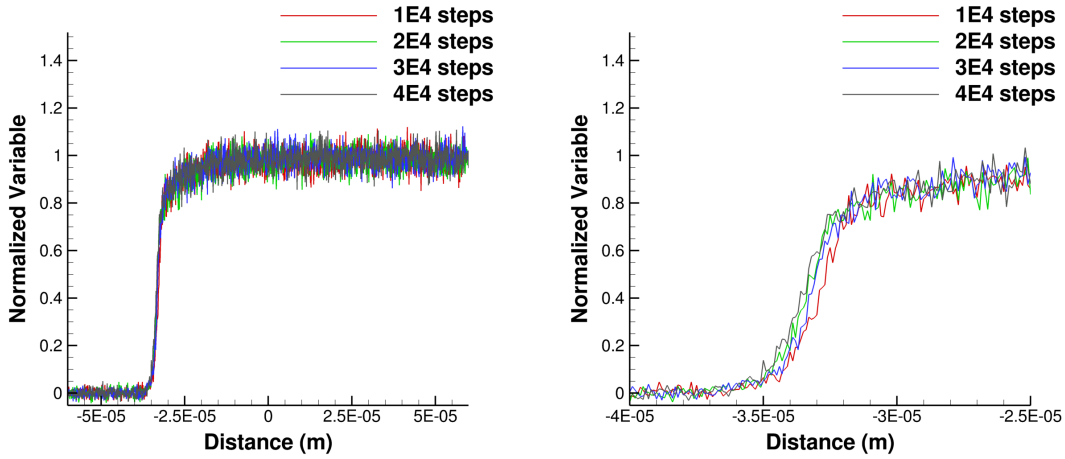

(a) Normalized density profile

(b) Normalized density profile, zoomed

Figure 5.20: Drifting $M_1 = 10$ shock with quantum boundary conditions at different times

vibration to other modes is relatively slow, the vibrational temperature remains constant upstream of the shock. However, if the upstream region was very long, vibration would equilibrate with other modes and heat up the upstream flow. The quantum vibrational temperature in the upstream region is slightly higher than the desired value (300 K) because the rovibrational energy coupling causes the actual vibrational energy to be slightly higher ($\sim$ 3 K) than the initialized vibrational energy (which is $\theta_v/2$), which is exacerbated by the steep slope in $T(\langle E_v \rangle)$ (see Fig.5.18). In the downstream region, we see that the translational, rotational, and classical vibrational temperatures do not equilibrate to the imposed translational temperature at the outflow boundary. This is significant because it shows that the shock will not conform to boundary conditions inconsistent with the thermodynamic properties of the gas of which it is composed. Additionally, we see that the classical and quantum vibrational temperatures are not in agreement in the downstream region. This is unavoidable because the definitions of these temperatures are different, but this difference will diminish at higher temperatures.

The u velocity profile in the shock is shown in Fig. 5.22, where it is seen that there is a slight decrease in the u velocity profile at the outflow, which explains the upstream

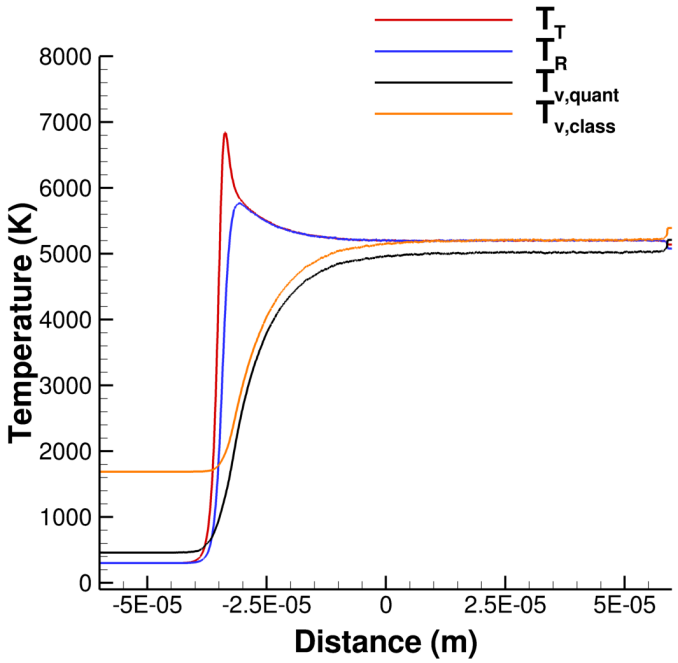

Figure 5.21: Temperature profiles in $M_1 = 10$ shock with quantum boundary conditions

movement of the shock.

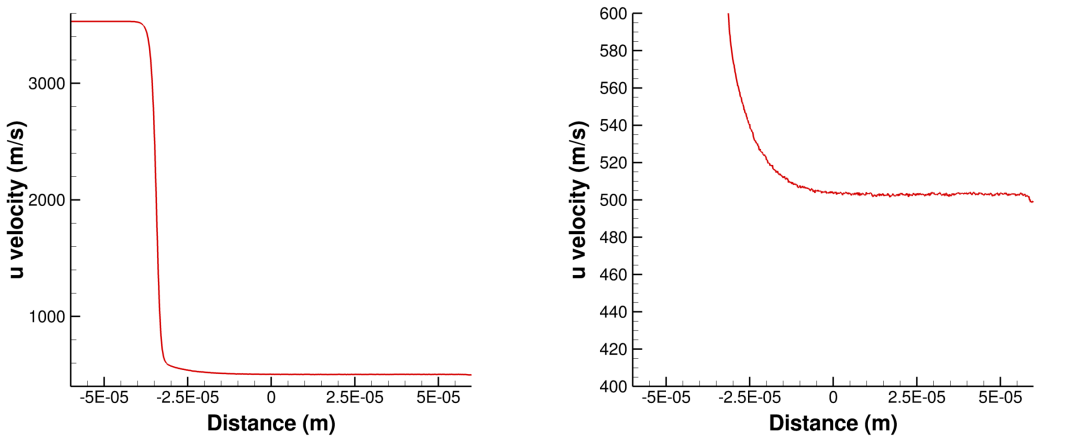

(a) time averaged u velocity profile

(b) Time averaged u velocity profile, zoomed

Figure 5.22: $M_1 = 10$ shock with quantum boundary conditions

Quantum Boundary Conditions with Classical Modifications

To prevent the shock from drifting, we modify the downstream flow conditions to account for the fact that the gas being simulated is classical. The upstream flow boundary conditions are kept at the quantum values given in Table 5.4, and vibrational energy of molecules is still sampled from the quantum distribution (Eq. 5.55). However, when computing the downstream conditions from the jump equations (Eqs. 5.50-5.52), the downstream enthalpy is defined using the classical definition ($h_2 = 9/2\ k_B T$). Additionally, because the downstream vibrational temperature should be in equilibrium with the other modes, the vibrational energy of molecules at the outflow are sampled from the classical distribution in Eq. 5.27. The downstream flow variables with these modifications are given in Table 5.5. The quantum boundary conditions with classical modifications are much closer to the quantum boundary conditions than the classical boundary conditions. There is still some difference in the downstream flow variables, but this is unavoidable. A CTC-DSMC simulation of a shock with these modified boundary conditions verified that the modifications stopped shock drift, and eliminated the jumps in T_t, ρ, and u seen at the outflow with the quantum boundary conditions. The density,

flow velocity, and flow temperatures of this shock are shown in Fig. 5.23.

	Classical BCs	Quantum BCs	Quantum BCs with classical modifications
u_1 (m/s)	3383.5	3530.7	3530.7
ρ_1 (kg/m^3)	0.1	0.1	0.1
T_1 (K)	300	300	300
u_2 (m/s)	452.5	499.1	503.65
ρ_2 (kg/m^3)	0.748	0.707	0.701
T_2 (K)	4509.0	5140.4	5179.4

Table 5.5: Comparison of different boundary conditions (BCs)

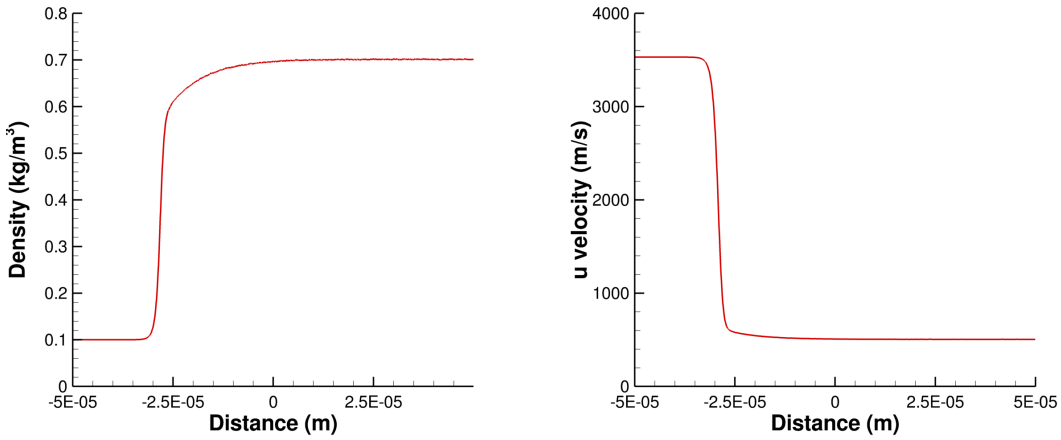

(a) Density profile

(b) u velocity

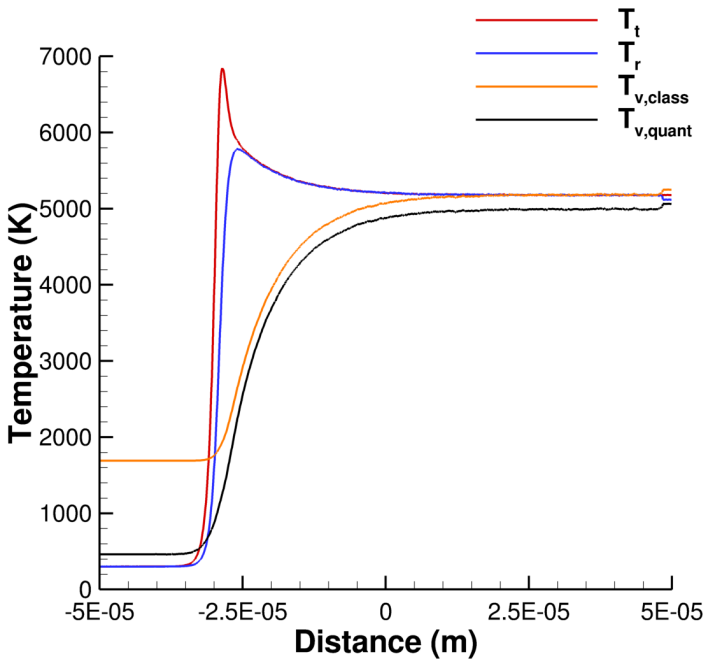

(c) T_t, T_r, $\mathrm{T}_{v,class}$, $\mathrm{T}_{v,quant}$ profiles

Figure 5.23: Time averaged profiles for the $M_1 = 10$, shock with quantum boundary conditions with classical modifications

5.7 Conclusions

In this chapter a Classical Trajectory Calculation Direct Simulation Monte Carlo (CTC-DSMC) implementation was described. This implementation uses the no-time-counter scheme with a cross-section determined by the potential energy surface, as opposed to a phenomenological collision rate model such as the variable hard-sphere (VHS) model. Both a constant cross-section model and a variable cross-section model were verified to produce identical CTC-DSMC results as long as the cross-section was conservative, thereby enabling the PES to dictate the collision rate. CTC-DSMC solutions for translational and rotational relaxation in one-dimensional shock waves (argon and diatomic nitrogen) were compared directly to pure Molecular Dynamics simulations employing an identical PES. For all cases, exact agreement was demonstrated down to the level of the velocity and rotational energy distribution functions. CTC-DSMC simulations are many orders of magnitude faster than pure MD because CTC-DSMC operates on spatial and temporal scales of the mean-free-path and mean-collision-time, respectively, and simulates only a fraction of real atoms contained within the flow volume.

For the diatomic nitrogen shock wave, long-lived orbiting collisions were found to occur within the simulations that persisted for more than a mean-collision-time (a DSMC time step). The trajectories show that in such collisions, the translational energy of two colliding nitrogen molecules is partially converted to rotational energy, reducing the translational energy below the value needed to escape the potential well. The two molecules exist in this meta-stable state until the complex exchange between rotational and translational energy allows the molecules to gain enough translational energy to escape the potential well and complete the collision event. For the diatomic nitrogen shock considered, such collisions only accounted for approximately 0.25% of all collisions. In this case, accurate results were obtained by ignoring these long-lived collisions. However, such physics are important for modeling multi-body collision rates and therefore recombination reactions, as well as having algorithm implications for the CTC-DSMC method.

We presented a preliminary algorithm for determining the three body collision rate in CTC-DSMC simulations for particles with no interatomic potential. We found that the three body collision rate predicted by CTC-DSMC and MD were in exact agreement

for this case. A discussion of the additional modifications to this algorithm that will be needed when considering three body collisions of particles interacting with a non-zero interatomic potential was presented. Ultimately, the three body collision rate in CTC-DSMC simulations can be compared to MD simulations with the same interatomic potential to evaluate the accuracy of any modifications.

A parallelization scheme for CTC-DSMC using a heterogeneous CPU/GPU system was described and benchmarked for certain test cases. The CTC-DSMC algorithm was threaded on multi-core CPUs using OpenMP and on GPUs using CUDA. The most important consideration for the parallelization scheme involved the effects of code branching due to the naturally varying collision times experienced by simulation molecules. If not addressed, such code branching was found to significantly decrease the GPU computational performance. A simple algorithm was presented that assigns multiple collisions to each thread, which, after computing a given collision, used a block-wise shared variable to determine the next collision available in memory to be performed. Using this algorithm, the GPU enabled speedup for a general flow problem approached the ideal speedup of a nominal case where all collisions require precisely the same time cost. We obtained a maximum speedup of $\sim$140$\times$ for a diatomic nitrogen shock containing 4×10^6 particles on a system with 4 GPUs+CPU compared with a serial simulation on one CPU core. The speedup per GPU was dependent on the number of collisions computed per GPU per CTC-DSMC step and ranged from 38$\times$ ($\sim$880,000 collisions) to 22$\times$ ($\sim$55,000 collisions). A speedup of $\sim$30$\times$ per GPU was obtained as long as there were $>\sim$100,000 collisions per GPU per CTC-DSMC time step. This parallelization technique has the potential to scale to larger CPU/GPU clusters with the use of standard DSMC distributed memory domain decomposition (via MPI) and the performance is expected to scale with the number of GPUs in the cluster. On existing parallel computing clusters, CTC-DSMC solutions of large-scale 2D and 3D non-equilibrium flows over complex geometries should be possible.

Finally, we discussed some of the issues occurring when simulating rotating, vibrating molecules with CTC-DSMC. At low temperatures, quantum and classical mechanics predict differing amounts of energy in the vibration mode, which led to problems simulating 1D shocks. Specifically, we found that 1D shocks simulated with classical

trajectory calculations would not conform to quantum mechanics based boundary conditions. We presented a simple method to adjust the downstream boundary conditions so that the quantum boundary conditions were closely approximated. Further work in this area could address how quasiclassical trajectory calculations, which involve using a post collision binning scheme to force molecules to vibrational and rotational energy levels allowed by quantum mechanics, can be used to better model molecular vibration in trajectory calculation DSMC. At higher temperatures, we found that rovibrational coupling caused an increase in the amount of energy stored in the rotational and vibrational modes. We demonstrated how this effect could be characterized so that the vibrational and rotational temperature could be correctly sampled.

Future effort is required to verify that CTC-DSMC is purely an acceleration technique for Molecular Dynamics simulations of dilute gases including long-lived collisions, multi-body collisions, and chemically reacting flows such as dissociation and recombination. Also, more accurate potential energy surfaces and trajectory integration techniques (quasi-classical or semi-classical trajectory integration) must be incorporated into the method to describe quantized vibrational excitation and relaxation. If successful, the CTC-DSMC method would directly link the field of computational chemistry (integrating the motion of small systems of atoms on a PES) with macroscopic dilute gas flows that are experimentally accessible and useful for engineering design.

Chapter 6

Summary and Conclusions

6.1 Summary

The primary goal of this work was to create a gas-surface chemical rate model to describe the heterogeneous recombination of oxygen on silica. To create this rate model, the first step was to determine the structures on silica surfaces where recombination could occur. This was outlined in Chapter 3. There is little information in the literature about the structures occurring on silica surfaces exposed to atomic oxygen. Therefore, we used molecular dynamics simulations with the $\text{ReaxFF}^{\text{GSI}}_{\text{SiO}}$ potential to model this system. The $\text{ReaxFF}^{\text{GSI}}_{\text{SiO}}$ potential is a classical potential which was specifically parametrized with highly accurate Density Function Theory results[3] to model gas-surface interactions in oxygen-silica systems. We validated that this potential was able to accurately describe the bulk structure of quartz and amorphous silica, as well as experimentally characterized surface reconstructions on quartz. We used molecular dynamics simulations with a flux boundary condition, wherein a silica surface was exposed to a gas composed of atomic oxygen until it reached steady-state surface population, to model the gas surface interface at different temperatures and pressures. The structures occurring on both quartz and amorphous silica surfaces exposed to atomic oxygen were analyzed to determine which surface sites were potentially catalytic with respect to direct gas-phase recombination reactions. We found that the majority of silica surfaces were covered with strongly bound bridging oxygen atoms, which were determined to be non-catalytic. We also identified a small set of surface structures (or defects), including

an under-coordinated silicon defect, a non-bridging oxygen defect, and a peroxyl defect which could participate direct gas-phase recombination reactions. These defects have been experimentally identified on real silica surfaces, and DFT calculations verified that the $\text{ReaxFF}^{\text{GSI}}_{\text{SiO}}$ adequately described the structure and energetics of these defects.[3, 1] Therefore, our simulations indicated that these defects were present on realistic silica surfaces exposed to atomic oxygen, and that they could be used in further studying oxygen recombination on silica.

The set of defects identified in Chapter 3 served as a basis for the finite rate catalytic model in Chapter 4. Such a rate model can be incorporated into continuum level simulations of hypersonic flows to describe gas-surface chemical reactions. The rate model consisted of a set of elementary gas-surface reactions based on the interaction of atomic and molecular oxygen with the defects discussed above. The rate equations used an Arrhenius form, which requires a pre-exponential factor and activation energy for each reaction. To find the Arrhenius parameters for the forward reactions we used trajectory calculations with the $\text{ReaxFF}^{\text{GSI}}_{\text{SiO}}$ potential. The outcomes of many trajectory calculations were used to find the probability of a reaction at different temperatures, which was fit using an exponential form to find Arrhenius parameters. The pre-exponential factors of reverse reactions were found using a combination of detailed balance and reasonable estimates from transition state theory. Values for the pre-exponential factors were picked from within a reasonable range for two reactions, and detailed balance was used to find the remaining reverse rate constants. This ensured that the rate model could maintain O_2-O gas-phase equilibrium. The activation energies of reverse reactions were calculated based on DFT single point energies because the $\text{ReaxFF}^{\text{GSI}}_{\text{SiO}}$ potential did not accurately predict the energy change for all of the reactions. The final rate model was used to predict the total oxygen recombination coefficient at different temperatures, pressures, and gas phase compositions.

We found that a rate model (as opposed to a simple constant or temperature dependent recombination coefficient) was necessary to generally describe gas-surface reactions. The recombination coefficient predicted by the rate model was a result of many competing reactions, and varied with temperature and pressure. The magnitude of the predicted recombination coefficient was directly proportional to the total concentration of surface sites, which is an input into the rate model. The recombination coefficient

predicted by the finite rate catalytic model was relatively constant at $T < 1500$ K, and decreased at T > 1500 K. The most important recombination reaction was the ER Recombination II reaction, wherein an atomic oxygen combined with the terminal oxygen atom in a peroxyl defect. Trajectory calculations showed that this reaction is essentially non-activated, which is why the oxygen recombination coefficient remained constant at T < 1500 K. The dropoff in the recombination coefficient at T > 1500 K was due to the desorption of molecular oxygen.

The secondary goal of this work was to use trajectory calculations, similar to those carried out in gas-surface interaction calculations, to model collisions in dilute gases with Classical Trajectory Calculation Direct Simulation Monte Carlo (CTC-DSMC). This was described in Chapter 5. We demonstrated a CTC-DSMC implementation that used the no-time-counter scheme with a cross-section determined by the potential energy surface. CTC-DSMC solutions for translational and rotational relaxation in one-dimensional shock waves (argon and diatomic nitrogen) were compared directly to pure Molecular Dynamics (MD) simulations employing an identical potential energy surface. For all cases, exact agreement was demonstrated down to the level of the velocity and rotational energy distribution functions. CTC-DSMC simulations are many orders of magnitude faster than pure MD because CTC-DSMC operates on spatial and temporal scales of the mean-free-path and mean-collision-time, respectively, and simulates only a fraction of real atoms contained within the flow volume. We also discussed a number of topics important in CTC-DSMC simulations, including GPU enabled acceleration, a preliminary algorithm for modeling three-body collisions, and characterizing high temperature rovibrational effects.

6.2 Conclusions and Future Work

In this work we developed a methodology for creating a finite rate catalytic model based on first principals calculations. We were successful in demonstrating a rate model that described the recombination of oxygen on realistic silica surfaces. Our rate model agreed with the trends in experimental results at T 300-1000 K, where recombination coefficients remained constant with temperature. However, there is experimental evidence that the oxygen recombination coefficient increases exponentially with temperature at

$T > 1000$ K, which is not predicted by our rate model. It is thought that the experimentally observed exponential trend in γ_O is due to an activated ER recombination reaction[6, 37], with the trend in γ_O with T following the activation energy of the ER recombination reaction. Neither type of ER recombination reactions in our rate model confirm this hypothesis. Therefore, we conclude that the exponential trend in recombination coefficient at T > 1000 K is not due to an activated ER recombination type reaction, and must be due to something else. Further work in three areas is necessary for a complete description of oxygen recombination on silica surfaces.

First, the total concentration of surface sites ($[S]$) as a function of temperature, pressure and gas-phase composition on real silica surfaces must be determined. Both our rate model and experimental results[6], indicate that γ is directly proportional to $[S]$. Currently, we assume that $[S]$ is constant, and choose $[S]$ so that the recombination coefficient predicted the rate model matches experimental results. However, it is possible that the concentration of surface sites varies with temperature and pressure. With the flux boundary condition molecular dynamics simulations in Chapter 3, we were able to determine how the $[S]$ varied with temperature and pressure, although the pressures used in these simulations were much higher than those used experimentally. A Kinetic Monte Carlo method, such as the one demonstrated by Thömel et al.[146], could be useful to model the structure of a silica surface exposed at low pressures. However, it is noted that the total concentration of surface sites on realistic silica surfaces cannot be determined from atomistic simulations alone, because of their limited length scales. At best atomistic simulations could give the concentration of sites per unit surface area. Because realistic surfaces are not perfectly flat, but rather macroscopically rough, the concentration of sites per unit surface area must be multiplied by a roughness factor to find the actual concentration of surface sites per unit area.[6] Thus a complete model of the surface must rely on *in situ* surface roughness measured through experiment, for example by using BET isotherms[147]

Second, the trajectory calculations for gas surface interactions must account for non-adiabatic reaction dynamics. As discussed in Chapter 3, the potential energy surface for gas phase species interacting with a cluster representing a surface site can significantly vary depending on the electronic spin state of the system. The calculations presented in this work assume that the system always follows the lowest potential energy surface,

however it is possible that this is not the case. A better representation of non-adiabatic reaction dynamics could be realized by a scheme that allows hopping between electronic energy states, such as the Landau-Zener scheme.[148, 149] For determining the thermal accommodation coefficient, which ultimately determines the energy transferred to the surface by the reaction, it is especially important to model non-adiabatic reaction dynamics because it is possible that recombined oxygen molecules leave the surface in electronically excited states.

Third, more mechanisms need to be incorporated into the rate model. Our rate model only included direct gas-phase reactions, such as adsorption, ER Recombination, and O_2 formation. It is possible that additional recombination mechanisms, such as Langmuir-Hinschelwood (LH) mechanism contribute to recombination. It is thought that LH recombination between physisorbed oxygen atoms and chemisorbed oxygen atoms results in the mild maximum in recombination coefficients at low temperatures.[6, 14] The rate model presented here predicts relatively constant γ_O at low temperatures, and the addition of this mechamism would not significantly alter the trends in γ_O with T. At higher temperatures, it is possible that LH recombination between chemisorbed oxygen atoms contributes to the overall recombination coefficient. In a previous work we observed that non-bridging oxygen atoms on silica surfaces could diffuse through the surface via lattice diffusion.[108] There is experimental evidence that lattice diffusion of atomic oxygen occurs through bulk SiO_2[109], and there are computational works modeling this process.[110, 111] In our previous work we also found that diffusing non-bridging oxygen atoms could combine on the surface to form adsorbed O_2, which could eventually desorb to complete the recombination process. Further investigation of the diffusion and recombination of non-bridging oxygen atoms on silica surfaces with both molecular dynamics simulations and DFT is warranted. All three of the topics discussed above should be addressed to better describe oxygen-silica surface catalysis.

The CTC-DSMC simulations presented in Chapter 5 were adequate to describe simple one dimensional shocks composed of argon or nitrogen. With existing computational resources, this method should be applicable to full 3D flows with complex geometries. Future research in trajectory calculation DSMC should focus on improving the ability of this method to accurately model collisions involving vibrational excitation/relaxation

and chemical reactions, which are of interest in hypersonic flows. This can be accomplished by using realistic potential energy surfaces[150, 19, 20] as well as quasiclassical or semiclassical trajectory integration schemes.[130, 131] Trajectory calculation DSMC that can accurately describe chemical reactions and vibrational excitation/relaxation would be a useful tool in modeling hypersonic non-equilibrium flows and for developing new phenomenological or state-to-state based DSMC collision models.

References

[1] Norman, P., Schwartzentruber, T., Leverentz, H., Luo, S., Meana-Pañeda, R., Paukku, Y., and Truhlar, D. G., "The Structure of Silica Surfaces Exposed to Atomic Oxygen," *Journal of Physical Chemistry C*, Vol. 117, No. 18, 2013, pp. 9311–9321.

[2] Meana-Pañeda, R., Paukku, Y., and Truhlar, D. G., "Private Communication," May 25, 2013.

[3] Kulkarni, A., Truhlar, D. G., Goverapet Srinivasan, S., van Duin, A., Norman, P., and Schwartzentruber, T., "Oxygen Interactions with Silica Surfaces: Coupled Cluster and Density Functional Investigation and the Development of a New ReaxFF Potential," *Journal of Physical Chemistry C*, 2012.

[4] Susman, S., Volin, K., Montague, D., and Price, D., "Temperature Dependence of the First Sharp Diffraction Peak in Vitreous Silica," *Physical Review B*, Vol. 43, No. 13, 1991, pp. 11076.

[5] Balat-Pichelin, M., Badie, J., Berjoan, R., and Boubert, P., "Recombination coefficient of atomic oxygen on ceramic materials under earth re-entry conditions by optical emission spectroscopy," *Chemical physics*, Vol. 291, No. 2, 2003, pp. 181–194.

[6] Kim, Y. C. and Boudart, M., "Recombination of oxygen, nitrogen, and hydrogen atoms on silica: kinetics and mechanism," *Langmuir*, Vol. 7, No. 12, 1991, pp. 2999–3005.

[7] Marschall, J., "Experimental determination of oxygen and nitrogen recombination coefficients at elevated temperatures using laser-induced fluorescence," 1997 National Heat Transfer Conference, Baltimore, MD, 1997, AIAA-1997-3879.

[8] Barbato, M., Reggiani, S., Bruno, C., and Muylaert, J., "Model for Heterogeneous Catalysis on Metal Surfaces with Applications to Hypersonic Flows," *Journal of Thermophysics and Heat Transfer*, Vol. 14, No. 3, 2000, pp. 412–420.

[9] Bose, D., Wright, M., and Palmer, G., "Uncertainty Analysis of Laminar Aeroheating Predictions for Mars Entries," *Journal Thermophysics and Heat Tranfer*, Vol. 20, No. 4, 2006, pp. 652–662.

[10] Cozmuta, I., "Molecular Mechanisms of Gas Surface Interactions in Hypersonic Flows," 39th AIAA Thermophysics Conference, Miami, FL, 2007, AIAA-2007-4046.

[11] Alfano, D., Scatteia, L., Monteverde, F., Beche, E., and Balat, M., "Microstructural Characterization of ZrB2-SiC based UHTC Tested in the MESOX Plasma Facility," *Journal of the European Ceramic Society*, Vol. 30, 2010, pp. 2345–2355.

[12] Greaves, J. C. and Linnet, J. W., "The Recombination of Oxygen Atoms At Surfaces," *Transactions of the Faraday Society*, 1958.

[13] Jumper, J. E. and Seward, W. A., "Model for Oxygen Recombination on Reaction Cured Glass," *Journal of Thermophysics and Heat Transfer*, Vol. 8, No. 3, 1994, pp. 460–465.

[14] Macko, P., Veis, P., and Cernogora, G., "Study of oxygen atom recombination on a Pyrex surface at different wall temperatures by means of time-resolved actinometry in a double pulse discharge technique," *Plasma Sources Science and Technology*, Vol. 13, No. 2, 2004, pp. 251.

[15] Bedra, L. and Balat-Pichelin, M. J., "Comparative modeling study and experimental results of atomic oxygen recombination on silica-based surfaces at high temperature," *Aerospace Science and Technology*, Vol. 9, No. 4, 2005, pp. 318–328.

[16] Bird, G. A., *Molecular Gas Dynamics and the Direct Simulation of Gas Flows*, Oxford University Press, Oxford, UK, 1994.

[17] Kim, J. G. and Boyd, I. D., "State Resolved Thermochemical Modeling of Nitrogen Using DSMC," 43rd AIAA Thermophysics Converence, New Orleans, LA, 2012, AIAA-2012-2991.

[18] Kim, J. G. and Boyd, I. D., "Master Equation Study of Hydrogen Relaxation Using Complete Sets of State-to-state transition Rates," 50th AIAA Aerospace Sciences Meeting, Nashville, TN, 2012, AIAA-2012-0362.

[19] Jaffe, R., Schwenke, D. W., and Chaban, G., "Vibrational and Rotational Excitation and Relaxation of Nitrogen from Accurate Theoretical Calculations," 46th AIAA Aerospace Sciences Meeting and Exhibit, Reno, NV, 2008, AIAA-2008-1208.

[20] Jaffe, R., Schwenke, D. W., and Chaban, G., "Theoretical Analysis of N_2 collisional dissociation and rotation-vibration energy transfer," 47th AIAA Thermophysics Converence, Orlando, FL, 2009, AIAA-2009-1569.

[21] Stenfeld, J. I., Francisco, J. S., and Hase, W. L., *Chemical Kinetics and Dynamics*, Prentence Hall, Upper Saddle River, NJ, 1999.

[22] Koura, K., "Monte Carlo direct simulation of rotational relaxation of diatomic molecules using classical trajectory calculations: Nitrogen shock wave," *Physics of Fluids*, Vol. 9, No. 11, 1997, pp. 3543–3549.

[23] Bruno, D., Capitelli, M., Longo, S., and Minelli, P., "Direct Simulation Monte Carlo Modeling of Non Equilibrium Reacting Flows. Issues for the Inclusion into a ab initio Molecular Processes Simulator," *ICCSA (2)*, edited by A. Lagan, M. L. Gavrilova, V. Kumar, Y. Mun, C. J. K. Tan, and O. Gervasi, Vol. 3044 of *Lecture Notes in Computer Science*, Springer, 2004, pp. 383–391.

[24] Greaves, J. and Linnett, J., "Recombination of atoms at surfaces. Part 6.Recombination of oxygen atoms on silica from 20 C to 600 C," *Transactions of the Faraday Society*, Vol. 55, 1959, pp. 1355–1361.

[25] Carleton, K. and Marinelli, W., "Spacecraft thermal energy accommodation from atomic recombination," *Journal Thermophysics and Heat Transfer*, Vol. 6, 1992, pp. 650–655.

[26] Stewart, D., "Determination of Surface Catalytic Efficiency for Thermal Protection Materials: Room Temperature to Their Upper Use Limit," 31rst Thermophysics Conference, New Orleans, LA, 1996, AIAA-1996-1863.

[27] Gomez, S., Steen, P., and Graham, W., "Atomic oxygen surface loss coefficient measurements in a capacitive/inductive radio-frequency plasma," *Applied Physics Letters*, Vol. 81, No. 1, 2002, pp. 19–21.

[28] Chazot, O., Panerai, F., Muylaert, J.-M., and Thoemel, J., "Catalysis Phenomena Determination in Plasmatron Facility for Flight Experiment Design," 10th AIAA/ASME Joint Thermophysics and Heat Transfer Conference, Chicago, IL, 2010, AIAA-2010-1248.

[29] Suzuki, S., Mizuno, M., Takayanagi, H., Fujita, K., Matsue, M., and Yamagiwa, Y., "Experiment Study for Atomic Oxygen Catalytic Efficiency on TPS Surfaces using Microwave Discharged Plasma," 51rst AIAA Aerospace Sciences Meeting, Grapevine, TX, 2013, AIAA-2013-0742.

[30] Alfano, D., Scatteia, L., Cantoni, S., and Balat-Pichelin, M., "Emissivity and catalycity measurements on SiC-coated carbon fibre reinforced silicon carbide composite," *Journal of the European Ceramic Society*, Vol. 29, No. 10, 2009, pp. 2045–2051.

[31] Pejaković, D. A., Marschall, J., Duan, L., and Martin, M. P., "Nitric oxide production from surface recombination of oxygen and nitrogen atoms," *Journal of Thermophysics and Heat Transfer*, Vol. 22, No. 2, 2008, pp. 178–186.

[32] Cartry, G., Duten, X., and Rousseau, A., "Atomic oxygen surface loss probability on silica in microwave plasmas studied by a pulsed induced fluorescence technique," *Plasma Sources Science and Technology*, Vol. 15, No. 3, 2006, pp. 479.

[33] Sneh, O. and George, S. M., "Thermal stability of hydroxyl groups on a well-defined silica surface," *The Journal of Physical Chemistry*, Vol. 99, No. 13, 1995, pp. 4639–4647.

[34] Nawaz, A., Driver, D. M., and Salinas, I. T., "Influence of Catalysis and Oxidation on Stagnation Point Heat Flux Measurements in Arc Jets," 2013, NATO Report: STO-MP-AVT-199.

[35] Balat-Pichelin, M. J., Kovalev, V., Kolesnikov, A., and Krupnov, A., "An Analysis and Predicting the Efficiency of Atomic Oxygen Recombination and Chemical Energy Accommodation on Heated Silica Surfaces," *Rarefied Gas Dynamics: 25th International Symposium*, AIP, 2005, pp. 1347–1352.

[36] Fernández-Ramos, A., Miller, J. A., Klippenstein, S. J., and Truhlar, D. G., "Modeling the Kinetics of Bimolecular Reactions," *Chemical Reviews*, Vol. 106, No. 11, 2006, pp. 4518–4584.

[37] Guerra, V., "Analytical model of heterogeneous atomic recombination on silicalike surfaces," *Plasma Science, IEEE Transactions on*, Vol. 35, No. 5, 2007, pp. 1397–1412.

[38] Scatteia, L., Alfano, D., Monteverde, F., Sans, J.-L., and Balat-Pichelin, M., "Effect of the Machining Method on the Catalycity and Emissivity of ZrB2 and ZrB2–HfB2-Based Ceramics," *Journal of the American Ceramic Society*, Vol. 91, No. 5, 2008, pp. 1461–1468.

[39] Cacciatore, M., Rutigliano, M., and Billing, G. D., "Eley-Rideal and Langmuir-Hinshelwood recombination coefficients for oxygen on silica surfaces," *Journal of Thermophysics and Heat Transfer*, Vol. 13, No. 2, 1999, pp. 195–203.

[40] Rutigliano, M., Zazza, C., Sanna, N., Pieretti, A., Mancini, G., Barone, V., and Cacciatore, M., "Oxygen Adsorption on β-Cristobalite Polymorph: Ab Initio Modeling and Semiclassical Time-Dependent Dynamics," *The Journal of Physical Chemistry A*, Vol. 113, No. 52, 2009, pp. 15366–15375.

[41] Arasa, C., Gamallo, P., and Sayós, R., "Adsorption of atomic oxygen and nitrogen at β-Cristobalite (100): a density functional theory study," *The Journal of Physical Chemistry B*, Vol. 109, No. 31, 2005, pp. 14954–14964.

[42] Arasa, C., Busnengo, H., Salin, A., and Sayós, R., "Classical dynamics study of atomic oxygen sticking on the β-cristobalite (100) surface," *Surface Science*, Vol. 602, No. 4, 2008, pp. 975–985.

[43] Arasa, C., Morón, V., Busnengo, H., and Sayós, R., "Eley–Rideal reaction dynamics between O atoms on β-cristobalite (100) surface: A new interpolated potential energy surface and classical trajectory study," *Surface Science*, Vol. 603, No. 17, 2009, pp. 2742–2751.

[44] Morón, V., Gamallo, P., Martin-Gondre, L., Crespos, C., Larregaray, P., and Sayós, R., "Recombination and Chemical Energy Accommodation Coefficients From Chemical Dynamics Simulations: O/O2 Mixtures Reacting over a β-Cristobalite (001) Surface," *Physical Chemistry Chemical Physics*, Vol. 13, No. 39, 2011, pp. 17494–17504.

[45] Bedra, L., Rutigliano, M., Balat-Pichelin, M., and Cacciatore, M., "Atomic oxygen recombination on quartz at high temperature: experiments and molecular dynamics simulation," *Langmuir*, Vol. 22, No. 17, 2006, pp. 7208–7216.

[46] Zazza, C., Rutigliano, M., Sanna, N., Barone, V., and Cacciatore, M., "Oxygen Adsorption on β-Quartz Model Surfaces: Some Insights from Density Functional Theory Calculations and Semiclassical Time-Dependent Dynamics," *The Journal of Physical Chemistry A*, Vol. 116, No. 9, 2012, pp. 1975–1983.

[47] Kohn, W., Becke, A. D., and Parr, R. G., "Density Functional Theory of Electronic Structure," *Journal of Physical Chemistry.*, Vol. 100, No. 31, 1996, pp. 12974–12980.

[48] Lopes, P., Demchuk, E., and Mackerell, A., "Reconstruction of the (011) Surface on α-Quartz: A Semiclassical Ab Initio Molecular Dynamics Study," *Interntional Journal of Quantum Chemistry*, Vol. 109, No. 1, 2008, pp. 50–64.

[49] Chen, Y.-W., Cao, C., and Cheng, H.-P., "Finding Stable α-Quartz Surface Structures via Simulations," *Applied Physics Letters*, Vol. 93, 2008, pp. 181911.

[50] Rignanese, G.-M., Vita, A. D., Charlier, J.-C., Gonze, X., and Car, R., "First-Principles Molecular Dynamics Study of the (0001) α-Quartz Surface," *Physical Review B*, Vol. 61, No. 19, 2000, pp. 13250–13255.

[51] Bart, F. and Gautier, M., "A LEED study of the (0001) a-Quartz Surface Reconstruction," *Surface Science*, Vol. 311, No. 1, 1994, pp. L671–L676.

[52] Steurer, W., Apfolter, A., Koch, M., Sarlate, T., Sodergard, E., Ernst, W., and Holts, B., "The Structure of the α-Quartz(0001) Surface Investigated Using Helium Atom Scattering and Atomic Force Microscopy," *Surface Science*, Vol. 601, 2007, pp. 4407–4411.

[53] Huang, P. Y., Kurasch, S., Srivastava, A., Skakalova, V., Kotakoski, J., Krasheninnikov, A. V., Hovden, R., Mao, Q., Meyer, J. C., Smet, J., Muller, D. A., and Kaiser, U., "Direct Imaging of a Two-Dimensional Silica Glass on Graphene," *Nano Letters*, Vol. 12, No. 2, 2012, pp. 1081–1086.

[54] Legrand, A. P., *The Surface Properties of Silicas*, John Wiley and Sons, New York, NY, 1998, Chap. 5.

[55] Lieberman, M. A. and Lictenberg, A. J., *Principles of Plasma Discharges and Material Processing*, John Wiley and Sons, New York, NY, 1994, Chap. 1.

[56] Zhuravlev, L., "The Surface Chemistry of Amorphous Silica. Zhuravlev model," *Colloids and Surfaces A*, Vol. 173, No. 1, 2000, pp. 1–38.

[57] Plimpton, S. J., "Fast Parallel Algorithms for Short-Range Molecular Dynamics," *Journal of Computational Physics*, Vol. 117, No. 1, 1995, pp. 1–19, http://lammps.sandia.gov.

[58] Sanders, M., Leslie, M., and Catlow, C., "Interatomic potentials for SiO2," *Journal of the Chemical Society, Chemical Communications*, , No. 19, 1984, pp. 1271–1273.

[59] Tsuneyuki, S., Tsukada, M., Aoki, H., and Matsui, Y., "First-principles interatomic potential of silica applied to molecular dynamics," *Physical Review Letters*, Vol. 61, No. 7, 1988, pp. 869–872.

[60] Van Beest, B., Kramer, G., and Van Santen, R., "Force fields for Silicas and Aluminophosphates based on Ab Initio Calculations," *Physical Review Letters*, Vol. 64, No. 16, 1990, pp. 1955–1958.

[61] de Vos Burchart, E., Verheij, V., Van Bekkum, H., and Van de Graaf, B., "A consistent molecular mechanics force field for all-silica zeolites," *Zeolites*, Vol. 12, No. 2, 1992, pp. 183–189.

[62] Roder, A., Kob, W., and Binder, K., "Structure and Dynamics of Amorphous Silica Surfaces," *Journal of Chemical Physics*, Vol. 114, No. 17, 2001, pp. 7602–7614.

[63] Van Duin, A. C., Dasgupta, S., Lorant, F., and Goddard, W. A., "ReaxFF: a reactive force field for hydrocarbons," *The Journal of Physical Chemistry A*, Vol. 105, No. 41, 2001, pp. 9396–9409.

[64] Mortier, W. J., Ghosh, S. K., and Shankar, S., "Electronegativity-equalization method for the calculation of atomic charges in molecules," *Journal of the American Chemical Society*, Vol. 108, No. 15, 1986, pp. 4315–4320.

[65] van Duin, A. C. T., Strachan, A., Stewman, S., Zhang, Q., and Goddard-III, W. A., "$\text{ReaxFF}_{\text{SiO}}$ Reactive Force Field for Silicon and Silicon Oxide Systems," *Journal of Physical Chemistry. A*, Vol. 107, 2003, pp. 2802–3811.

[66] Valentini, P., Schwartzentruber, T. E., and Cozmuta, I., "Molecular dynamics simulation of O sticking on Pt (111) using the ab initio based ReaxFF reactive force field," *The Journal of Chemical Physics*, Vol. 133, 2010, pp. 084703.

[67] Khalilov, U., Pourtois, G., Duin, A. v., and Neyts, E., "self-limiting oxidation in small-diameter Si nanowires," *Chemistry of Materials*, Vol. 24, No. 11, 2012, pp. 2141–2147.

[68] Neyts, E., Khalilov, U., Pourtois, G., and Van Duin, A., "Hyperthermal oxygen interacting with silicon surfaces: adsorption, implantation, and damage creation," *The Journal of Physical Chemistry C*, Vol. 115, No. 11, 2011, pp. 4818–4823.

[69] Khalilov, U., Pourtois, G., van Duin, A., and Neyts, E., "Hyperthermal Oxidation of Si (100) 2× 1 Surfaces: Effect of Growth Temperature," *The Journal of Physical Chemistry C*, Vol. 116, No. 15, 2012, pp. 8649–8656.

[70] Watts, J. D., Gauss, J., and Bartlett, R. J., "Coupled-Cluster Methods with Noniterative Triple Excitations for Restricted Open-Shell Hartree–Fock and Other General Single Determinant Reference Functions. Energies and Analytical Gradients," *Journal of Chemical Physics*, Vol. 98, 1993, pp. 8718–8733.

[71] Knowles, P. J., Hampel, C., and Werner, H.-J., "Coupled Cluster Theory For High Spin, Open Shell Reference Wave Functions," *Journal of Chemical Physics*, Vol. 99, 5219–5227; **2000**, *112*, 3106–3107(E), 1993.

[72] Zhao, Y. and Truhlar, D. G., "A New Local Density Functional For Main-Group Thermochemistry, Transition Metal Bonding, Thermochemical Kinetics, and Noncovalent Interactions," *Journal of Chemical Physics*, Vol. 125, 2006, pp. 194101.

[73] Zhao, Y. and Truhlar, D. G., "The M06 Suite of Density Functionals for Main Group Thermochemistry, Thermochemical Kinetics, Noncovalent Interactions, Excited States, and Transition Elements: Two New Functionals and Systematic Testing of Four M06-Class Functionals and 12 other Functionals," *Theoretical Chemistry Accounts*, Vol. 120, No. 1, 2008, pp. 215–241.

[74] Demuth, T., Jeavoine, Y., Hafner, J., and Angyan, J. G., "Polymorphism in Silica Studied in the Local Density and Generalized-Gradient Approximations," *Journal of Physics:Condensed Matter*, Vol. 11, 1999, pp. 3833–3874.

[75] Dolino, G., Bachheimer, J., and Zeyen, C., "Observation of an Intermediate Phase Near the α-β Transition of Quartz by Heat Capacity and Neutron Scattering Measurements," *Solid State Commun.*, Vol. 45, No. 3, 1983, pp. 295–299.

[76] Levien, L., Prewitt, C. T., and Weidner, D. J., "Structure and Elastic Properties of Quartz at Pressure," *American Minerologist*, Vol. 65, 1980, pp. 920–930.

[77] Kihara, K., "An X-ray Study of the Temperature Dependence of the Quartz Structure," *European Journal of Minerology*, Vol. 2, No. 1, 1990, pp. 63–77.

[78] Downs, R. and Hall-Wallace, M., "The American Mineralogist Crystal Structure Database," *Americal Minerologist*, Vol. 88, No. 1, 2003, pp. 247–250.

[79] Huff, N., Demiralp, E., Çagin, T., and Goddard III, W., "Factors Affecting Molecular Dynamics Simulated Vitreous Silica Structures," *Journal of Non-Crysalline Solids*, Vol. 253, No. 1, 1999, pp. 133–142.

[80] Nose, S. and Klein, M., "Constant Pressure Molecular Dynamics for Molecular Systems," *Molecular Physics*, Vol. 50, No. 5, 1983, pp. 1055–1076.

[81] Jee, S., McGaughey, A., and Sholl, D., "Molecular Simulations of Hydrogen and Methane Permeation Through Pore Mouth Modified Zeolite Membranes," *Molecular Simulation*, Vol. 35, No. 1-2, 2009, pp. 70–78.

[82] Vink, R. and Barkema, G., "Large Well-relaxed Models of Vitreous Silica, Coordination Numbers, and Entropy," *Physical Review B*, Vol. 67, No. 24, 2003, pp. 245201.

[83] Nakano, A., Kalia, R., and Vashishta, P., "First Sharp Diffraction Peak and Intermediate-Range Order in Amorphous Silica: Finite-Size Effects in Molecular Dynamics Simulations," *Journal of Non-Crystalline Solids*, Vol. 171, No. 2, 1994, pp. 157–163.

[84] Fogarty, J., Aktulga, H., Grama, A., Van Duin, A., and Pandit, S., "A Reactive Molecular Dynamics Simulation of the Silica-Water Interface," *Journal of Chemical Physics*, Vol. 132, 2010, pp. 174704.

[85] Grimley, D., Wright, A., and Sinclair, R., "Neutron Scattering from Vitreous Silica IV. Time-of-Flight Diffraction," *Journal of Non-Crystalline Solids*, Vol. 119, No. 1, 1990, pp. 49–64.

[86] Mozzi, R. and Warren, B., "The Structure of Vitreous Silica," *Journal of Applied Crystallography*, Vol. 2, No. 4, 1969, pp. 164–172.

[87] Konnert, J. and Karle, J., "The Computation of Radial Distribution Functions for Glassy Materials," *Acta Crystallogr., Sect. A: Cryst. Phys., Diffr., Theor. Gen. Crystallogr.*, Vol. 29, No. 6, 1973, pp. 702–710.

[88] Coombs, P., De Natale, J., Hood, P., McElfresh, D., Wortman, R., and Shackelford, J., "The Nature of the Si-O-Si Bond Angle Distribution in Vitreous Silica," *Philosophy Magazine B*, Vol. 51, No. 4, 1985, pp. 39–42.

[89] Neuefeind, J. and Liss, K., "Bond Angle Distribution in Amorphous Germania and Silica," *Berichte der Bunsengesellschaft Physical Chemistry*, Vol. 100, No. 8, 1996, pp. 1341–1349.

[90] Garcia, A. and Wagner, W., "Generation of the Maxwellian Inflow Distribution," *Journal of Computational Physics*, Vol. 217, No. 2, 2006, pp. 693–708.

[91] Hochstrasser, G. and Antonini, J., "Surface States of Pristine Silica Surfaces: I. ESR studies of Es Dangling Bonds and of CO2- Adsorbed Radicals," *Surface Science*, Vol. 32, No. 3, 1972, pp. 644–664.

[92] Warren, W., Kanicki, J., Rong, F., and Poindexter, E., "Paramagnetic Point Defects in Amorphous Silicon Dioxide and Amorphous Silicon Nitride Thin Films II." *Journal of the Electrochemical Society*, Vol. 139, No. 3, 1992, pp. 880–889.

[93] Costa, D., Fubini, B., Giamello, E., and Volante, M., "A Novel Type of Active Site at the Surface of Crystalline SiO2 (a-Quartz) and its Possible Impact on Pathogenicity," *Canadian Journal of Chemistry*, Vol. 69, No. 9, 1991, pp. 1427–1434.

[94] Levine, S. M. and Garofalini, S. H., "A Structural Analysis of the Vitreous Silica Surface via a Molecular Dynamics Computer Simulation," *Journal of Chemical Physics*, Vol. 86, No. 5, 1987, pp. 2997–3002.

[95] Wilson, M. and Walsh, T., "Hydrolysis of the Amorphous Silica Surface. I. Structure and Dynamics of the Dry Surface," *Journal of Chemical Physics*, Vol. 113, 2000, pp. 9180–9190.

[96] Griscom, D. L. and Friebele, E. J., "Fundamental Defect Centers in Glass: Si Hyperfine Structure of the Nonbridging Oxygen Hole Center and the Peroxyl Radical in a-SiO2," *Physical Review B*, Vol. 24, No. 8, Oct 1981, pp. 4896–4898.

[97] Lynch, B. J., Zhao, Y., and Truhlar, D. G., "Effectiveness of Diffuse Basis Functions for Calculating Relative Energies by Density Functional Theory," *Journal of Physical Chemistry A*, Vol. 107, No. 9, 2003, pp. 1384–1388.

[98] Valentini, P. and Schwartzentruber, T. E., "Large-scale molecular dynamics simulations of normal shock waves in dilute argon," *Physics of Fluids*, Vol. 21, No. 6, 2009, pp. 066101.

[99] Sorenson, C., Valentini, P., and Schwartzentruber, T. E., "Uncertainty Analysis of Reaction Rates in a Finite Rate Surface Catalysis Model," 42nd AIAA Thermophysics Conference, Honolulu, Hawaii, 2011, AIAA-2011-3643.

[100] Marschall, J. and MacLean, M., "Finite-Rate Surface Chemistry Model, I: Formulation and Reaction System Examples," 42nd AIAA Thermophysics Conference, Honolulu, HI, June, 2011, AIAA 2011-3738.

[101] MacLean, M., Marschall, J., and Driver, D., "Finite-Rate Surface Chemistry Model, II: Coupling to Viscous Navier-Stokes Code," 41rst AIAA Thermophysics Conference, Honolulu, HI, 2011, AIAA-2011-3784.

[102] Alkandry, H., Farbar, E. D., and Boyd, I. D., "Evaluation of Finite-Rate Surface Chemistry Models for Simulation of the Stardust Reentry Capsule," 43rd AIAA Thermophysics Conference, New Orleans, LA, 2012, AIAA 2012-2874.

[103] Vincenti, W. and Kruger, C., *Introduction to Physical Gas Dynamics*, Robert E. Kreiger Publishing Company, Malabar, Florida, 1965.

[104] Agresti, A. and Coull, B. A., "Approximate is better than exact for interval estimation of binomial proportions," *The American Statistician*, Vol. 52, No. 2, 1998, pp. 119–126.

[105] McQuarrie, D. A., *Statistical Mechanics*, University Science Books, Sausalito, California, 2000.

[106] McBride, B. J. and Gordon, S., "Computer Program for Calculation of Complex Chemical Equilibrium Compostions and Applications II," *NASA RP-1331-P2*, 1996.

[107] Stewart, D. A., "Surface Catalysis and Characterization of Proposed Candidate TPS for Access-to-Space Vehicles," *NASA Technical Memorandum 112206*, 1997.

[108] Norman, P., Schwarztentruber, T., and Cozmuta, I., "Modeling Air-SiO2 surface Catalysis under Hypersonic Conditions with ReaxFF Molecular Dynamics," 10th AIAA/ASME Joint Thermophysics and Heat Transfer Conference, Chicago, IL, 2010, AIAA-2010-4320.

[109] Tatsumura, K., Shimura, T., Mishima, E., Kawamura, K., Yamasaki, D., Yamamoto, H., Watanabe, T., Umeno, M., and Ohdomari, I., "Reactions and diffusion of atomic and molecular oxygen in the SiO_2 network," *Physical Review B*, Vol. 72, No. 4, 2005, pp. 045205.

[110] Hoshino, T., Hata, M., Neya, S., Nishioka, Y., Watanabe, T., Tatsumura, K., and Ohdomari, I., "Diffusion of molecular and atomic oxygen in silicon oxide," *Japanese journal of applied physics*, Vol. 42, No. 6A, 2003, pp. 3560–3565.

[111] Hamann, D., "Diffusion of Atomic Oxygen in SiO_2," *Physical Review Letters*, Vol. 81, No. 16, 1998, pp. 3447–3450.

[112] Valentini, P., Tump, P. A., Zhang, C., and Schwartzentruber, T. E., "Molecular Dynamics Simulations of Normal Shock Waves in Dilute Gas Mixtures," 50th AIAA Aerospace Sciences Meeting, Nashville, TN, 2012, AIAA-2012-0225.

[113] Valentini, P., Zhang, C., and Schwartzentruber, T. E., "Molecular dynamics simulation of rotational relaxation in nitrogen: Implications for rotational collision number models," *Physics of Fluids*, Vol. 24, No. 10, 2012, pp. 106101.

[114] Valentini, P. and Schwartzentruber, T. E., "A combined Event-Driven/Time-Driven molecular dynamics algorithm for the simulation of shock waves in rarefied gases," *Journal of Computational Physics*, Vol. 228, No. 23, 2009, pp. 8766 – 8778.

[115] Koura, K., "Monte Carlo direct simulation of rotational relaxation of nitrogen through high total temperature shock waves using classical trajectory calculations," *Physics of Fluids*, Vol. 10, No. 10, 1998, pp. 2689–2691.

[116] Koura, K., "Direct simulation Monte Carlo study of rotational nonequilibrium in shock wave and spherical expansion of nitrogen using classical trajectory calculations," *Physics of Fluids*, Vol. 14, No. 5, 2002, pp. 1689–1695.

[117] Koura, K., "Monte Carlo direct (test-particle) simulation of rotational and vibrational relaxation and dissociation of diatomic molecules using classical trajectory calculations," *AIP Conference Proceedings*, Vol. 585, 2001.

[118] Fujita, K., "Coupled Rotation-Vibration-Dissociation Kinetics of Nitrogen using QCT Models," 36th AIAA Thermophysics Conference, Orlando, FL, 2003, AIAA-2003-3779.

[119] Fujita, K., "Assessment of Molecular Internal Relaxation and Dissociation by DSMC-QTC Analysis," 37th AIAA Fluid Dynamics Conference and Exhibit, Miami, FL, 2007, AIAA-2007-4345.

[120] Fujita, K., "Vibrational Relaxation and Dissociation Kinetics of CO by CO-O Collisions," 40th Thermophysics Conference, Seattle, WA, 2008, AIAA 2008-3919.

[121] Deng, H., Ozawa, T., and Levin, D. A., "Analysis of Chemistry Models for DSMC Simulations of the Atmosphere of Io," *Journal of Thermophysics and Heat Transfer*, Vol. 26, No. 1, 2012, pp. 36–45.

[122] Anderson, J., Lorenz, C., and Travesset, A., "General purpose molecular dynamics simulations fully implemented on graphics processing units," *Journal of Computational Physics*, Vol. 227, No. 10, 2008, pp. 5342–5359, http://codeblue.umich.edu/hoomd-blue.

[123] Frezzotti, A., Ghiroldi, G., and Gibelli, L., "Solving the Boltzmann equation on GPUs," *Computer Physics Communications*, Vol. 182, No. 12, 2011, pp. 2445–2453.

[124] Matsumoto, H. and Koura, K., "Comparison of velocity distribution functions in an argon shock wave between experiments and Monte Carlo calculations for Lennard-Jones potential," *Physics of Fluids A*, Vol. 3, No. 12, 1991, pp. 3038–3045.

[125] Pack, R. T., Walker, R. B., and Kendrick, B. K., "Three-body collision contributions to recombination and collision-induced dissociation. I. Cross sections," *The Journal of Chemical Physics*, Vol. 109, No. 16, 1998, pp. 6701–6713.

[126] Bird, G., "Direct molecular simulation of a dissociating diatomic gas," *Journal of Computational Physics*, Vol. 25, No. 4, 1977, pp. 353–365.

[127] Boyd, I. D., "Analysis of viration-dissociation-recombination processes behind strong shock waves of nitrogen," *Physics of Fluids*, Vol. 178, 1992.

[128] Itina, T. E., Tokarev, V. N., Marine, W., and Autric, M., "Monte Carlo simulation study of the effects of nonequilibrium chemical reactions during pulse laser desorption," *Journal of Chemical Physics*, Vol. 21, 1997.

[129] Gallis, M. A., Bond, R. B., and Torczynski, J. R., "Assesment of Reaction-Rate Predictions of a Collision-Energy Approach from Chemical Reactions in Atmopsheric Flows," 10th AIAA/ASME Joint Thermophysics and Heat Transfer Conference, 2010, AIAA 2010-4499.

[130] Truhlar, D. and Muckerman, J., "Reactive scattering cross sections III: quasiclassical and semiclassical methods," *Atom-Molecule Collision Theory*, 1979, pp. 505–566.

[131] Billing, G. and Wang, L., "Semiclassical calculations of transport coefficients and rotational relaxation of nitrogen at high temperatures," *Journal of Physical Chemistry*, Vol. 96, No. 6, 1992, pp. 2572–2575.

[132] Swope, W. C., Andersen, H. C., Berens, P. H., and Wilson, K. R., "A computer simulation method for the calculation of equilibrium constants for the formation of physical clusters of molecules: Application to small water clusters," *The Journal of Chemical Physics*, Vol. 76, No. 1, 1982, pp. 637–649.

[133] Andersen, H., "RATTLE: A Velocity version of the SHAKE algorithm for molecular dynamics calculations," *Journal of Computational Physics*, Vol. 52, No. 1, 1983, pp. 24–34.

[134] Patkowski, K. and Szalewicz, K., "Argon pair potential at basis set and excitation limits," *Journal of Chemical Physics*, Vol. 133, 2010, pp. 094304.

[135] NVIDIA Corp., "NVIDIA Compute Unified Device Architecture Programming Guide Version 4.2," 2012.

[136] OpenMP Architecture Review Board, "OpenMP Application Program Interface Version 3.0," July 2011.

[137] R. M. Stallman and GCC Developer Community, *Using The Gnu Compiler Collection: A Gnu Manual For Gcc Version 4.3. 3*, CreateSpace, 2009.

[138] Su, C. C., Smith, M., Kuo, F.-A., Wu, J.-S., Hsieh, C.-W., and Tseng, K.-C., "Large-scale simulations on multiple Graphics Processing Units (GPUs) for the direct simulation Monte Carlo method," *Journal of Computational Physics*, Vol. 231, No. 23, 2012, pp. 7932–7958.

[139] Gao, D. and Schwartzentruber, T. E., "Optimizations and OpenMP implementation for the direct simulation Monte Carlo method," *Computers & Fluids*, Vol. 42, No. 1, 2011, pp. 73–81.

[140] Gao, D., Zhang, C., and Schwartzentruber, T. E., "Particle Simulations of Planetary Probe Flows Employing Automated Mesh Refinement," *Journal of Spacecraft and Rockets*, Vol. 48, No. 3, 2011, pp. 397–405.

[141] Dietrich, S. and Boyd, I., "Scalar and parallel optimized implementation of the direct simulation Monte Carlo method," *Journal of Computational Physics*, Vol. 126, No. 2, 1996, pp. 328–342.

[142] LeBeau, G., "A parallel implementation of the direct simulation Monte Carlo method," *Computer Methods in Applied Mechanics and Engineering*, Vol. 174, No. 3, 1999, pp. 319–337.

[143] Ivanov, M. S., Markelov, G. N., and Gimelshien, S. F., "Statistical Simulation of Reactive Rarefied Flows: Numerical Approach and Applications," 7th AIAA/ASME Joint Thermophysics and Heat Transfer Conference, Albuquerque, NM, 1998, AIAA-1998-2669.

[144] Landau, L. D. and Lifshitz, E. M., "Statistical Physics, Vol. 1," *Oxford: Pergamon*, Vol. 24, 1980, pp. 31–57.

[145] Alsmeyer, H., "Density profiles in argon and nitrogen shock waves measured by the absorption of an electron beam," *Journal of Fluid Mechanics*, Vol. 74, No. 3, 1976, pp. 497–513.

[146] Thömel, J., Lukkien, J. J., and Chazot, O., "A Multiscale Approach for Building a Mechanism base Catalysis Model for High Enthalpy CO_2 Flow," 39th AIAA Thermophysics Conference, Miami, FL, 2007, AIAA-2007-4399.

[147] Brunauer, S., Emmett, P. H., and Teller, E., "Adsorption of gases in multimolecular layers," *Journal of the American Chemical Society*, Vol. 60, No. 2, 1938, pp. 309–319.

[148] Landau, L. D., "Zur theorie der energieubertragung. ii," *Physics of the Soviet Union*, Vol. 2, No. 2, 1932, pp. 46–51.

[149] Zener, C., "Non-adiabatic crossing of energy levels," *Proceedings of the Royal Society of London. Series A, Containing Papers of a Mathematical and Physical Character*, Vol. 137, No. 833, 1932, pp. 696–702.

[150] Chaban, G., Jaffe, R., Schwenke, D. W., and Huo, W., "Dissociation cross sections and rate coefficients for nitrogen from accurate theoretical calculations," 46th AIAA Aerospace Sciences Meeting and Exhibit, Reno, NV, 2008, AIAA-2008-1209.

Appendix A

CPU/GPU Parallelization Pseudocode and Three Body Collision Cross Sections in CTC-DSMC

Pseudocode for Parallelization of Collisions in CPU and GPU

Parallelization of the collision code with OpenMP is accomplished relatively easily. After collision partners have been assigned at each DSMC time step, collisions are executed with the following code:

```
#pragma openmp parallel for schedule(dynamic)
for(int i = 0; i < number_collisions; i++) {
    collide_particles(cpu_collisions[i]);
}
```

where the subroutine `collide_particles()` performs a collision between particles with velocities and rotational energies stored in the array `cpu_collisions[]`. To carry out collisions on the heterogeneous GPU/CPU system, some collisions are processed with

above approach on the CPU while others are sent to the GPUs and carried out with the approach shown below. The data structures used are:

```
struct collision {
  double V[2][3] //particle velocities
  double erot[2] //particle rotational energies
}
struct collision_data {
  double X[4][3] //individual atom positions
  double V[4][3] //individual atom velocities
}

collision cpu_collisions[] // Allocated on CPU
collision gpu_collisions[] // Allocated on GPU
collision_data gpu_collision_data[] //Allocated on GPU
```

The pseudocode, which is executed at every DSMC time step, is as below. A diagram of the memory reads used in this algorithm is shown in Fig. A.1.

1. At each DSMC timestep populate `cpu_collisions[]` with N_{coll} collisions.
2. Pre-process collisions on GPU:
   (a) Copy N_{coll} `cpu_collisions[]` (on CPU) to `gpu_collisions[]` (on GPU)
   (b) For each collision in `gpu_collisions[]`:
      i. Generate random impact factor, molecular orientations, and rotational velocity direction.
      ii. Use molecular velocities, rotational energies to set atomic velocities for each molecule in `gpu_collision_data[]`.
3. Execute collisions on GPU:
   (a) Divide up collisions into blocks of threads:
   `int threads_per_block = 64`, (optimized for our specific architecture, see section 4.1)

`int coll_per_thread = rnd_down_pwr2`[1]`(`N_{coll}`/4096)` (optimized for our specific architecture, see section 4.1)

`int n_blocks = rnd_up_pwrof2`[1]`(`N_{coll}`)/(threads_per_block * coll_per_thread)`

(b) Integrate Collisions: Each thread reads collision data from the array index `first_coll`, while subsequent collisions are read from between `block_start` and `block_fin`. A conceptual diagram of the memory reading pattern is shown in Fig. A.1.

i. `int first_coll = thread_id + threads_per_block * block_id.`
`int block_start = (n_blocks + (block_id)*(coll_per_thread-1)) * threads_per_block`
`int block_fin= (n_blocks + (block_id+1)*(coll_per_thread-1)) * threads_per_block`
`int idx = first_coll`
`__shared__`[2] `int next_coll = block_start`

ii. Copy `gpu_collision_data[idx].X[][],V[][]` to local arrays `X_loc[][]`, `V_loc[][]`

iii. Integrate collision until finished

iv. Copy local `X_loc[][]`, `V_loc[][]` back to global memory (`gpu_collision_data[idx]`)

v. `idx = atomicAdd`[3]`(next_coll, 1)`

vi. if(`idx >= block_fin`) break, else goto ii

4. Post process collisions on GPU:

(a) For each item in `gpu_collision_data[]`:
transform atomic velocities (`gpu_collision_data.V[][]`) to molecular velocities and rotational energies (`gpu_collisions.V[][]`, `gpu_collisions.erot[][]`).

(b) Copy N_{coll} `gpu_collisions[]` on GPU collisions to `cpu_collisions[]` on CPU.

[1] round integer down or up to the nearest power of 2

[2] __shared__ indicates a variable is shared by all threads within a block[135]

[3] atomicAdd is a non-blocking operator which increments the shared variable `next_collision` and returns the unincremented value[135]

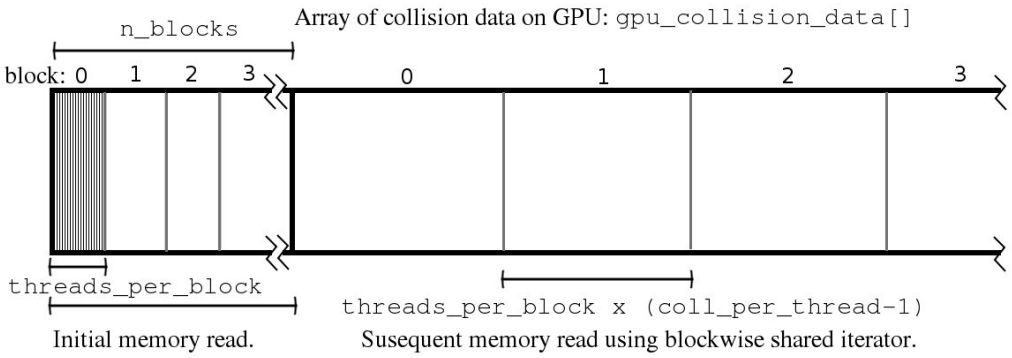

Figure A.1: Diagram of memory reads for collision processing.

Three Body Collision Cross Section

In the CTC-DSMC three body collision algorithm, the probability of a two body collision colliding with another particle is:

$$P_{coll} = \frac{\sigma|\vec{g}_{3B}| \times \frac{\tau_{2B}}{\Delta t_{DSMC}} \times \frac{\tau_{1B}}{\Delta t_{DSMC}}}{(\sigma|g_{3B}|)_{max}} \tag{A.1}$$

Here we outline a method to find the volume V_{3B} swept out by a two body collision in the direction of $\vec{g}_{3B}$:

$$V_{3B} = \sigma|\vec{g}_{3B}| \times \tau_{2B} \tag{A.2}$$

with a Monte Carlo integration. A diagram of this volume for particles with a diameter D_{cutoff} is shown in Fig. A.2(a). The volume V_{3B} is uniquely defined by $\vec{g}_{3B}$, and can only be evaluated once a two body collision and another body are paired to test if they collide. The relative velocity $\vec{g}_{3B}$ is:

$$\vec{g}_{3B} = \vec{v}_{com,2B} - \vec{v}_{1B} \tag{A.3}$$

Where $\vec{v}_{com,2B}$ is the center of mass velocity of the two body collision and $\vec{v}_{1B}$ is the velocity of the other body. To evaluate V_{3B}, the two body collision is integrated as usual with $\vec{g}_{3B}$ added to the velocity of each particle. For constant cross-section molecules with no interatomic potential, the volume swept out is defined by the initial ($\vec{X}_{1,i}$,$\vec{X}_{2,i}$) and final ($\vec{X}_{1,f}$,$\vec{X}_{2,f}$) positions of the atoms in the collision (for particles with non-zero interatomic potential, a list of points representing the collisions could be used instead.)

To perform the volume integration, Monte Carlo integration points ($\vec{X}_{MC}$) are randomly generated within a box with a volume V_{box} defined by the initial and final coordinates of the collision with a bounding tolerance of D_{cutoff}. If points are within the volume swept out by the collision, they are accepted, and V_{3B} is given by:

$$V_{3B} = V_{box} \times \frac{N_{accept}}{N_{total}} \tag{A.4}$$

A point $\vec{X}_{MC}$ is provisionally accepted if it meets the following criteria:

$$(\texttt{distance\_lineseg}(\vec{X}_{n,f}, \vec{X}_{n,i}, \vec{X}_{MC}) < D_{cutoff}) \& (\texttt{distance}(\vec{X}_{n,i}, \vec{X}_{MC}) > D_{cutoff}) \tag{A.5}$$

Where n can refer to either body in the two body collision, and `distance_lineseg` is a subroutine that returns the minimum distance between a line segment defined by the first two points and the third. Points $\vec{X}_{MC}$ that lie within a distance D_{cutoff} of the initial collision locations ($\vec{X}_{1,i}$, $\vec{X}_{2,i}$) must be treated specially to account for actual volume swept out during a collision. For example, if a point $\vec{X}_{MC}$ lies within D_{cutoff} of $\vec{X}_{1,i}$, it should only be accepted if it is a distance greater than D_{cutoff} away from position $\vec{X}_1$(t) at the time t during the trajectory when leading surface of $\vec{X}_2$(t) coincides with the point. With this method, most points within D_{cutoff} of the initial collision locations ($\vec{X}_{1,i}$, $\vec{X}_{2,i}$) are rejected. Finally, if a molecule in the two body collision is moving backwards relative to $\vec{g}_{3B}$, points within the volume swept out by that molecule are rejected. Figure A.2(b) shows the accepted Monte Carlo integration points of a sample two body collision.

For Monte Carlo volume integrations in the three body collision rates presented in Chapter 5, we used 10,000 points. Using more points did not significantly change the three body collision rates. The number of required volume integrations can be reduced in the acceptance/rejectance portion of the three body collision algorithm by testing if the three body collision is provisionally accepted with $V_{3B} = V_{box}$ (V_{box} is cheap to compute), and if the collision is accepted, rechecking the acceptance with V_{3B} evaluated by integration.

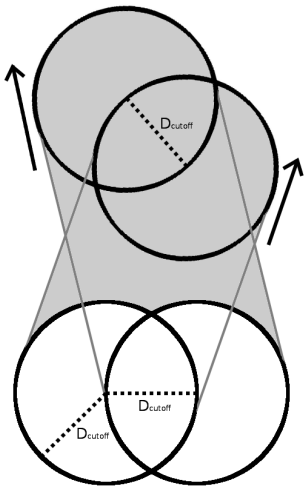

(a) Diagram of the volume swept out by a two body collision. Volume swept out is highlighted in grey.

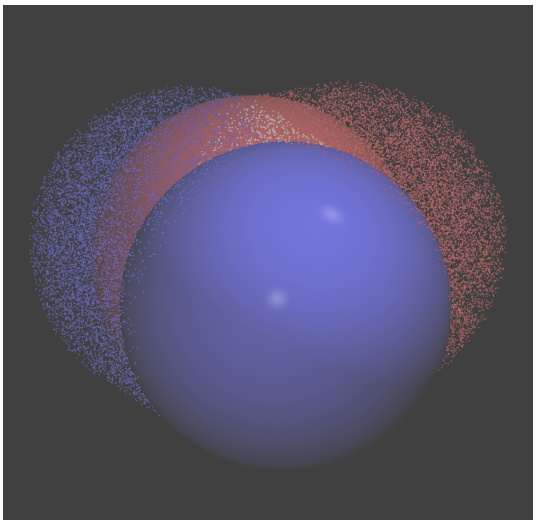

(b) Example of a Monte Carlo volume integration of a two body collision. Atom 1 is red and atom 2 is blue. Small points represent accepted integration points. Blue points are within the volume swept out by atom 1, red points are within the volume swept out by atom 2, and white points are within both.

Figure A.2: The volume swept out by a two body collision.